A ^{127}Xe Calibration Source for the LoLX Detector

Lisa Rudolph, Faculty of Science

McGill University, Montreal

August, 2024

A thesis submitted to McGill University in partial fulfillment of the requirements of the degree of

Master of Physics

Abstract

The Light-only Liquid Xenon (LoLX) detector is a small R&D detector located at McGill University that is designed to study the properties of light transport in liquid xenon (LXe) using silicon photomultipliers (SiPMs). LoLX is currently being used to monitor and characterize the long-term behaviour of Hamamatsu VUV4 and FBK VUV-HD3 SiPMs; both of which are being considered by the neutrinoless double beta decay experiment nEXO. In order to monitor the behaviour of these SiPMs, the use of augmenting the LXe with a radioactive ^{127}Xe source has been proposed. This work will cover the motivation for using ^{127}Xe as a calibration source, as well as the theoretical underpinnings as to how to make such a source from natural xenon gas.

Abrégé

Le détecteur de xénon liquide à lumière seule (LoLX) est un petit détecteur de recherche et de conception situé à l'Université McGill, conçu pour étudier les propriétés du transport de la lumière dans le xénon liquide (LXe) à l'aide de photomultiplicateurs au silicium (SiPMs). LoLX est présentement utilisé pour surveiller et caractériser le comportement à long terme des SiPMs Hamamatsu VUV4 et FBK VUV-HD3, tous deux pris en compte par l'expérience de désintégration double bêta sans neutrino nEXO. Afin de surveiller le comportement de ces SiPMs, on a proposé d'augmenter le LXe avec une source radioactive de ^{127}Xe. Ce travail portera sur les raisons de l'utilisation de ^{127}Xe comme source d'étalonnage, ainsi que sur les fondements théoriques de la fabrication d'une telle source à partir de xénon naturel.

Contribution of Authors

All chapters of this thesis were written by the author. Furthermore, all images, unless otherwise specified, were produced by the author as well. The Python code was written by the author and reviewed by Dr. Brian Lenardo to ensure its quality. Lastly, all of the activity calculations in Chapter 7 were done by the author.

The CAD drawings were produced by the author; however, A. Schonewille created the stand-in for the High Energy Metals coupler as seen in Appendix A.1 Drawing Number XAC009.

Dr. Thomas Brunner provided the inaugural edits for this thesis and Justin Quan provided edits for the French Abstract.

Acknowledgements

I would like to extend my gratitude to my family for being incredibly supportive of my endeavours, no matter where, or what, they entail. Even though after all these years I still don't think they know what a neutrino is, I am always glad to hear them ask about my work with earnestness and sincerity.

I would also like to thank my supervisor Dr. Thomas Brunner, David Gallacher, and Dr. Brian Lenardo for their immense help over the past few years. I would not have been able to complete this thesis without your guidance and advice.

To my past supervisor Dr. Kâmil Uludağ, I would like to thank you for teaching me the importance of taking one's time as life is not a race nor is there a penalty for deciding that your path in life will look different from someone else's. In addition to this, I am glad that you took the time to teach me that failing does not make one a failure. And if you are to become a failure, that's okay, as it need not permeate your entire being; life goes on. At the time I think I was too young to appreciate what you meant, but as I get older I often find myself reflecting on those words.

I would like to extend my immense appreciation for the work done by the chemists Dr. K. Schmiegel and L. Panizzon as they have helped to change not only my life in numerous, positive ways, but the lives of millions of others. I would not be the person I am today without them.

To my wonderful, glorious, vivacious, and effervescent friends: your witticisms, quips, and shenanigans brought so much joy to the past few years. Your support, camaraderie,

guidance, and knowledge have meant so much to me and I am incredibly glad to have met you. You are all truly invaluable.

Lastly, I would like to thank A. Schonewille as well as Taiga. You two are truly the star at the centre of my world, and the warmth and kindness you give illuminate my life in every aspect. You are both so incredibly precious to me, and I am forever glad to be a part of your lives.

Table of Contents

Abstract i

Abrégé ii

Contribution of Authors iii

Acknowledgements iv

List of Figures x

List of Tables xi

1 Introduction **1**

2 Neutrino Physics and the Standard Model **4**

2.1 History and the Nature of the Neutrino 4

2.2 Solar Neutrino Problem 6

2.3 Neutrino Oscillation 6

2.3.1 Solar and Atmospheric Neutrino Oscillations 9

2.4 Massive Neutrinos and Majorana Particles 12

2.4.1 Dirac-Type Neutrinos 13

2.4.2 Majorana-Type Neutrinos 14

2.5 Double Beta Decay 15

3 nEXO's Search for $0\nu\beta\beta$ in ^{136}Xe **20**

3.1 ^{136}Xe and Its Applications in $0\nu\beta\beta$ Decay Searches 20

3.2 Experimental Sensitivity and Background 22

3.3 LXe Time Projection Chambers 23

3.4 nEXO . . . 26
3.5 Detector Calibration Methods for nEXO . . . 29
3.5.1 Event Energy Reconstruction . . . 29
3.5.2 Radioactive Calibration Sources . . . 30

4 Light Detection and Silicon Photomultipliers 33
4.1 P-N Junctions, Photodiodes, and APDs . . . 34
4.2 SiPMs . . . 38
4.3 Photodetector Requirements for nEXO . . . 39

5 LoLX: The Light-only Liquid Xenon Detector 42
5.1 The LoLX Detector . . . 42
5.1.1 LoLX: The Initial Generation . . . 43
5.1.2 LoLX^2: The Second Generation of LoLX . . . 45
5.2 A ^{127}Xe *In Situ* Calibration Source . . . 46

6 Radioactive Decay and Radioisotope Production 48
6.1 Radioactivity and the Bateman Equation . . . 48
6.1.1 The Bateman Equation and Decay Chains . . . 49
6.1.2 Activity . . . 52
6.2 Radioisotope Production . . . 52
6.2.1 Neutron Capture . . . 53
6.2.2 Radioisotope Production Due to Radiative Capture . . . 54

7 Production of a ^{127}Xe Calibration Source 57
7.1 Royal Military College Nuclear Reactor . . . 58
7.2 Canister Design . . . 58
7.3 Natural Xenon . . . 61
7.3.1 Activity of ^{nat}Xe Gas . . . 65
7.4 Canister Activity . . . 71

7.4.1 Activity of Al 6061 72
7.4.2 Activity of Stainless Steel 321 80
7.5 Proposed Safety Measures and Calibration Source Deployment Method . . 87

8 Conclusion **90**

A **91**

A.1 Canister Components 91
A.2 Canister Assembly Instructions 103
A.3 Assembled Canister Design 106

List of Figures

2.1 Production of atmospheric neutrinos from cosmic rays. 10
2.2 Proposed neutrino mass hierarchies. 13
2.3 Mass parabola for A=136. 17
2.4 Feynman diagrams of double beta decay and neutrinoless double beta decay. 18
2.5 Energy spectrum for $2\nu\beta\beta$ and $0\nu\beta\beta$ decay. 19

3.1 Decay scheme for ^{136}Xe. 22
3.2 Charge and light production in LXe. 25
3.3 Diagram of the nEXO detector. 27
3.4 Diagram of the nEXO TPC. 28
3.5 Schematic of the charge collection tile for nEXO. 28
3.6 External calibration sites around the nEXO TPC. 31
3.7 Decay chains for ^{220}Rn and ^{222}Rn. 32

4.1 Diagram of a PMT. 34
4.2 Diagram of a p-n junction. 35
4.3 The different operational regimes of a p-n junction. 36
4.4 Simplified electrical diagram of a SPAD. 37
4.5 nEXO energy resolution at the $Q_{\beta\beta}$ value as a function of photodetection efficiency. 41

5.1 Diagram of first generation of LoLX. 43
5.2 Diagram of the LoLX Cryostat. 44

5.3 Diagram of light production within LoLX and the decay scheme of the ^{90}Sr beta source. 45
5.4 Schematic of the LoLX^2 detector. 46
5.5 Plot of the ^{127}Xe decay scheme. 47

6.1 A diagram of radiative capture. 53
6.2 Plot of neutron capture cross-section as a function of neutron energy. 54

7.1 RMC reactor schematic. 59
7.2 Design of the Al canister. 61
7.3 Composition of ^{nat}Xe. 62
7.4 Psuedocode used to calculate radioisotope activity. 66
7.5 Expected activities for radioisotopes resulting from ^{nat}Xe. 67
7.6 Pseudocode for the Bateman equation for the case where n=2. 68
7.7 Expected activities over time for radioisotopes resulting from ^{nat}Xe. 69
7.8 The elemental composition of Al 6061. 71
7.9 Expected activity of Al 6061. 75
7.10 Expected activities of Al 6061 after irradiation ends. 77
7.11 Pseudocode for the Bateman equation for the case where n=3. 78
7.12 The elemental composition of stainless steel (SS) 321. 80
7.13 Expected activity of SS 321. 84
7.14 Expected activity of SS 321 after irradiation ends. 85
7.15 Layout of the Xe gas handling system. 89

List of Tables

2.1 PMNS matrix values. 13

3.1 Common isotopes that undergo $2\nu\beta\beta$ decay. 21

4.1 Common semiconductors and their properties. 36

7.1 Properties of isotopes present within ^{nat}Xe. 62

7.2 Radioisotope properties resulting from ^{nat}Xe exposure to thermal neutrons. 64

7.3 Xe radioisotope activities. 70

7.4 Isotopes present within Al 6061. 73

7.5 Radioisotopes produced from neutron activation on Al 6061. 74

7.6 Al 6061 radioisotope activities. 79

7.7 Properties of isotopes present within Stainless Steel (SS) 321 that produce radioisotopes. 81

7.8 Radioisotopes produced from the thermal neutron capture of isotopes within SS 321. 82

7.9 SS 321 radioisotope activities. 86

Chapter 1

Introduction

The Standard Model (SM) of Particle Physics is the theory born from the collective effort of thousands of physicists to explain how elementary particles and three of the four fundamental forces interact with one another. One group of these elementary particles, the leptons, contains a subset of electrically-neutral, spin-1/2 particles known as neutrinos. The neutrino, which comes in three flavours defined by the charged lepton involved in the interaction i.e., electron neutrino (ν_e), muon neutrino (ν_μ), and tau neutrino (ν_τ), was originally thought to be a massless particle in the early years of the SM. However, results from the Homestake Experiment in the late 1960s (see Chapter 2 for further details) suggested that neutrinos were able to oscillate flavours, something only possible for massive neutrinos [1]. Thirty years later, in the late 1990s and early 2000s, the Super-Kamiokande collaboration in Japan and the Sudbury Neutrino Observatory (SNO) in Canada provided concrete evidence that neutrinos can oscillate flavour, and were indeed massive particles [2, 3].

The existence of massive neutrinos indicated that the SM was still incomplete, and necessitated that changes had to be made to the SM to account for non-zero neutrino masses. If neutrinos were to acquire their mass in a manner similar to other leptons, right-handed neutrinos would have to exist. However, as right-handed neutrinos have

not been found to exist it has been postulated that neutrinos are Majorana-type particles: neutrally charged, spin-1/2 particles that are their own antiparticles [4].

One method of determining if the neutrino is a Majorana-type particle is by witnessing the hypothesized neutrinoless double beta decay ($0\nu\beta\beta$). During conventional double beta decay, two neutrons decay into two protons with the emission of two electrons and two electron antineutrinos. Much like traditional beta decay, $0\nu\beta\beta$ involves the decay of two neutrons into two protons, but only the two electrons are emitted.

The nEXO collaboration plans on testing the proposed Majorana nature of the neutrino by looking for $0\nu\beta\beta$ decays in a liquid xenon (LXe) time projection chamber (TPC) enriched to 90% in the isotope ^{136}Xe. As ^{136}Xe is capable of undergoing traditional double beta decay, it makes for an excellent candidate for $0\nu\beta\beta$ decay.

In LXe TPCs, energy deposits result in the emission of light as well as ionization charges. The nEXO collaboration is planning to use silicon photomultipliers (SiPMs) to detect the scintillation light. The ability of these SiPMs to detect light is of key importance to nEXO as the detector's energy resolution is highly dependent on the light-detection efficiency of these SiPMs. For these reasons, it is important to understand the properties and characteristics of the SiPMs that have been proposed for the nEXO detector.

The Light-only Liquid Xenon (LoLX) R&D detector, located at McGill University, offers a chance to understand and characterize these SiPMs as well as study them over an extended period of time. However, in order to do so, baseline behaviour must be established. For these reasons, a radioactive ^{127}Xe source is being developed as an *in situ* calibration source for LoLX.

This thesis will cover the history of neutrino physics and the theoretical motivations for the nEXO experiment (Chapter 2) as well as the proposed nEXO detector (Chapter 3). Chapter 4 gives a brief overview on the history of photodetectors, and delves into the theory behind p-n junctions, photodiodes, avalanche photodiodes, and then SiPMs. The Chapter ends with the relationship between the light detection efficiency of the SiPMs and the energy resolution of nEXO. This transitions into Chapter 5 which goes into more

detail about the LoLX R&D detector at McGill University and the research that is being done regarding the characterization and understanding of the proposed SiPMs for nEXO. The reasoning for using radioactive ^{127}Xe as an *in situ* calibration source is given, as well as a proposed methodology for doing so. Chapter 6 covers the basics of radioactive decay, the Bateman equation, radiative capture, and radioisotope production. Lastly, Chapter 7 delves into the process of making a ^{127}Xe calibration source for LoLX.

Chapter 2

Neutrino Physics and the Standard Model

2.1 History and the Nature of the Neutrino

The neutrino is an electrically neutral, spin-1/2 fermion, that interacts via the weak interaction. The neutrino, which had previously been thought to be massless, is the lightest fermion within the Standard Model (SM) and it comes in three flavours: the electron neutrino (ν_e), the muon neutrino (ν_μ), and the tau neutrino (ν_τ). The existence of the neutrino was first postulated by Wolfgang Pauli in 1930 as a means to explain the perceived breaking of momentum, energy, and spin conservation that was seen in beta-decay experiments [5]. At the time, results from beta-decay experiments showed that the emitted electron had a continuous kinetic energy distribution [6]. This was at odds with the theoretical understanding of beta-decay, for if beta-decay solely consisted of the emission of an electron then there would be a well-defined and narrow energy distribution [7, 8]. However, this continuous spectrum indicated that there was energy lost somewhere during the decay, which implied an apparent lack of energy conservation. In order to solve this problem, Pauli postulated a neutral, massless particle that was present during weak interactions. This particle, the neutrino, would share the energy with the electron and

would ensure angular momentum and spin conservation. The neutrino remained a hypothesized particle until July of 1956 when an article published in Science declared its discovery [9]. This article, written by C. Cowan, F. Reines, F. Harrison, H. Kruse and A. McGuire, described what would be known as the Cowan-Reines neutrino experiment, which definitively proved the existence of the neutrino and earned Reines the 1995 Nobel Prize in Physics [10].

The Cowan-Reines neutrino experiment consisted of a water tank with dissolved $CdCl_2$ positioned between liquid scintillators and situated close to a nuclear reactor which functioned as the neutrino source [9]. Their experiment utilized the following reaction where the incoming electron antineutrino ($\overline{\nu}_e$) would react with a proton (p) in the water and produce a neutron (n) and a positron (e^+):

$$\overline{\nu}_e + p \rightarrow n + e^+.$$

The positron would then annihilate with a nearby electron which would result in the emission of two 511 keV gamma rays. The neutron would be captured by a cadmium nucleus in an excited stated and subsequently emit gamma rays [11]. These gamma rays would interact with the liquid scintillator and the resulting photons would be recorded by the photomultiplier tubes. Their experiment yielded positive results and confirmation of the neutrino as well as a measurement of the neutrino cross section [9]. This experiment confirmed the existence of electron neutrinos.

Further experiments by Dr. Leon Lederman, Dr. Melvin Schwartz, and Dr. Jack Steinberger in 1962 [12] and by the DONUT Collaboration in 2001 [13] would prove the existence of two more neutrino flavours: the muon neutrino and the tau neutrino, respectively. Following these discoveries, analyses of Z boson decays at the Large Electron-Positron (LEP) collider and the Stanford Linear Collider (SLC) determined there to only be three flavours of light neutrinos [14], relating to the three flavours of charged leptons: electron (e), muon (μ), and tau (τ).

2.2 Solar Neutrino Problem

During the late 1960s neutrino physics was still in its infancy when it became the cause of much speculation and confusion. The Homestake Experiment (also known as the Brookhaven Solar Neutrino Experiment) had produced results that once again showed a discrepancy between theory and experiment. In order to study the neutrino flux emitted from the Sun, astrophysicists engineered an experiment that would take place deep underground in the Homestake Gold Mine where they would fill a 10^6 gallon tank with tetrachloroethylene (C_2Cl_4) [1, 15]. Tetrachloroethylene, a common dry-cleaning fluid, was chosen as it was a rich source of chlorine, and as such the following reaction could be taken advantage of to detect neutrinos:

$$\nu_e + {}^{37}\text{Cl} \rightarrow {}^{37}\text{Ar} + e^-.$$

In this inverse beta-decay reaction an electron neutrino would react with the ^{37}Cl and produce the radioactive isotope ^{37}Ar ($T_{1/2} \approx 35$ days [16]) as well as an electron. By collecting the radioactive Ar isotopes from the tank and counting them, the neutrino flux from the Sun could be deduced. The results were quite unexpected as they found that the experimentally determined flux was roughly one third of the theoretically predicted value [1]. This discrepancy, that confounded physicists, was referred to as the Solar Neutrino Problem.

2.3 Neutrino Oscillation

A decade prior to the Homestake experiment, the physicist Bruno Pontecorvo proposed a novel idea that neutrinos could change their flavour [17]. Having been inspired by the $K^0 \rightleftarrows \overline{K}^0$ oscillations, Pontecorvo postulated that if neutrinos could change flavour, then the electron neutrinos leaving the sun may no longer be electron neutrinos when they reached Earth, i.e., $\nu_e \rightleftarrows \nu_\mu$ [17]. This would turn out to be an attractive explanation

for the results of the Homestake experiment, for if the electron neutrinos that were produced by the sun were no longer electron neutrinos once they reached Earth, the Homestake experiment would not be sensitive to them - thereby explaining the discrepancy between measured and predicted solar neutrino flux values.

In 1969, Pontecorvo and Vladimir Gribov calculated the likelihood that an electron neutrino would remain in its state after travelling from the Sun to the Earth, and found that if neutrino oscillations were present then the detected neutrino flux would be decreased by a factor of $\sim$2, which was similar to the observations made at the Homestake experiment [18].

However, Pontecorvo's hypothesis was at odds with the physicists' understanding of the SM at that time. In order for the neutrino to change flavour while traveling, at least two of the neutrino mass eigenstates must have a non-zero mass - a notion that was in disagreement with the SM which assumed that neutrinos were massless.

In Pontecorvo's proposed model it was thought that each of the neutrino flavour eigenstates (ν_e, ν_μ, ν_τ) corresponded to a linear combination of the three mass eigenstates ν_1, ν_2, and ν_3. Therefore, a neutrino flavour state could be written as

$$|\nu_\alpha\rangle = \sum_j U^*_{\alpha j} |\nu_j\rangle \tag{2.1}$$

where α denotes the flavour (e, μ, τ), j denotes the mass (j = 1, 2, 3), and $U_{\alpha j}$ are components of the unitary Pontecorvo-Maki-Nakagawa-Sakata (PMNS) matrix U [19, 20]. The

PMNS matrix, analogous to the CKM matrix for quarks, can be expressed as

$$
\begin{aligned}
U &= \begin{bmatrix} U_{e1} & U_{e2} & U_{e3} \\ U_{\mu 1} & U_{\mu 2} & U_{\mu 3} \\ U_{\tau 1} & U_{\tau 2} & U_{\tau 3} \end{bmatrix} \\
&= \begin{bmatrix} c_{12}c_{13} & s_{12}c_{13} & s_{13}e^{-i\delta} \\ -s_{12}c_{23} - c_{12}s_{23}s_{13}e^{i\delta} & c_{12}c_{23} - s_{12}s_{23}s_{13}e^{i\delta} & s_{23}c_{13} \\ s_{12}s_{23} - c_{12}c_{23}s_{13}e^{i\delta} & -c_{12}s_{23} - s_{12}c_{23}s_{13}e^{i\delta} & c_{23}c_{13} \end{bmatrix} \begin{bmatrix} e^{i\alpha_1/2} & 0 & 0 \\ 0 & e^{i\alpha_2/2} & 0 \\ 0 & 0 & 1 \end{bmatrix},
\end{aligned}
\tag{2.2}
$$

where $c_{ij} = \cos\theta_{ij}$ and $s_{ij} = \sin\theta_{ij}$ are mixing angles and $\alpha_{i=1,2}$ and δ are phase factors.

In order to understand how a neutrino of flavour α behaves over time, one can apply the Schrodinger equation to the mass state ν_j, which yields

$$
|\nu_j(t,x)\rangle = e^{-i(E_j t - p_j x)}|\nu_j(0,0)\rangle, \tag{2.3}
$$

where E_j and p_j are the energy and momentum of the neutrino. If the neutrino were to travel a distance L, we can make some changes to the above equation. If we assume that the neutrino will be highly relativistic as it travels, we can make the assumption that $t \approx L$. Furthermore, if the neutrino mass is much less than its momentum, and all the mass eigenstates have the same momentum, the energy term becomes

$$
E_j = \sqrt{p^2 + m_j^2} \approx p + m_j^2/2p. \tag{2.4}
$$

Incorporating this and the assumption that $t \approx L$ into Equation 2.3 yields

$$
|\nu_j(L)\rangle = e^{-i(m_j^2 L/2p)}|\nu_j(0)\rangle. \tag{2.5}
$$

This can be further simplified to $p = E$ if one assumes that the neutrino mass is much smaller than its energy. Substituting Equation 2.5 back into Equation 2.1, we can obtain an expression for the flavour state vector after travelling a distance L:

$$|\nu_\alpha(L)\rangle \approx \sum_j U^*_{\alpha j} e^{-i(m_j^2/2E)L} |\nu_j\rangle \tag{2.6}$$

where m_j is the mass of the neutrino mass eigenstate and E is the neutrino energy.

The likelihood of a neutrino changing its flavour over a distance is derived from the probability that the neutrino has flavour β at distance L given by

$$\begin{aligned} P_{\alpha\to\beta} &= |\langle\nu_\beta|\nu_\alpha(L)\rangle|^2 \\ &= \left|\sum_j U^*_{\alpha j} U_{\beta j} e^{-i\frac{m_j^2 L}{2E}}\right|^2 \\ &= \delta_{\alpha\beta} - 4\sum_{j>k} \Re(U^*_{\alpha j} U_{\beta j} U_{\alpha k} U^*_{\beta k}) \sin^2\left(\frac{\Delta m^2_{jk} L}{4E}\right) \\ &+ 2\sum_{j>k} \Im(U^*_{\alpha j} U_{\beta j} U_{\alpha k} U^*_{\beta k}) \sin\left(\frac{\Delta m^2_{jk} L}{2E}\right), \end{aligned} \tag{2.7}$$

where $\Delta m^2_{jk} \equiv m^2_j - m^2_k$, L is the distance the neutrino travels, and E is its energy. It is clear from Equation 2.7 that the probability of flavour oscillation depends on the difference of the squared masses, implying that at least two of the mass eigenstates are non-zero and different from the other. Therefore, discovery of neutrino oscillations would be evidence for at least two massive neutrinos.

2.3.1 Solar and Atmospheric Neutrino Oscillations

A similar quandary to the solar neutrino problem was present in the measurements of atmospheric neutrinos. Atmospheric neutrinos are neutrinos that are produced due to interactions between the Earth's atmosphere and cosmic rays: high-energy particles, consisting mostly of protons, that are produced by extraterrestrial sources [21]. When they interact with the nuclei present in the Earth's atmosphere they produce pions as

well as kaons [22]. As seen in Figure 2.1, a charged pion can decay as

$$\pi^{\pm} \rightarrow \mu^{\pm} + \overset{(-)}{\nu}_{\mu} \tag{2.8}$$

with the resulting muon decaying into

$$\mu^{\pm} \rightarrow e^{\pm} + \overset{(-)}{\nu}_{\mu} + \overset{(-)}{\nu}_{e}. \tag{2.9}$$

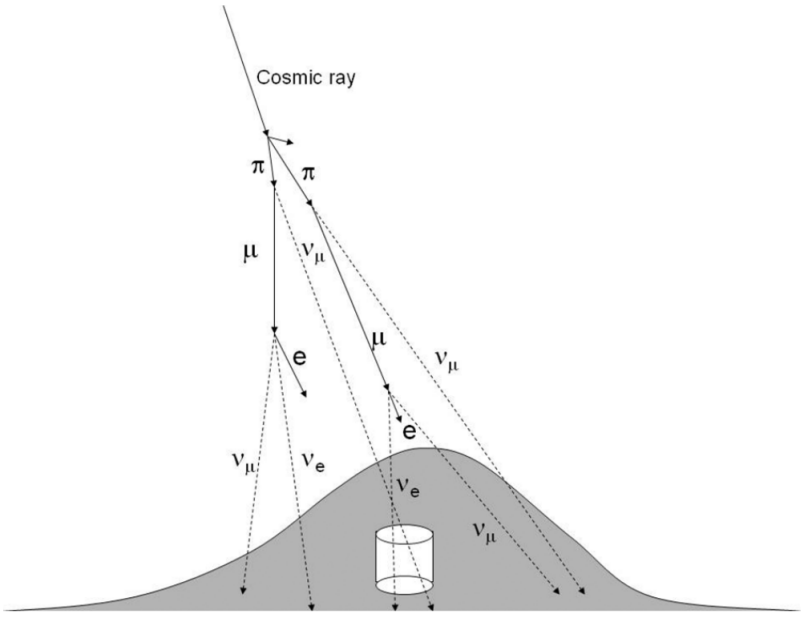

Figure 2.1: Incident cosmic rays interact with the nuclei in the atmosphere and produce mesons such as pions and kaons. Atmospheric neutrinos are the byproducts of these mesons decaying. Figure sourced from [22].

However, this is not the only decay mode for a charged pion. While less likely than the previous decay (with a branching fraction of 0.000123 [23]), a charged pion can also decay into

$$\pi^{\pm} \rightarrow e^{\pm} + \overset{(-)}{\nu}_{e}. \tag{2.10}$$

While these are just two ways that atmospheric neutrinos can be produced, it should be noted that charged kaons will also decay and produce neutrinos.

Due to the nature of these decays, it was expected that the ratio of the flux of $\nu_\mu + \overline{\nu}_\mu$ to the flux of $\nu_e + \overline{\nu}_e$ to be $\sim$2 [24]. However, results at detectors such as the Kamiokande water Cherenkov detector in Japan indicated that there was a discrepancy in the detected number of muon-like events. While the number of detected electron-like events agreed with the theoretical predictions, the number of muon-like events was almost half of what was to be expected [25]. Once again it became apparent that there was a discrepancy between theoretical predictions and measurements, and just like the solar neutrino problem, the possibility of neutrino oscillations was proposed as an underlying cause.

Super-Kamiokande is a water Cherenkov detector located in the Mozumi mine, Japan. In 1998 the collaboration presented their results which were consistent with the existence of $\nu_\mu \rightleftarrows \nu_\tau$ oscillations [2]. Furthermore, they were able to determine values for some of the parameters like $\sin^2 2\theta$ and Δm^2 [2].

Shortly after this discovery in 2001, the Sudbury Neutrino Observatory (SNO) collaboration published evidence for neutrino oscillations from their work on solar neutrinos [3]. SNO, an imaging water Cherenkov detector located in Sudbury Ontario, was able to measure the total solar neutrino flux as well as the solar electron neutrino flux. Comparing the two showed that the electron neutrino flux was roughly one third of the total solar neutrino flux [3].

These neutrino oscillation experiments provided conclusive evidence for neutrino oscillations, and subsequently that neutrinos were in fact massive particles. For their work, both Dr. Art McDonald (who led the SNO group) and Dr. Takaaki Kajita (who led the Super-Kamiokande group) where awarded the 2015 Nobel Prize in Physics [26].

The data from these neutrino oscillation experiments has allowed researchers to deduce the values for some of the parameters in the PMNS matrix. While the data indicates that $\Delta m^2_{21} < |\Delta m^2_{32}|$ [27, 28], it does not reveal the neutrino mass scale, the mass of the neutrino, nor do they indicate the hierarchy of the neutrino mass eigenstates. However, cosmological data can be used to constrain the sum of the masses, $m_{cosmo} = \Sigma m_i$, and it currently places a lower limit of $m_{cosmo} \geq$0.06 eV for the normal hierarchy (NH) and

$m_{cosmo} \geq$0.1 eV for the inverted mass hierarchy (IH) [29]. If the neutrino mass hierarchy (NMH) was determined, it would would enable a greater understanding of neutrinos, neutrino mixing, as well as helping to determine the neutrino mass scale [27]. However, there has yet to be any conclusive evidence whether the ν_3 mass eigenstate is heavier or lighter than ν_2 and ν_1 [27].

Since ν_1 and ν_2 are closely spaced, two different mass hierarchies have been put forth to describe these two scenarios, both of which are shown in Figure 2.2. In the NH, ν_3 is the heaviest of the mass eigenstates. In contrast to this is the IH where ν_3 is the lightest mass eigenstate:

1. Normal hierarchy (NH): $m_3 > m_2 > m_1$,
2. Inverted hierarchy (IH): $m_2 > m_1 > m_3$.

Figure 2.2 further shows the fraction of the neutrino flavour within each mass eigenstate while Δm^2_{atm} and Δm^2_{sol} refer to atmospheric and solar neutrino experiments that were able to determine the values for Δm^2_{32} and Δm^2_{21}, respectively.

While current experiments are unable to determine which hierarchy correctly describes the nature of the neutrino, the data from these and other neutrino oscillation experiments has allowed researchers to determine some of the elements in the PMNS matrix. Table 2.1 shows some of the values for the mass terms as well as the mixing angles.

2.4 Massive Neutrinos and Majorana Particles

While the results from Super-Kamiokande and SNO proved the existence of neutrino oscillations, they also pointed out the flaws in the current SM. In particular, the results from these experiments implied that neutrinos were in fact massive particles. Therefore, changes had to be made to the SM in order to account for this new-found knowledge.

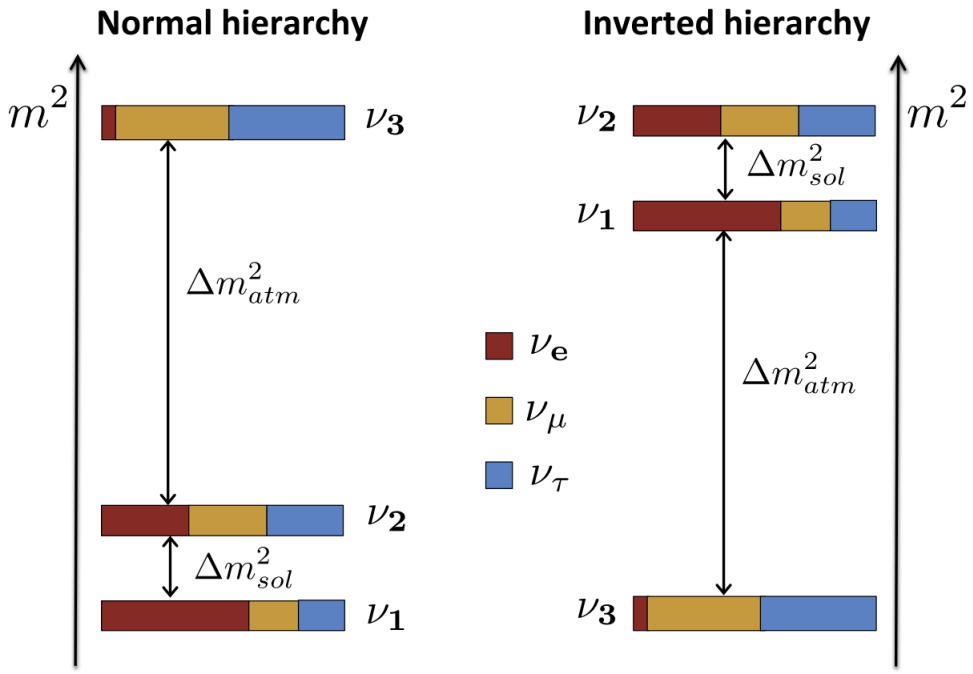

Figure 2.2: A diagram of the two proposed neutrino mass hierarchies. The colours indicate the fraction of neutrino flavours within each mass eigenstate and Δm^2_{atm} and Δm^2_{sol} refer to atmospheric and solar neutrino experiments that measure Δm^2_{32} and Δm^2_{21} (Δm^2_{31} in the IH regime), respectively. Figure sourced from [30].

Table 2.1: Summary of the best fit to the PMNS matrix elements for both the normal (NH) and inverted (IH) hierarchies.

Parameter	NH	IH	Reference
$\Delta m^2_{21}[10^{-5}\text{eV}^2]$	7.53 ± 0.18	7.53 ± 0.18	[23]
$\lvert\Delta m^2_{31}\rvert[10^{-3}\text{eV}^2]$	$2.55^{+0.02}_{-0.03}$	$2.45^{+0.02}_{-0.03}$	[31]
$\Delta m^2_{32}[10^{-3}\text{eV}^2]$	2.437 ± 0.033	-2.519 ± 0.033	[23]
$\sin^2(\theta_{12})$	0.307 ± 0.013	0.307 ± 0.013	[23]
$\sin^2(\theta_{23})$	$0.547\ ^{+0.018}_{-0.024}$	$0.534\ ^{+0.021}_{-0.024}$	[23]
$\sin^2(\theta_{13})$	$(2.20 \pm 0.07) \times 10^{-2}$	$(2.20 \pm 0.07) \times 10^{-2}$	[23]
$\delta[^\circ]$	194^{+24}_{-22}	284^{+26}_{-28}	[31]

2.4.1 Dirac-Type Neutrinos

The existence of non-zero neutrino masses requires that changes need to be made to the SM in order to incorporate them. To do so we can add a Dirac mass term for the

neutrino in the SM Lagrangian where m_D is the Dirac mass, ν_L and $\overline{\nu}_R$ are the left- and right-handed chiral projections respectively, and h.c. is the Hermitian conjugate:

$$\mathcal{L}_D = -m_D \overline{\nu}_R \nu_L + h.c.. \tag{2.11}$$

If neutrinos were simply Dirac-type particles, and their masses were described by the Dirac mass term, then it can be seen from the Hermitian conjugate term in Equation 2.11 that right-handed neutrinos would be required to exist. However, such neutrinos have never been observed experimentally. Furthermore, if there were only Dirac-type neutrinos then it would stand to reason that they would gain their mass in a similar manner to the other leptons through the Yukawa coupling to the Higgs field. But in contrast to the masses of the other leptons, the current experimental upper limits on the mass of the neutrino are roughly 10^6 times smaller than that of the electron [32]. This discrepancy between lepton masses and lack of an observed right-handed neutrino indicates that neutrinos might not solely be Dirac-type fermions.

2.4.2 Majorana-Type Neutrinos

One popular solution is that neutrinos are Majorana-type particles. Majorana particles, first postulated in 1937 by Ettore Majorana, are electrically neutral, spin-1/2 particles that are their own antiparticles, i.e., $\nu_\alpha = \overline{\nu}_\alpha$ [4]. Incorporating this into the SM Lagrangian requires the addition of a Majorana mass term for neutrinos

$$\mathcal{L}_M = -\frac{1}{2} m_R \overline{(\nu_R)^c} \nu_R - \frac{1}{2} m_L \overline{(\nu_L)^c} \nu_L + h.c., \tag{2.12}$$

where m_L and m_R are the left- and right-handed mass terms and ν^c is the charge conjugate of ν. It is important to note that this equation could only be valid for neutrally charged particles, and that this equation would not conserve lepton number.

From here Equation 2.11 and Equation 2.12 can be combined to

$$\begin{aligned}\mathcal{L}_{D+M} &= \mathcal{L}_D + \mathcal{L}_M \\ &= -m_D \overline{\nu}_R \nu_L - \frac{1}{2} m_L \overline{(\nu_L)^c} \nu_L - \frac{1}{2} m_R \overline{(\nu_R)^c} \nu_R + h.c., \quad .\end{aligned} \tag{2.13}$$

If we consider the case of a single flavour of neutrino, we can simplify the above expression into

$$\mathcal{L}_{D+M} = -\frac{1}{2} m_R \overline{(n_L)^c} M n_L + h.c., \tag{2.14}$$

where

$$n_L = \begin{bmatrix} \nu_L \\ (\nu_R)^c \end{bmatrix} \quad \text{and} \quad M = \begin{bmatrix} m_L & m_D \\ m_D & m_R \end{bmatrix} \tag{2.15}$$

and has the mass eigenvalues

$$m_\pm = \frac{1}{2}\left[(m_L + m_R) \pm \sqrt{(m_L - m_R)^2 + 4m_D^2}\right]. \tag{2.16}$$

If $m_L = m_R = 0$, then the equation becomes that for a Dirac neutrino, showing that the Dirac term is just a special case for the more general Equation 2.14.

The existence of a Majorana neutrino would prove that lepton number conservation is not universal, it could indicate that neutrinos obtain their mass differently from other leptons, and it would indicate physics beyond the SM. One such method to test the Majorana nature of the neutrino is with neutrinoless double beta decay.

2.5 Double Beta Decay

Beta decay is a type of radioactive decay that consists of two types: β^+ and β^-. During β^- decay an element with atomic number Z and mass number A has a neutron converted into a proton via the creation and emission of an electron and electron antineutrino. Both types of decay are shown below:

$$\begin{aligned} \beta^- : &\qquad (Z, A) \rightarrow (Z+1, A) + e^- + \overline{\nu}_e, \\ \beta^+ : &\qquad (Z, A) \rightarrow (Z-1, A) + e^+ + \nu_e, \end{aligned} \tag{2.17}$$

where it is evident that β^+ decay is the converse of β^- decay as it is the conversion of a proton into a neutron via the creation and emission of a positron and electron neutrino. However, there are special cases where double beta decay can occur. Double-beta decay ($2\nu\beta\beta$) was first proposed by Dr. Maria Goeppert Mayer in 1935 as a second order weak process where two neutrons decay into two protons with the emission of two electrons and two electron antineutrinos [33]:

$$(Z, A) \rightarrow (Z+2, A) + 2e^- + 2\overline{\nu}_e. \tag{2.18}$$

In order for it to occur, both the atomic number and mass number must be even and the masses must satisfy the following:

1. $m(Z, A) > m(Z+2, A)$, and
2. $m(Z, A) < m(Z+1, A)$,

requiring that the initial mass must be greater than the final mass after double beta decay and that the initial mass must be less than the final mass after single beta decay. This is shown in Figure 2.3, where ^{136}Xe on the Even-Even parabola is forbidden to undergo beta decay to ^{136}Cs; however, it is energetically allowed to decay to ^{136}Ba via two simultaneous beta decays. An example of two simultaneous beta decays is shown in the Feynman diagram in Figure 2.4 a.) where two neutrons are converted into two protons via two W bosons that subsequently decay into two electrons and two antineutrinos. However, this is only for the case for $\nu_\alpha \neq \overline{\nu}_\alpha$.

If neutrinos are Majorana particles then the Feynman diagram in Figure 2.4 b.) could be valid where no neutrinos exist in the final state. This hypothetical process was pro-

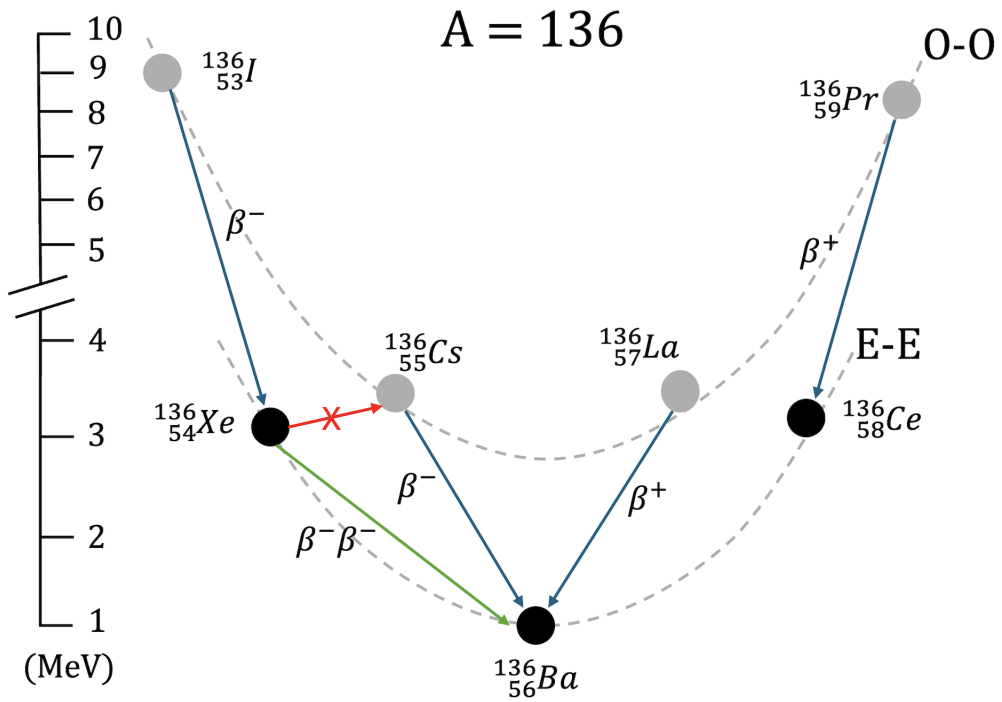

Figure 2.3: Mass parabola for nuclei with A=136 and the decays they are able to undergo. The Even-Even (E-E) parabola shows the nuclei with an even number of protons and neutrons and the Odd-Odd (O-O) parabola shows the nuclei with odd numbers of protons and neutrons. On the left side of the image, ^{136}Xe is forbidden to undergo beta decay to ^{136}Cs. However, it is energetically allowed to decay to nuclei ^{136}Ba via two simultaneous beta decays. Figure reproduced and edited from [34].

posed by W. H. Furry in 1939 and is known as neutrinoless double beta decay ($0\nu\beta\beta$) [36]:

$$(Z, A) \rightarrow (Z + 2, A) + 2e^-. \tag{2.19}$$

The lack of neutrinos in the final state implies the violation of lepton number conservation in weak decays and would constitute physics that is not included in the SM. If light Majorana neutrino exchange is the dominant contributor to $0\nu\beta\beta$, then its decay rate is inversely proportional to the half-life of this decay process [32], with the decay rate given by

$$(T^{0\nu}_{1/2})^{-1} = G_{0\nu}(Q_{\beta\beta}, Z)|M_{0\nu}|^2 \left(\frac{\langle m_{\beta\beta}\rangle}{m_e}\right)^2, \tag{2.20}$$

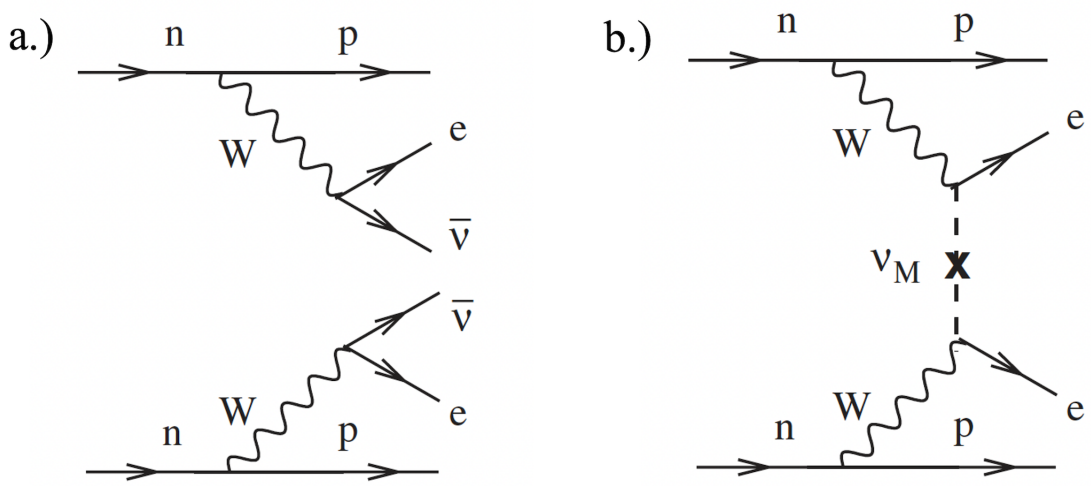

Figure 2.4: Edited and sourced from [35]. a.) Feynman diagram of traditional double beta decay where two neutrons are converted into two protons via the release and decay of two W bosons into two electrons and two antineutrinos. b.) Feynman diagram of neutrinoless double beta decay where no neutrinos are emitted.

where $G_{0\nu}(Q_{\beta\beta}, Z)$ is the phase-space factor for the emission of the two electrons [37], and $M_{0\nu}$ is a nuclear matrix element. $\langle m_{\beta\beta}\rangle$ is the effective Majorana mass which is defined as

$$\langle m_{\beta\beta}\rangle = |\sum_{i=1}^{3} U_{ei}^2 m_i|, \tag{2.21}$$

where U_{ei} are elements of the PMNS matrix.

As both $G_{0\nu}$ and $M_{0\nu}$ are calculated by nuclear theory, if experiments were successful in observing $0\nu\beta\beta$ decay they would be able to use their results to determine $\langle m_{\beta\beta}\rangle$; or if the experiments did not yield positive results then an upper limit on the mass could then be set. It should be mentioned that this is model dependent and only true for a light Majorana mass exchange mechanism.

During classical $2\nu\beta\beta$ decay, the resulting 2-electron energy spectrum, as shown in Figure 2.5, is continuous. In comparison, during $0\nu\beta\beta$ decay all of the energy is shared between the electrons which results in a sharp peak at the end of the $2\nu\beta\beta$ spectrum [39]. The energy where this peak would occur is known as the $Q_{\beta\beta}$ value. The Q-value

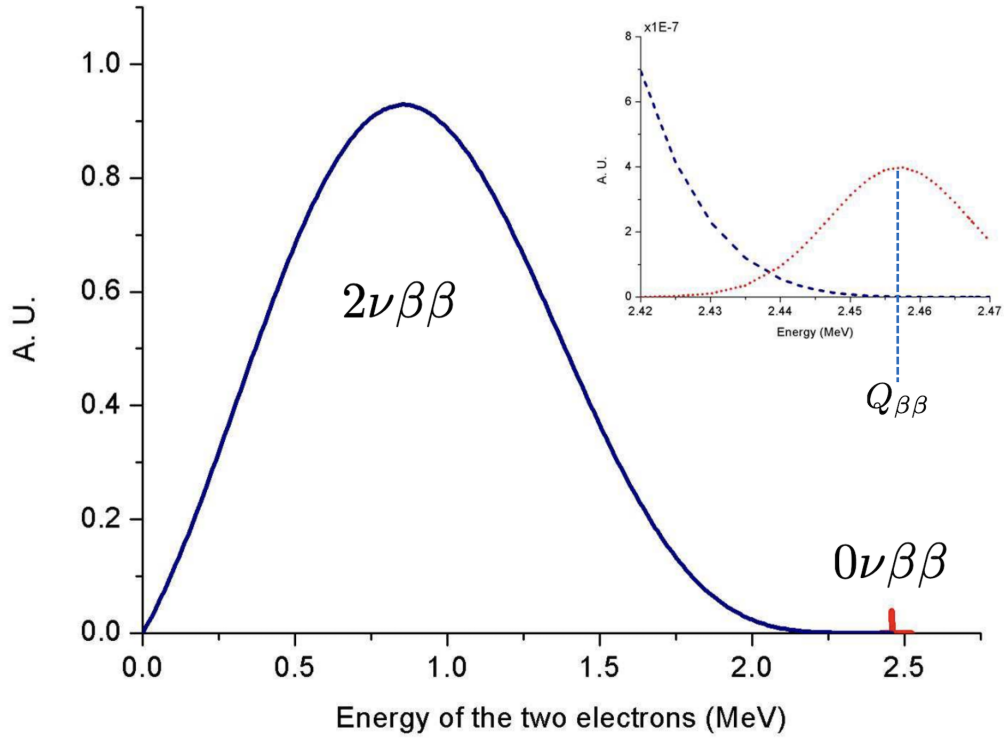

Figure 2.5: The resulting 2-electron energy spectrum for both $2\nu\beta\beta$ (blue) and $0\nu\beta\beta$ (red) decay of ^{136}Xe. A magnified portion of the spectrum at the $Q_{\beta\beta}$ value ($Q_{\beta\beta}$=2.458 MeV) is shown in the upper right corner. Figure sourced and edited from [38].

is defined as the difference in mass between the parent and daughter atom and is the amount of energy released during the decay [40]. For $\beta\beta$ decay, $Q_{\beta\beta}$ is defined as

$$Q_{\beta\beta} = [m(Z, A) - m(Z + 2, A)]c^2, \tag{2.22}$$

where $m(Z, A)$ is the mass of an atom with atomic number Z and atomic mass number A.

Chapter 3

nEXO's Search for $0\nu\beta\beta$ in ^{136}Xe

As shown in the previous chapter, the trademark signal for a $0\nu\beta\beta$ decay is a peak centered at the $Q_{\beta\beta}$ value. The profile and shape of this peak is dependent on the detector resolution; therefore, detecting it, whilst ensuring a high detector resolution and low background signal, is a monumental challenge for physicists.

3.1 ^{136}Xe and Its Applications in $0\nu\beta\beta$ Decay Searches

The detector technology of $0\nu\beta\beta$ decay searches is highly dependent on the isotope of choice. Firstly, the isotope must be capable of undergoing $2\nu\beta\beta$. While there are several that do, see Table 3.1 for the most common ones, the isotope must also have a large $Q_{\beta\beta}$ value, be feasible and cost-effective to procure in large amounts, and be compatible with the desired detection technique [39]. One attractive choice for such an experiment is the isotope xenon-136 (^{136}Xe), which has a Q-value of 2.458 MeV [41].

As a member of the noble gas family, liquid xenon (LXe) has the ability to produce both scintillation photons and ionizing electrons when exposed to radiation. In fact, ionization electrons and scintillation light emission are anti-correlated [46], so when ionization and scintillation signals are detected together it allows for a precise measurement of a particle's energy [47]. In addition to this, due to LXe's large atomic number and density, it

Table 3.1: Properties of the most prevalent isotopes that undergo $2\nu\beta\beta$. Isotope abundance and $Q_{\beta\beta}$ values sourced from [42].

Isotope	Abundance (%)	$Q_{\beta\beta}$ (MeV)	$T_{1/2}$ (yr.)
^{48}Ca	0.187	4.263	$5.3^{+1.2}_{-0.8} \times 10^{19}$ [43]
^{76}Ge	7.8	2.039	$(1.88 \pm 0.08) \times 10^{21}$ [43]
^{82}Se	9.2	2.998	$0.87^{+0.02}_{-0.01} \times 10^{20}$ [43]
^{96}Zr	2.8	3.348	$(2.3 \pm 0.2) \times 10^{19}$ [43]
^{100}Mo	9.6	3.035	$7.06^{+0.15}_{-0.13} \times 10^{18}$ [43]
^{116}Cd	7.6	2.813	$(2.69 \pm 0.09) \times 10^{19}$ [43]
^{130}Te	34.08	2.527	$(7.91 \pm 0.21) \times 10^{20}$ [43]
^{136}Xe	8.9	2.458	$[2.165 \pm 0.016 \pm 0.059] \times 10^{21}$ [44]
^{150}Nd	5.6	3.371	$[9.34 \pm 0.22^{+0.62}_{-0.60}] \times 10^{18}$ [45]

possesses the largest stopping power for penetrating radiation amongst all of the stable liquid noble gases [47]. While radon does have more stopping power than LXe, it is radioactive. Furthermore, the attenuation length of a 2.4 MeV γ-ray in LXe is $\simeq$ 8.7 cm [32], which means that γ-rays produced external to the detector will be less likely to penetrate far into the LXe without scattering, ensuring that the central volume of the detector will remain largely unaffected. This quality can be used to greater extent with larger detectors, as gamma rays will be less likely to reach the central volume. Lastly, the LXe does not have long-lived isotopic radioactive contamination, and it can be repeatedly purified, thereby further increasing the overall purity of the LXe over time [32].

One of the xenon isotopes, ^{136}Xe, comprises 8.9% of natural xenon and it is capable of undergoing $2\nu\beta\beta$ decay, as shown in Figure 3.1. For this reason, and for those previously mentioned, it has become an attractive choice for experiments searching for $0\nu\beta\beta$ decay. The ^{136}Xe isotope was previously used by the EXO-200 experiment to search for $0\nu\beta\beta$ decay using a LXe time projection chamber (TPC) enriched to $\sim 80\%$ with ^{136}Xe [49]. It was the first experiment to observe the $2\nu\beta\beta$ decay of ^{136}Xe [50] as well as to establish its half-life as 2.165 $\pm$ 0.016 $\times 10^{21}$ years [44]. EXO-200 was also able to achieve a half-life sensitivity (expanded upon further in the next section) of $T^{0\nu}_{1/2} > 3.5 \cdot 10^{25}$yr at 90% CL [51].

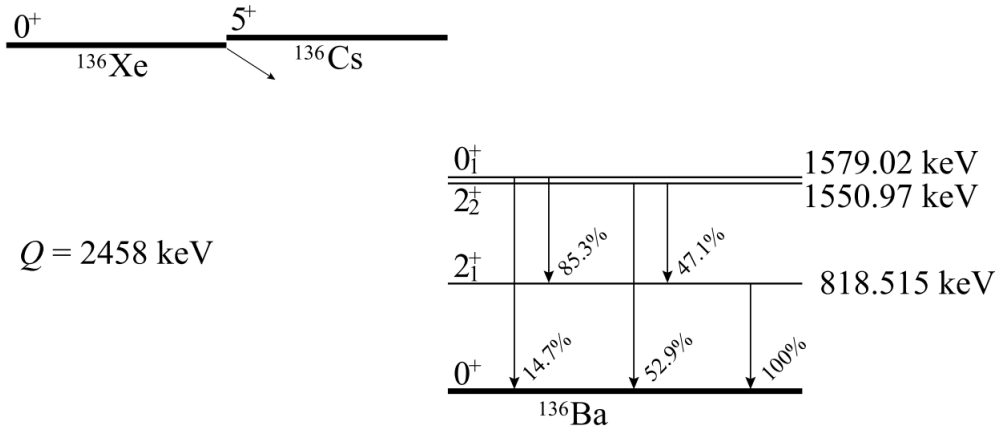

Figure 3.1: The decay scheme for the decay of ^{136}Xe to ^{136}Ba. Scheme sourced from [48].

The work of EXO-200 showed that ^{136}Xe is an attractive candidate for $0\nu\beta\beta$ for multiple reasons. Not only did it undergo double beta decay, as natural Xe is composed of $\sim$ 9% of ^{136}Xe and there are large reserves of natural xenon within the atmosphere, it was relatively easy to procure and enrich to a large percentage. Furthermore, its Q-value of $Q_{\beta\beta}$ = 2458.07 $\pm$ 0.31 keV [41] is much larger compared to the Q-value for other radioactive decays making it easier to determine if a $0\nu\beta\beta$ decay occurred.

3.2 Experimental Sensitivity and Background

In experiments searching for $0\nu\beta\beta$ decay, a common metric to quantify a detector is the sensitivity, which is defined as the half-life of the largest signal that can be hidden by an experiment's background at a given confidence level [52]. As shown in [53], the half-life sensitivity can be expressed as its relationship to the number of possible candidate events one would expect to observe. As the $0\nu\beta\beta$ decay signal is a peak, searches for such a signature occur in a well-defined region around the Q-value, referred to as the region of interest (ROI). If we let N be the number of candidate events within that ROI, it then follows that

$$T_{1/2}^{0\nu} = ln(2)\frac{N_A \varepsilon M t}{W N}, \tag{3.1}$$

where N_A is Avogadro's number, M is the mass of the source, W is the molar mass of the source, ε is the detection efficiency within the ROI, and t is exposure time [53]. Equation 3.1 can then be combined with Equation 2.20 to obtain a value for $m_{\beta\beta}$:

$$m_{\beta\beta} = \sqrt{\frac{NA}{\varepsilon M t}}, \tag{3.2}$$

where

$$A = \frac{W}{ln(2)N_A G_{0\nu}(Q_{\beta\beta}, Z)|M_{0\nu}|^2}.$$

However, this formula is only applicable for a background-free scenario, which is seldom likely to occur. In order to account for the presence of a background, one can use the large background approximation to find that the sensitivity of an experiment can be described as the square root of the mean predicted background level (b): $S(b) \simeq \alpha\sqrt{b}$ [54], where α is a constant. Following the approach described in [54], substituting N in Equation 3.2 for $\alpha\sqrt{b}$ yields

$$m_{\beta\beta} = \sqrt{\frac{\alpha b^{1/2} A}{\varepsilon M t}}. \tag{3.3}$$

Hence, the presence of a background greatly affects the sensitivity of an experiment. Therefore, limiting and controlling sources of background are of paramount importance for experiments attempting to study $0\nu\beta\beta$ decay.

3.3 LXe Time Projection Chambers

In the 1970s, Dr. David Nygren proposed a new type of particle detector that would be able to provide 3-D particle tracking and particle identification during electron-positron collision [55]. This cylindrical detector would be known as a time projection chamber (TPC) and it would consist of a large gaseous drift space with a constant applied electric field [56]. The working principle of the TPC is that a charged particle moving through the gas with sufficient energy will produce ionization electrons and these electrons will drift

towards the endcaps where they will be detected. In the original TPC design, ionization electrons were detected using multiwire proportional chambers which allowed for determining the x-y position of the event [56]. The z position would be determined using the electron drift time [55].

While TPCs originally used a gaseous medium, in 1977 Dr. Carlo Rubbia proposed the use of liquid noble gases as a medium, particularly the use of liquid-argon [57]. Liquid-argon, along with LXe, are the only two of the liquid rare gases to produce both scintillation light and ionization electrons when exposed to radiation [47]. The scintillation light signals can be used along with the charge detection signals to perform a 3-D event reconstruction [47].

In LXe TPCs, ionizing radiation produced from an event causes excitation and ionization of the Xe atoms, which results in ionization electrons and scintillation light. This process is illustrated in Figure 3.2, where one can see that the production of scintillation light is due to two different processes involving ionizing radiation producing excited atoms Xe^* and Xe^+ ions [47]. An excited Xe atom can combine with another Xe atom to form what is known as an excited dimer (Xe_2^*) [47]:

$$\begin{aligned} Xe^* + Xe &\rightarrow Xe_2^*, \\ Xe_2^* &\rightarrow 2Xe + h\nu \quad . \end{aligned} \tag{3.4}$$

When this dimer decays, it produces scintillation light at a wavelength of λ=175 nm. However, scintillation can also be produced as a result of ionization, as shown by [47]:

$$\begin{aligned} Xe^+ + Xe &\rightarrow Xe_2^+, \\ Xe_2^+ + e^- &\rightarrow Xe^{**} + Xe \\ Xe^{**} &\rightarrow Xe^* + \text{heat}, \\ Xe^* + Xe &\rightarrow Xe_2^*, \\ Xe_2^* &\rightarrow 2Xe + h\nu \quad . \end{aligned} \tag{3.5}$$

The scintillation light is then detected by photodetectors inside of the TPC.

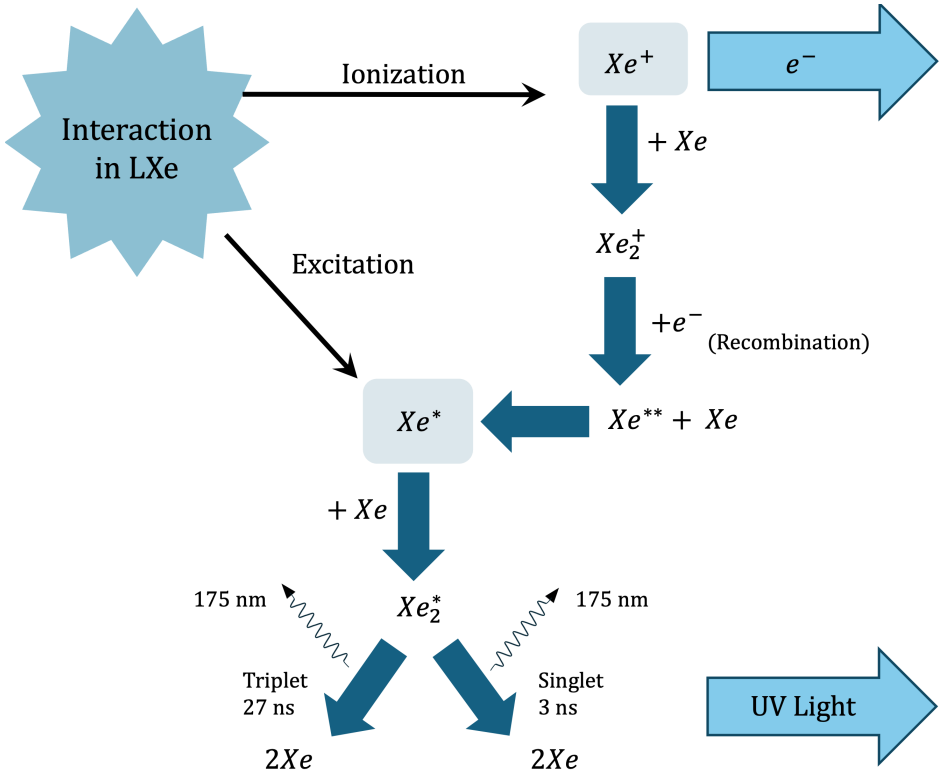

Figure 3.2: Charge and light production in LXe as a result of interactions within the LXe. Image reproduced from [58].

Determining the location of an event within the TPC can be done by combining information from the photodetectors and from the segmented anode. When using a grid-like design, the location of the ionization electrons at the anode allows for reconstructing the x-y position of the event [59]. The difference in arrival time between the photodetector signal and the signal from the anode can be used to determine the depth at which the event occurred (z position), assuming a homogeneous electron drift.

LXe TPCs have previously been used in the EXO-200 experiment and will be used in the proposed nEXO experiment.

3.4 nEXO

The next Enriched Xenon Observatory (nEXO), the successor to EXO-200, is an experiment proposed to test the Majorana nature of neutrinos by deploying 5000 kg of LXe in a single-phase TPC enriched to 90% in the isotope ^{136}Xe [32]. During a decay, nEXO will measure both the scintillation light signals as well as those from drifting ionization and combine this information in order to produce a 3-D map of the energy deposition and location in the TPC. Building upon the work done by its predecessor, nEXO is being designed to achieve a projected sensitivity beyond 10^{28} years with a designed for energy resolution of $\sigma/Q_{\beta\beta}$ = 1 % [60, 61].

However, nEXO has to contend with various sources of backgrounds affecting its sensitivity. Some of the sources of these backgrounds are: long-lived radionuclides, cosmogenically created radionuclides, neutrino-induced backgrounds, radionuclides resulting from (α,n) reactions, and the decay of ^{222}Rn [61]. The backgrounds that pose the greatest threat to nEXO are those which release enough energy to interfere with the ^{136}Xe $0\nu\beta\beta$ signal, in particular those with long half-lives. However, some backgrounds in the form of γ-rays can be identified due to the multiple Compton scattering that they will undergo and they can be excluded from the analysis [32]. The monolithic nature of the LXe TPC, along with the LXe attenuation length, help to diminish the background effects of external γ-rays deep in the detector volume. A proposed location for nEXO is at SNOLAB in Sudbury, Canada, as the depth of the mine will help to shield the detector from external and cosmological radiation. The design for nEXO is shown in Figure 3.3, with the TPC filled with the enriched LXe. It is surrounded by 33,000 kg of a cryogenic fluid (HFE-7000) which will help to minimize temperature fluctuations as well as shield from external γ-rays [32]. The TPC and HFE-7000 are contained within the inner vessel (IV), which in turn is surrounded by the outer vessel (OV) with a vacuum separating them. This vacuum acts as a thermal insulation from the water that surrounds the OV, which is part of the outer detector (OD).

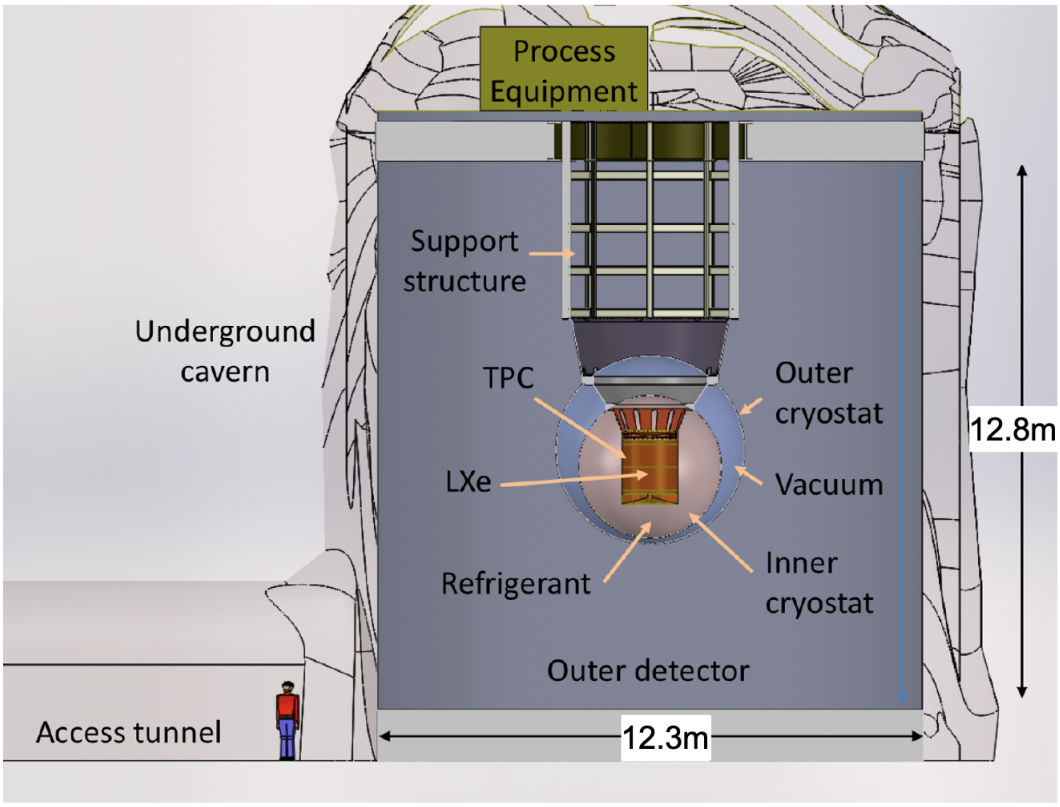

Figure 3.3: A diagram of the nEXO detector. The image shows the geometry and general scale of the overall detector with a focus on the components external to the TPC. Figure sourced and edited from [32].

The OD is a cylindrical water tank that will serve to shield the TPC from external γ-rays and moderate externally produced neutrons. The tank is lined with photomultiplier tubes (PMTs) to detect cosmic radiation. Cosmic radiation, typically in the form of muons, can pass through the detector and cause events in the TPC. This is the result of muon-induced spallation neutrons that are captured on the Xe, as well as detector materials, and thereby create radioactive backgrounds. In order to identify these events, the PMTs inside the OD detect the Cherenkov light produced from the muons passing through the water, which allows researchers to correlate between PMT and TPC activity; thus enabling them to veto possible muon events [32].

As shown in Figure 3.4, the TPC is a vertical copper cylinder of equal height and diameter filled with LXe. A cathode is located at the bottom of the cylinder and current

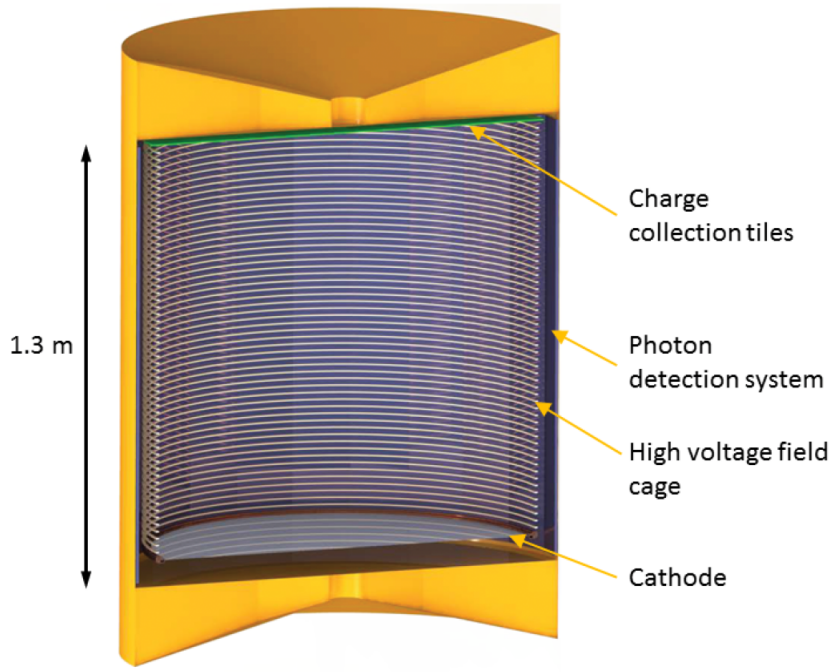

Figure 3.4: A diagram of the nEXO TPC. Image sourced from [32].

research is being undertaken to optimize its design as well as how to mitigate the accumulation of radon decay products on its surface [32]. At the top of the detector is the

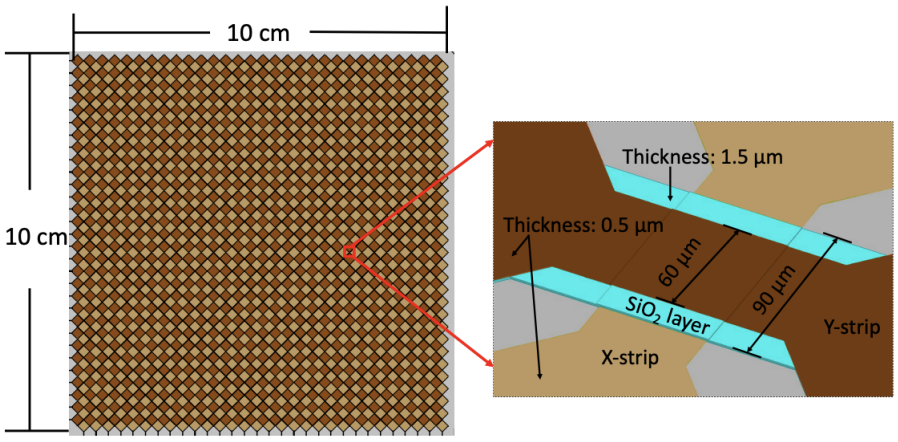

Figure 3.5: A schematic of the charge collection tile for nEXO which highlights its tiled appearance. The light-coloured X strips are connected vertically and the dark-coloured Y strips are connected horizontally. A detailed view shows a thin layer of SiO_2 separating the strips at the pad junction. Image sourced from [62].

segmented anode, shown in Figure 3.5, which features orthogonally-connected "X" and "Y" metal strips [59]. Field shaping rings (FSRs) ensure that the 400 V/cm electric drift field is uniform along the vertical axis. Behind the FSRs, lining the barrel of the cylinder, are the Silicon PhotoMultipliers (SiPMs) which detect the λ=175 nm LXe scintillation light. As the scintillation light wavelength is in the ultraviolet regime, Vacuum Ultraviolet (VUV) SiPMS need to be used for light collection. Presently, nEXO is considering the use of either Fondazione Bruno Kessler (FBK) VUV-HD3 or Hamamatsu Photonics VUV4 SiPMs. A more in-depth explanation of SiPMs and their function will be explained in the following chapter.

3.5 Detector Calibration Methods for nEXO

3.5.1 Event Energy Reconstruction

The energy from an event in the TPC, E, can be written as a combination of the ionization and scintillation signals due to the strong anti-correlation of the two [63]:

$$\langle E \rangle = W \cdot (S + Q), \tag{3.6}$$

where S is the number of scintillation photons released after recombination, Q is the number of ionization electrons released after recombination, and W is a proportionality constant [64]. In this equation W represents the average energy required to form an electron-ion pair.

The scintillation signal, S, can be further defined as

$$S = \frac{S_0}{\varepsilon_0} \tag{3.7}$$

where S_0 is the measured number of photons and ε_0 is the light detection efficiency. We can define ε_0 as:

$$\varepsilon_0 = \varepsilon_{QE} \times \varepsilon_{LM}(x, y, z), \tag{3.8}$$

where ε_{QE} is the quantum efficiency of the SiPMs (see Section 4.2 for more details), which is the probability that a photon incident to a SiPM gets absorbed and triggers an avalanche [32]. Lastly, $\varepsilon_{LM}(x, y, z)$ is a function that describes the photon transport efficiency within the detector [64]. Similar to the initial number of photons, the initial number of ionization electrons, also known as the ionization signal, can be written as

$$Q = \frac{Q_0}{e^{-t/\tau_e}}, \tag{3.9}$$

where Q_0 is the measured number of electrons, τ_e is the electron lifetime in LXe, i.e., the length of time it takes before a free electron adheres to an impurity in the LXe, and t is the drift time [64]. For a uniform drift field, t can be further defined as $t = v_d/z$ where z is the position in the TPC and v_d is the drift velocity.

In order to optimize the energy reconstruction, the accurate measurements of $\varepsilon_{LM}(x, y, z)$ and τ_e are of extreme importance (see [64] for further information regarding the measurement of these values). For these reasons, nEXO is currently looking at external (to the TPC) and internal (to the TPC) calibration methods to determine and monitor these variables.

3.5.2 Radioactive Calibration Sources

The proposed method for external TPC calibration is by using six ^{228}Th sources located outside the TPC at the locations marked in orange in Figure 3.6. Decays from the ^{228}Th to ^{208}Tl decay chain will act as a γ source that will help to monitor the charge-light anti-correlation and measure the electron lifetime within the TPC [32]. It is currently proposed that the TPC will be exposed to these sources for two hours, every other day [32].

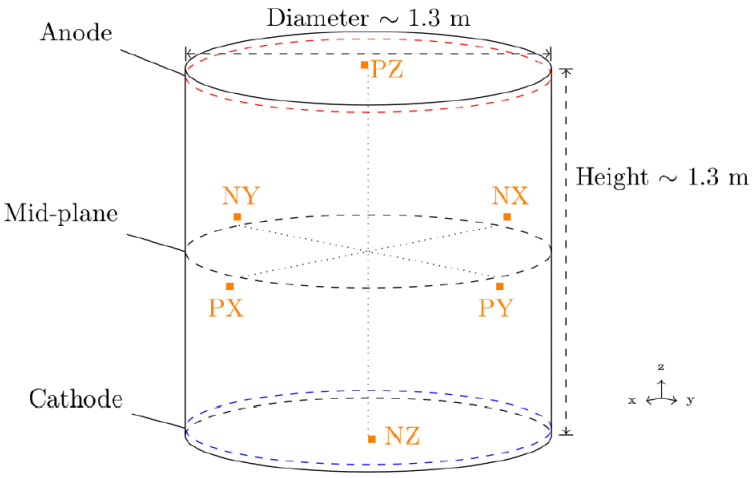

Figure 3.6: External calibration sites around the nEXO TPC depicted by the orange squares. NX, NY, PX, and PY will be located outside of the TPC, and NZ and PZ will be located behind the anode and cathode respectively. Image sourced from [32].

In addition to this, nEXO plans on mapping the light detection efficiency of SiPMs as a function of location within the TPC [32]. A proposed method for doing this is by using a calibration source that emits light at a known energy and moving it to different positions within the TPC and measuring the light response. However, due to the attenuation length in LXe, using a calibration source external to the TPC will decrease the chance of events being evenly distributed in the LXe. Therefore, an idea that was proposed to use either ^{220}Rn or ^{222}Rn as an injectable calibration source that would ensure a homogeneous distribution of event [32]. However, there are challenges with both of these options. Using the decay of ^{220}Rn as a source would require a calibration time of several days [66], and using the decay of ^{222}Rn results in long-lived decay products. As seen in Figure 3.7, one of the radioisotopes in the decay chain is ^{210}Pb, that while not offering any use in terms of calibration, can build up in the detector and act as a source of background [67].

In response to this there has been discussion of using ^{127}Xe as an *in situ* calibration source within the TPC [64]. This topic will be elaborated upon further in Chapters 5 and 7; however, Chapter 4 will focus on the theory regarding SiPMs and why understanding and characterizing them is important for nEXO.

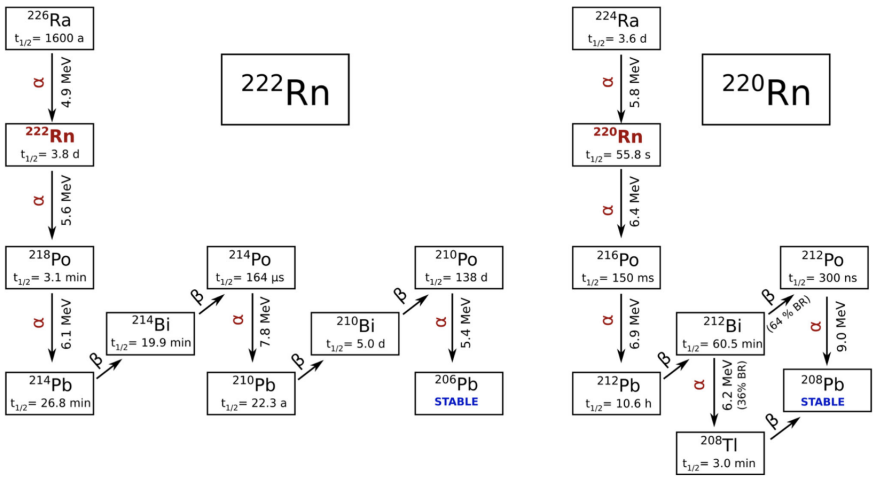

Figure 3.7: Decay chains for the proposed calibration sources ^{220}Rn and ^{222}Rn. Image sourced from [65].

Chapter 4

Light Detection and Silicon Photomultipliers

Photon detection has been important for physics experiments, particularly in the fields of high energy and astroparticle physics, for many decades. The earliest and simplest methods for photon detection relied on the human eye, but had the drawback that it required someone to physically watch the experiment [68]. One of the first inventions to circumvent this issue was the photoelectric tube, invented in the 1910s by Elster and Geitel, which produced a measurable electric current due to the detection of a photon [69].

The current was only proportional to the intensity of the light, which made it difficult for measurements of low-intensity light. In 1930, the Soviet physicist L.A. Kubetsky invented a device that would be able to greatly amplify weak photocurrents to achieve a gain on the order of 10^3-10^4 [70]. These devices, which at the time were known as "Kubetsky's tubes", would be the foundation for the modern photomultiplier tube (PMT).

In a PMT, shown in Figure 4.1, an incoming photon creates an electron at the photocathode due to the photoelectric effect. This photoelectron is then focused and accelerated into a dynode which produces secondary electrons. These secondary electrons are then focused and accelerated to the next dynode and this process is repeated until the resulting pulse is collected at the anode [72,73].

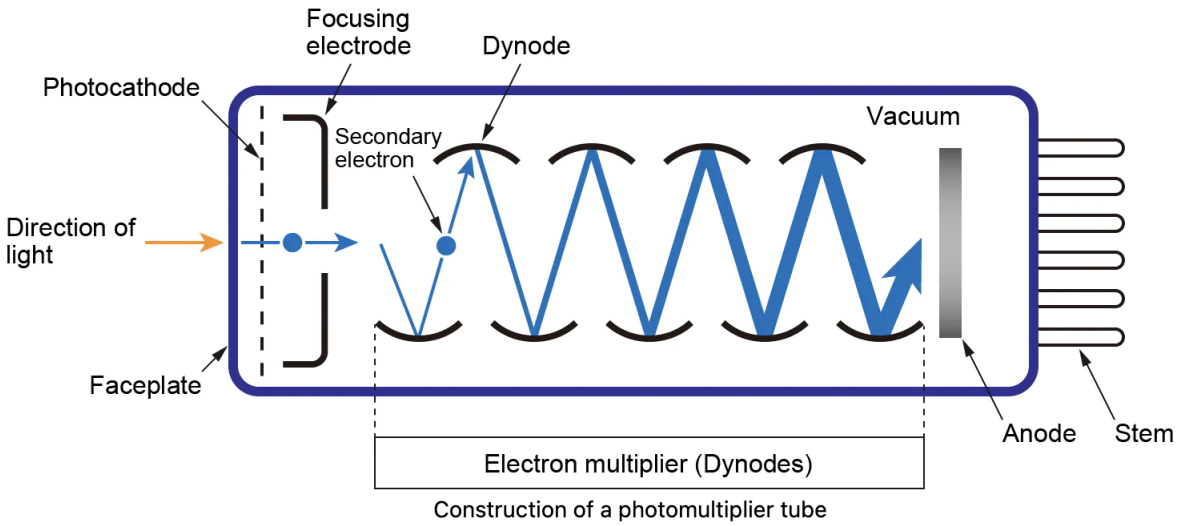

Figure 4.1: A diagram of a photomultiplier tube (PMT) that highlights the effect of electron multiplication. Sourced from [71].

PMTs have been common in physics experiments since their inception; however, they do have their limitations. One of these is that they are affected by magnetic fields, as well as their size, and the fact that they are made with radioactively-impure materials [73]. For these reasons, experiments have looked into other methods for photodetection instead. One such option that has become popular is the silicon-based solid-state photodetector known as a silicon photomultiplier (SiPM). SiPM's are able to detect single photons, which makes them an attractive choice for experiments that depend on photon counting. In addition to this, their small size, insensitivity to magnetic fields, small operating voltage, and fast timing resolution make them advantageous photodetectors [32, 74, 75]. The primary unit of a SiPM is the single-photon avalanche diode (SPAD) and its working principle is based on a p-n junction that is reverse biased above the breakdown threshold [75].

4.1 P-N Junctions, Photodiodes, and APDs

A p-n junction is a boundary between p-doped (positively charged) and n-doped (negatively charged) semiconductor materials [76]. These p-doped and n-doped mate-

rials each have their own charge carriers: holes and electrons respectively. The large concentration of positive charge carriers in the p-doped material causes the holes to migrate towards the n-doped side and recombine with the electrons. Likewise, the negative charge carriers in the n-doped material migrate towards the holes and combine with them. However, this recombination causes negatively charged ions to be present on the p-side towards the junction as well as for positively charged ions on the n-side.

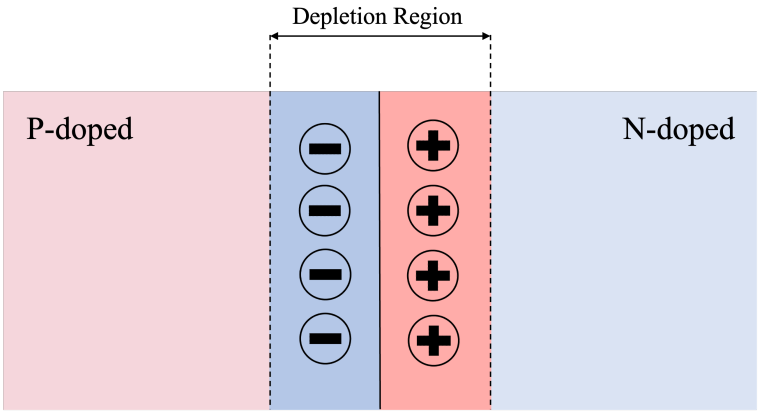

Figure 4.2: A schematic of a p-n junction that highlights the depletion region and shows the concentration of charge carriers.

This results in a region near the junction that contains few charge carriers and is therefore called the depletion region [77]. Figure 4.2 shows a schematic of a p-n junction and highlights the depletion region. As can be seen, the depletion region is positively charged on the n-side and negatively charged on the p-side, thereby creating an internal electric field. Table 4.1 lists some of the more common semiconductors and their physical properties.

A photodiode is a p-n junction with a reverse bias voltage applied to it, meaning that a negative bias is connected to the p-side and a positive bias to the n-side. This causes the charge carriers to move away from the junction, resulting in a widened depletion region. When a photon with energy greater than the band gap energy of the material is absorbed by the photodiode, the absorbed photon creates electron-hole (e-h) pairs in the depletion region via the photoelectric effect and the e-h pairs then move towards

Table 4.1: Common semiconductors and their physical properties. Table sourced from [77].

Semiconductor	Density (g cm^{-3})	Band gap (eV)	Ionization energy (eV/e-h pair)	Dielectric constant (ϵ_s/ϵ_0)
Si	2.33	1.12	3.61	11.9
SiC(4H)	3.21	3.23	7.8	9.66
Ge	5.33	0.68	2.98	16
GaAs	5.32	1.42	4.2	13.1
CdTe	6.06	1.52	4.43	10.36
HgI_2	6.4	2.13	4.3	8.8

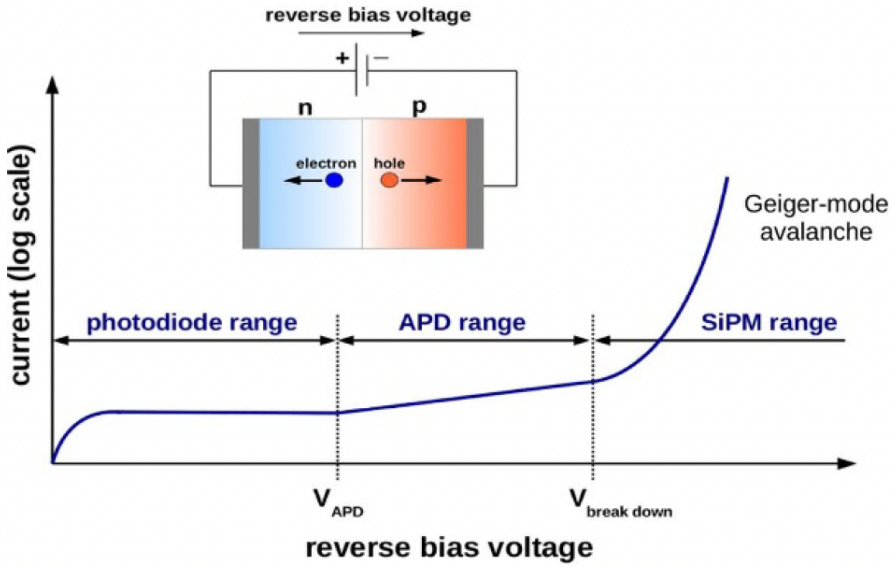

Figure 4.3: The different operational regimes (photodiode, avalanche photodiode, and single-photon avalanche diode/SiPM) of a p-n junction as a function of the applied reverse bias voltage. Image sourced from [75].

their respective regions [75]. As the number of charge carriers does not increase as they traverse, the resulting current output is proportional to the incident light intensity [75]. This operational regime is known as the photodiode regime, as can be seen in Figure 4.3 which shows the different operational regimes for a p-n junction as a function of the applied reverse bias voltage. One drawback of photodiodes is that they cannot be used for single photon detection as there is no internal amplification of charge carriers [78].

If the reverse bias is increased, the electric field becomes large enough that the electron from the e-h pair is able to accelerate and create more e-h pairs through impact ionization [79]. This is known as the avalanche photodiode (APD) regime. In this regime, the gain, or the number of charge carriers collected per avalanche, is proportional to the applied reverse bias [75, 80].

If even greater reverse bias voltage is applied, the results are similar to the APD regime. However, in this scenario, both electrons and holes are accelerated and subsequently create more e-h pairs through impact ionization. This avalanche effect results in an output in the form of a current pulse. This regime is known as the single-photon avalanche diode (SPAD)/SiPM regime, as only a single initial charge carrier is needed to create a self-sustaining avalanche. The voltage that this occurs at is known as the breakdown voltage (V_{BD}), and the difference between the bias voltage and the breakdown voltage is known as the overvoltage, $V_{OV} = V_{bias} - V_{BD}$. When a reverse bias voltage is applied greater than the V_{BD} the SPAD is operating in what is known as Geiger mode [75].

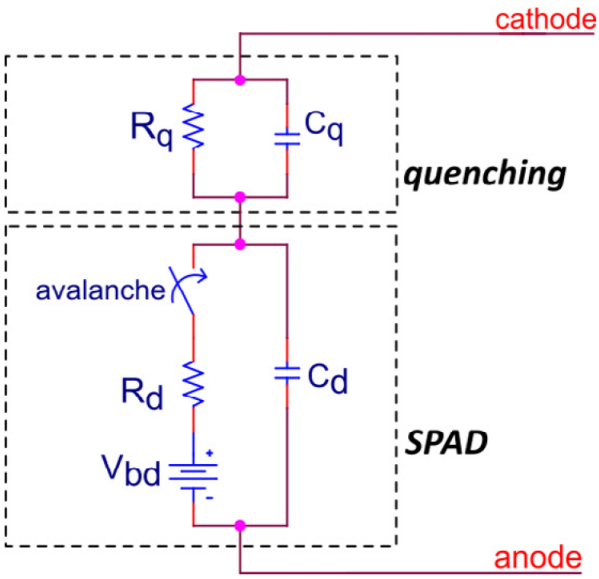

Figure 4.4: A simplified schematic of a SPAD electrical circuit along with the quenching circuit. An avalanche is simulated by closing the switch on the circuit. Figure sourced from [81].

4.2 SiPMs

A simplified electrical diagram of a SPAD is shown in Figure 4.4. In this diagram, the SPAD comprises a series combination of a voltage source, a resistor (R_d), and a switch, all of which are in parallel to a capacitor (C_d). In this diagram, the voltage source is equal to the breakdown voltage, C_d is the capacitance of the inner depletion region, and R_d is the internal resistance of the diode space-charge region [81]. A quenching resistor R_q and a parasitic capacitor C_q are combined in parallel and added to the SPAD in series where they act to return a SPAD to Geiger mode after the SPAD has absorbed a photon and produced an avalanche. It is the parallel combination of many of these SPADs, along with their quenching circuit, that constitutes a silicon photomultiplier (SiPM).

The average gain for an analog SiPM can be described as [81]:

$$\text{Gain} = \frac{V_{OV}(C_q + C_d)}{q} \tag{4.1}$$

where q is the elementary charge. The gain is usually on the order of 10^5-10^7, which results in a signal that is well above expected noise [81].

An important metric to quantify the performance of a SiPM is the photodetection efficiency (PDE). The PDE is the ability for a SiPM to detect photons of a certain wavelength and it is dependent on the overvoltage V_{OV} and the wavelength of the incident photon, λ:

$$\text{PDE}(V_{OV}, \lambda) = \text{QE}(\lambda) \times P_T(V_{OV}, \lambda) \times \text{FF}_{eff}. \tag{4.2}$$

The PDE consists of three factors: the quantum efficiency (QE), the P_T (the avalanche triggering probability), and the FF_{eff} (the effective geometric fill factor) [75]. The QE is the combination of the probability that an incoming photon will cross through the antireflective coat (ARC) on the SiPM surface, caused by the SiPM material having a high refractive index [75], and the probability that it will create an e-h pair that will make it to the high-field region [82]. As the QE is a wavelength-dependent parameter, it is impor-

tant to tailor what semiconductor material is used depending on the wavelength of light that is being measured. The P_T is the probability that the e-h pairs will trigger a Geiger breakdown [83] and the FF_{eff} describes the ratio of the active area, or the area that is able to detect the photon, to the total area of the SiPM [75, 82].

4.3 Photodetector Requirements for nEXO

As mentioned in Section 3.5, the QE is an important parameter for determining the light detection efficiency (ε_0) in nEXO, and by extension the reconstructing of event energy. By combining Equations 3.6, 3.7, and 3.8, we can see how the event energy depends on the QE:

$$\begin{aligned} \langle E \rangle &= W \cdot \left(\frac{S_0}{\varepsilon_{QE} \times \varepsilon_{LM}} + Q \right) \\ &= W \cdot \left(\frac{S_0}{\varepsilon_0} + Q \right). \end{aligned} \tag{4.3}$$

As such, it follows that the energy resolution of nEXO is dependent on the QE as it can be mathematically expressed as

$$\text{Energy Resolution} = \sigma_E / E, \tag{4.4}$$

where σ_E is the standard deviation of $\langle E \rangle$ (see Equation 3.6) [84]. We can write the variance of $\langle E \rangle$ as:

$$\begin{aligned} \sigma^2_{\langle E \rangle} &= W^2(\sigma_Q^2 + \sigma_S^2) \\ &= W^2(\sigma_Q^2 + \frac{S}{\varepsilon_0}[(1 - \varepsilon_0) + \eta_N]), \end{aligned} \tag{4.5}$$

where σ_Q^2 is the variance of the charge noise and η_N is an excess noise factor [32]. Using Equation 4.5 and Equation 4.3, we can express the energy resolution as

$$\frac{\sigma_E}{E} = \frac{\sqrt{\sigma_Q^2 + \frac{S}{\varepsilon_0}[(1-\varepsilon_0) + \eta_N]}}{S_0 + \varepsilon_0 Q} \cdot \varepsilon_0, \tag{4.6}$$

which shows its dependence on the light detection efficiency. As previously mentioned in Section 3.4, nEXO plans to operate at an electric drift field of 400 V/cm. Therefore in order to achieve nEXO's desired energy resolution of 1% at that electric drift field, one finds that the light detection efficiency must be greater than 3% ($\varepsilon_0 > 3\%$) [32], as shown in Figure 4.5. The drift field is based on experience gained with the EXO-200 detector. While a higher electric field would result in an improved energy resolution it also increases the risk of voltage breakdown or sparking in the TPC with potentially catastrophic consequences for the detector's electronics.

We can further express ε_0 as a function of the SiPM photodetection efficiency (ε_{PDE}), the reflectivity (R) at the SiPM surface, and ε_{LM} from Equation 3.8. This yields:

$$\varepsilon_0 = \frac{\varepsilon_{LM} \cdot \varepsilon_{PDE}}{(1-R)}, \tag{4.7}$$

with the SiPM photodetection efficiency defined as

$$\varepsilon_{PDE} = (1-R)\varepsilon_{QE}, \tag{4.8}$$

where ε_{QE} (from Equation 3.8) is the quantum efficiency of the SiPMs. Knowing nEXO's desired energy resolution, we can determine that the required PDE for the SiPMS, at a wavelength of λ=175 nm, is $\varepsilon_{PDE} > 15\%$ [32].

Considering Equation 4.7, it is evident that both ε_{PDE} and R affect ε_0; therefore, as the energy resolution is linearly dependent on ε_0, it is important to study and characterize the reflectivity, photodetection efficiency, and quantum efficiency of nEXO's proposed SiPMs.

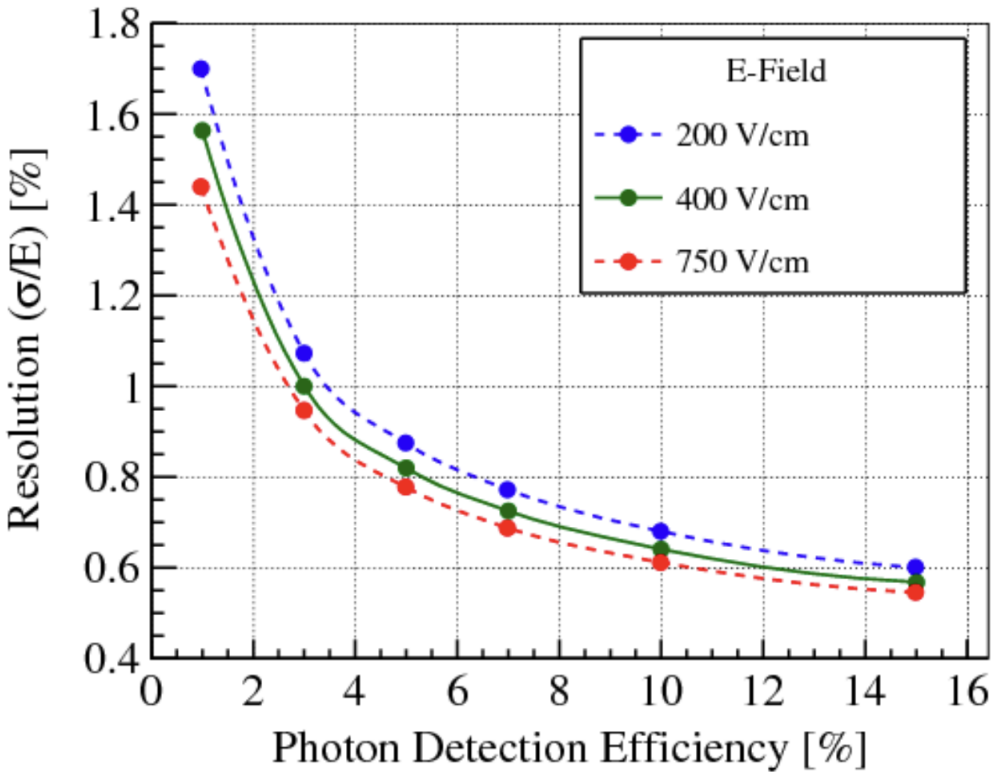

Figure 4.5: nEXO energy resolution at the $Q_{\beta\beta}$ signal as a function of photodetection efficiency. For $\sigma/E = 1\%$, at a drift field of 400 V/cm, the required light detection efficiency is $> 3\%$. Figure sourced from [32].

Chapter 5

LoLX: The Light-only Liquid Xenon Detector

As mentioned in Chapter 3.4, nEXO aims to achieve an energy resolution of $\sigma/Q_{\beta\beta}$ = 1%. However, a key part of determining the energy resolution is the collection efficiency of scintillation light [32]. Therefore, the nEXO collaboration has studied the choices of SiPMs used within nEXO, their behaviour over a long period of time, and the optical transport processes.

5.1 The LoLX Detector

LoLX (Light-only Liquid Xenon) is a LXe R&D detector located at McGill University in Montréal, Canada. It is currently being used for SiPM photosensor research and design for the nEXO experiment.

The primary research goals of the LoLX detector are to understand and to characterize the performance of VUV SiPMS in LXe over a long period of time, and to study light emission, transport, and detection in LXe. Furthermore, the detector aims to study the Cherenkov and scintillation light yields within LXe. Information garnered from LoLX

will help to inform the choice of SiPMs for nEXO as well as to better understand their behaviour in a LXe medium.

5.1.1 LoLX: The Initial Generation

The first generation of LoLX consisted of a 3D-printed octagonal cage that featured 24 Hamamatsu VUV4 SiPM modules (for a total of 96 SiPM dices). The octagonal geometry was chosen to maximize the volume usage in the cylindrical cryostat tube. The detector uses ∼6 kg of LXe, and unlike nEXO, does not have an electric field. As such, electric charge is not recorded and the detector solely detects light, hence its moniker. A photo of the detector during assembly is shown in Figure 5.1.

The detector is contained in a LXe cryostat that is cooled with liquid nitrogen. Figure 5.2 shows a depiction of the LoLX cryostat and the detector's location within.

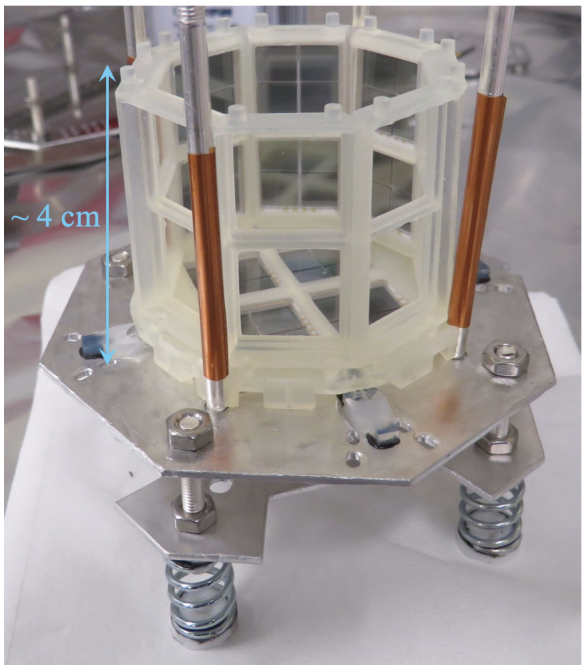

Figure 5.1: The first generation of the LoLX detector during assembly which highlights the 3D-printed cage that houses the SiPMs as well as the relative size of the detector. Image provided by the Brunner Neutrino Lab (BνL) at McGill University.

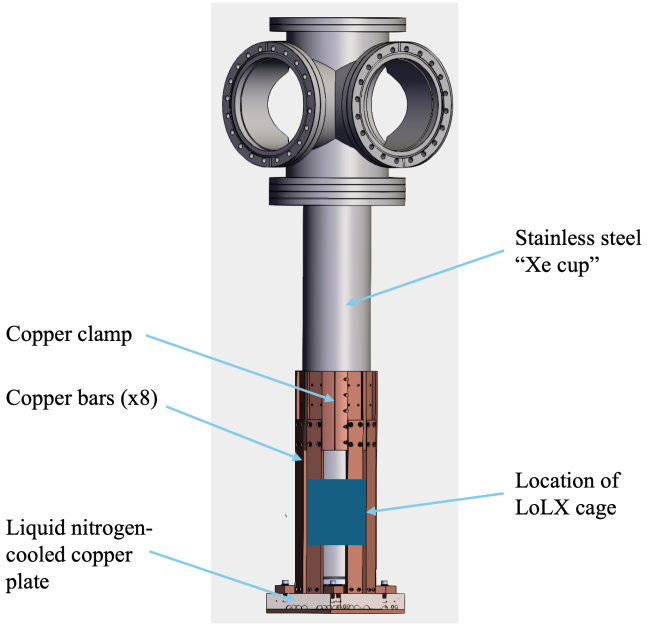

Figure 5.2: Diagram of the cryostat in the initial configuration of LoLX. Figure reproduced from [85].

To provide events with the LoLX detector, a ^{90}Sr beta source was adhered to the tip of a needle and was inserted into the main volume of the detector. Figure 5.3 a.) shows the location of the radioactive source within LoLX, and Figure 5.3 b.) shows the decay scheme for ^{90}Sr.

In order to separate the Cherenkov and scintillation light produced by the radioactive source, different wavelength-selective filters were placed in front of the VUV4 SiPMs. In order to detect Cherenkov light, 22 of the SiPM modules were equipped with long-pass filters that are sensitive to light with a wavelength greater than 225 nm. One of the SiPM modules featured a band-pass filter which was meant to collect only scintillation light, as it was only sensitive to light with a wavelength between 150-180 nm, and finally there was one SiPM module that did not have a filter on it and was sensitive to light of all wavelengths.

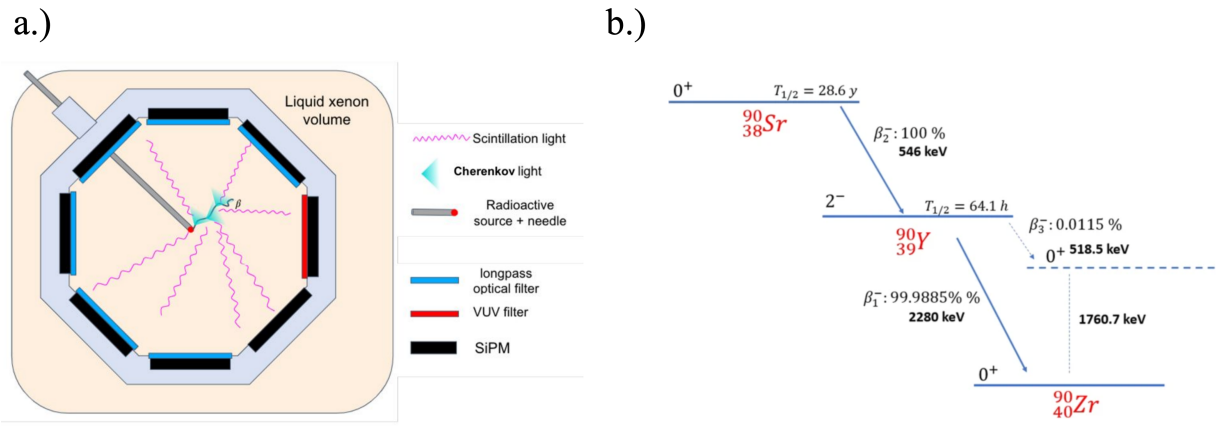

Figure 5.3: a.) A diagram showing both scintillation and Cherenkov light produced by events stemming from the internal ^{90}Sr radioactive source. Also shown are the different filters on the SiPM modules. Original image produced by Austin de St Croix. b.) The decay scheme for ^{90}Sr, which acts as the internal beta source in LoLX. Image sourced from [86].

5.1.2 LoLX^2: The Second Generation of LoLX

In early 2023, the second generation of LoLX, LoLX^2, began. This upgrade removed the 3D-printed cage, and featured the incorporation of a VUV-sensitive PMT, the addition of Fundazione Bruno Kessler (FBK) SiPMs to the previously present Hamamatsu VUV4 SiPMs, and the use of a cryocooler instead of a liquid nitrogen operated cooling system.

The primary design change that was made was to use a cubic-shaped cage based on circuit boards instead of the previous 3D-printed octagonal cage design. While the previous iteration of LoLX was designed to maximize the observed LXe volume, the second generation was modified in order to simplify the geometry. As can be seen in Figure 5.4 b.), 5 panels of the cube feature SiPMs, with each panel further divided into 4 tiles and labeled as either "FBK" or "H" for Hamamatsu. Each of these tiles represent 4 SiPM dices, resulting in LoLX^2 having a total of 40 FBK and 40 Hamamatsu SiPMs. Lastly, a Hamamatsu VUV-sensitive R8520-406 PMT is located at the top of the cage. Figure 5.4 a.) shows a diagram of the new panel design, including the SiPM module locations, as well as the location of the PMT and overall cubic structure of LoLX^2.

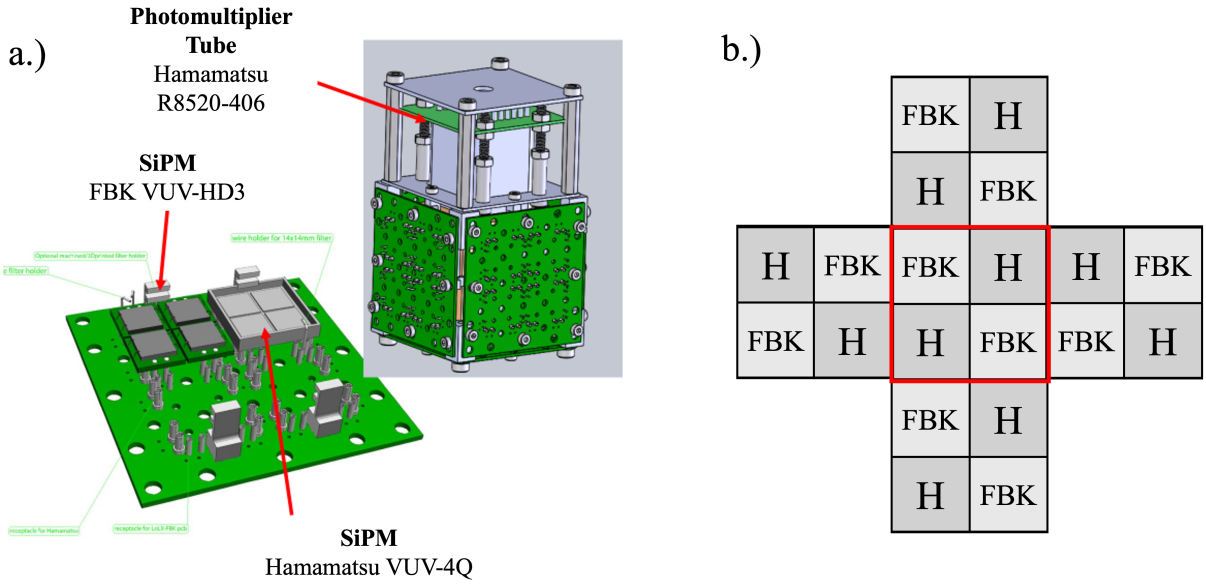

Figure 5.4: A schematic of the LoLX^2 detector. a.) A diagram showing one of the panels of the detector, along with its SiPMs, and the overall cubic structure of the LoLX^2 detector. b.) The SiPM layout within the LoLX^2 detector. The brand of SiPM is denoted as either "H" for Hamamatsu or "FBK" for Fundazione Bruno Kessler and the red square highlights the bottom of the detector. Figure reproduced from [87].

5.2 A ^{127}Xe *In Situ* Calibration Source

A proposed method to monitor the long-term stability and performance of SiPMs within LoLX^2, and by extension nEXO, is to augment the LXe with the radioactive isotope ^{127}Xe [64]. ^{127}Xe is an attractive choice as its Q-value of 662.3 keV is small enough to not interfere with the detection of a $0\nu\beta\beta$ decay, yet its half-life of 36.4 days is long enough that it will allow for *in situ* calibration and characterization whilst the LoLX detector is operating [64, 89]. As seen in Figure 5.5, ^{127}Xe decays to ^{127}I through electron capture, and deposits a total energy of either 236 keV or 408 keV in LXe [64].

The process of making ^{127}Xe relies on the radiative neutron capture (which is described in detail in Section 6.2) on ^{126}Xe. Previous work [64] has already been done by Dr. Brian Lenardo of the nEXO Stanford group regarding the fabrication of a ^{127}Xe calibration source from ^{126}Xe, and they have shown that fabricating such a source is a feasible

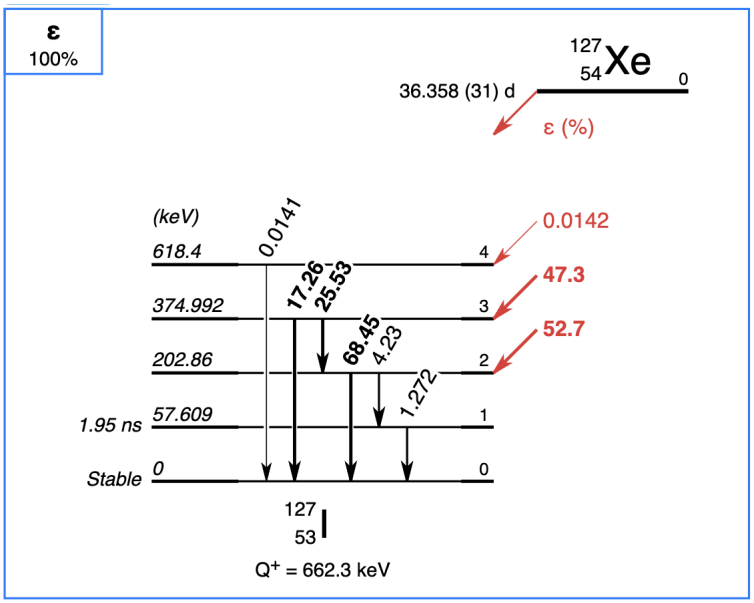

Figure 5.5: The decay scheme of ^{127}Xe. ^{127}Xe decays to ^{127}I through electron capture with a half-life of 36.4 days and a Q-value of 662.3 keV. Image produced using the Laraweb website [88].

option. However, their application of such a source was for the calibration of position-dependent detection efficiencies and not the long term monitoring and characterization of SiPMs that LoLX will be researching [64]. Furthermore, the canister design to hold such a source, as well as the location for the irradiation, and expected radioisotopes will be different than those from the Stanford group.

The methodology for procuring a ^{127}Xe calibration source, as well as the proposed canister design, and the expected activities of the radioisotopes will be covered in Chapter 7. Preceding that, Chapter 6 will cover the theory of radioactive decay and radiative capture.

Chapter 6

Radioactive Decay and Radioisotope Production

Radioactive calibration sources are vital for large experiments such as nEXO, as they enable researchers to understand a detector's response as well as to monitor the detector's behaviour over time. As such, it is important to understand the characteristics of such radioactive sources as well as how to produce them. This chapter will cover the basics of radioactive decay, decay chains and the Bateman equation, as well as radiative capture and the production rate of radioisotopes. Information regarding the implementation of such techniques to manufacture a radioactive calibration source will be covered in Chapter 7.

6.1 Radioactivity and the Bateman Equation

During radioactive decay, the original unstable radionuclide (known as the parent) releases energy via radiation and decays to the daughter nuclide. The time it takes for a source to decay to half of its original amount is known as the radioactive half-life, $t_{1/2}$. For radioactive decay, the half-life is used to define the decay constant, λ, which can be

expressed as

$$\lambda = \frac{ln2}{t_{1/2}}. \tag{6.1}$$

The inverse of the decay constant is known as the mean lifetime, τ:

$$\tau = \frac{1}{\lambda}, \tag{6.2}$$

which is the time required for a radionuclide to decay to $1/e$ of its initial amount.

6.1.1 The Bateman Equation and Decay Chains

As the rate at which the number of parent radionuclides decay to the daughter is governed by Poisson statistics, the change in the number of parent atoms can be described by a differential equation. For the scenario in which you have a non-branching decay, such as:

$$N_1 \xrightarrow{\lambda_1} N_2 \xrightarrow{\lambda_2} N_3 \ldots \xrightarrow{\lambda_{i-1}} N_i,$$

where N_i is the number of atoms of isotope i with decay constant λ_i, the equation that describes the change in the number of atoms with respect to time is [90]:

$$\frac{dN_i}{dt} = \lambda_{i-1} N_{i-1} - \lambda_i N_i. \tag{6.3}$$

The general formula for finding the number of atoms of isotope n at time t is given by the Bateman equation [91] (see [90] for a modern derivation):

$$N_n(t) = N_1(0) \times \left(\prod_{i=1}^{n-1} \lambda_i \right) \times \sum_{i=1}^{n} \frac{e^{-\lambda_i t}}{\prod\limits_{j=1, j\neq i}^{n} (\lambda_j - \lambda_i)}. \tag{6.4}$$

In the case of the decay of a parent isotope to a daughter where $N_1 \xrightarrow{\lambda_1} N_2$, Equation 6.4 reduces to its simplest form, i.e. n=1:

$$\frac{dN_1}{dt} = -\lambda_1 N_1. \tag{6.5}$$

In order to find the number of atoms as a function of time, we can solve Equation 6.5 using the initial condition that $N_1(t = 0) = N_{1,0}$, where $N_{1,0}$ is the initial number of atoms present in the source. This yields

$$N_1(t) = N_{1,0} e^{-\lambda_1 t}, \tag{6.6}$$

which describes how the number of parent atoms changes over time.

In the previous example, if the resulting daughter isotope is not stable and experiences a subsequent decay as well $\left(N_1 \xrightarrow{\lambda_1} N_2 \xrightarrow{\lambda_2} N_3 \right)$ we can find the number of N_2 atoms at time t using the Bateman equation again, but this time for n=2:

$$\frac{dN_2}{dt} = \lambda_1 N_{1,0} e^{-\lambda_1 t} - \lambda_2 N_2. \tag{6.7}$$

To solve this, we can choose a general solution of the form:

$$N_2 = C_1 e^{-\lambda_1 t} - C_1 e^{-\lambda_2 t}, \tag{6.8}$$

where C_1 is a constant. By using this definition of N_2, we can incorporate it back into Equation 6.7 to achieve:

$$\begin{aligned} \frac{dN_2}{dt} &= \lambda_1 N_{1,0} e^{-\lambda_1 t} - \lambda_2 N_2 \\ -C_1 \lambda_1 e^{-\lambda_1 t} + C_1 \lambda_2 e^{-\lambda_2 t} &= \lambda_1 N_{1,0} e^{-\lambda_1 t} - \lambda_2 (C_1 e^{-\lambda_1 t} - C_1 e^{-\lambda_2 t}). \end{aligned} \tag{6.9}$$

By solving the above equation, we find that

$$C_1 = \frac{\lambda_1 N_{1,0}}{\lambda_2 - \lambda_1}, \tag{6.10}$$

and when combining Equations 6.10 and 6.8, we arrive at the expression for the number of N_2 atoms as a function of time:

$$N_2(t) = \frac{\lambda_1 N_{1,0}}{\lambda_2 - \lambda_1}(e^{-\lambda_1 t} - e^{-\lambda_2 t}). \tag{6.11}$$

We can further extend this scenario for the case where $N_1 \xrightarrow{\lambda_1} N_2 \xrightarrow{\lambda_2} N_3 \xrightarrow{\lambda_3} N_4$. Using the Bateman equation for n=3, we see that

$$\frac{dN_3}{dt} = \lambda_2 N_2 - \lambda_3 N_3. \tag{6.12}$$

Using a general solution in the form of:

$$N_3 = K_1 e^{-\lambda_1 t} + K_2 e^{-\lambda_2 t} - (K_1 + K_2) e^{-\lambda_3 t}, \tag{6.13}$$

where K_1 and K_2 are constants, and the definitions of N_2 from Equation 6.8 and C_1 from Equation 6.10, we can see that

$$K_1 = \frac{\lambda_1 \lambda_2 N_{1,0}}{(\lambda_2 - \lambda_1)(\lambda_3 - \lambda_1)}, \tag{6.14}$$

and

$$K_2 = \frac{\lambda_1 \lambda_2 N_{1,0}}{(\lambda_1 - \lambda_2)(\lambda_3 - \lambda_2)}. \tag{6.15}$$

Substituting these back into Equation 6.13 yields an expression for N_3 as a function of time:

$$\begin{aligned} N_3(t) = {} & \frac{\lambda_1 \lambda_2 N_{1,0}}{(\lambda_2 - \lambda_1)(\lambda_3 - \lambda_1)(\lambda_3 - \lambda_2)} \\ & \times \left(e^{-\lambda_1 t}(\lambda_3 - \lambda_2) + e^{-\lambda_2 t}(\lambda_3 - \lambda_1) - e^{-\lambda_3 t}(\lambda_1 - \lambda_2) \right). \end{aligned} \tag{6.16}$$

The Bateman equation can be used to solve a decay chain, and modified to solve branching decays, for any value of n. However, as one can imagine, for large values of n it can become quite challenging to find a solution by hand and is therefore often solved computationally.

6.1.2 Activity

The activity of the source, A, also known as the number of decays per second, is defined as

$$A(t) = -\frac{dN}{dt} = \lambda N(t). \tag{6.17}$$

We can then substitute Equation 6.6 into Equation 6.17 to achieve:

$$\begin{aligned} A(t) &= -\frac{dN}{dt} \\ &= \lambda N_0 e^{-\lambda t} \\ &= A_0 e^{-\lambda t}, \end{aligned} \tag{6.18}$$

where A_0 ($A_0 \equiv \lambda N_0$) is the initial activity of the source.

For scenarios such as

$$N_1 \xrightarrow{\lambda_1} N_2 \xrightarrow{\lambda_2} N_3 \xrightarrow{\lambda_3} N_4,$$

if we wish to find the activity of the second isotope, N_2, we simply multiply Equation 6.11 by λ_2. Likewise, in order to find the activity for N_3(t), we multiply Equation 6.16 by λ_3.

6.2 Radioisotope Production

In some cases, isotopes can be produced if a source of target atoms is exposed to a high neutron environment. In this situation an incoming neutron and a nucleus can combine to form a new compound nucleus. This process is known as neutron capture.

6.2.1 Neutron Capture

During neutron capture, the incident neutron and target nucleus combine to form a compound nucleus, shown in Figure 6.1, that is in an excited energy state. If the compound nucleus then decays to the ground state via the emission of a photon, the entire process is referred to as radiative capture, or (n, γ) process. However, the likelihood that

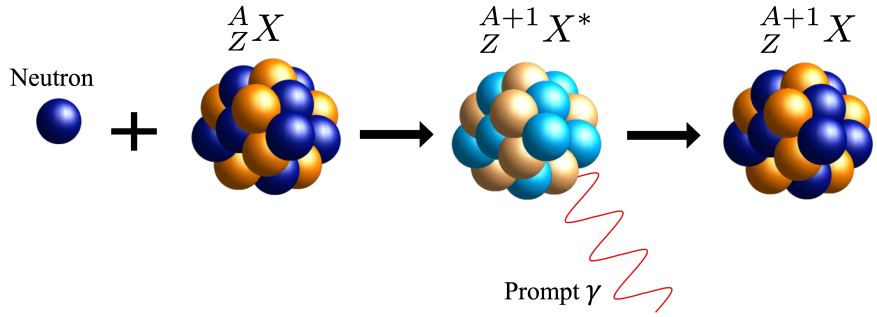

Figure 6.1: The radiative capture process wherein an incident neutron combines with a target nucleus to form an excited compound nucleus which then decays to the ground state via the emission of a gamma ray.

neutron capture will occur is a statistical process, i.e., the neutron capture cross-section can be used to describe the probability that a neutron of a specific energy will interact with the nucleus. The likelihood of such an event depends on the energy of the neutron as well as the isotope in question. However, it is generally seen that slower neutrons, like thermal neutrons, often have larger cross-sections. Thermal neutrons are those that are in thermal equilibrium with their surroundings at temperature T and at room temperature ($\sim$ 20 $^{\circ}$ C) they have a kinetic energy of $E_{neutron}$ = 0.025 eV [92]. Thermal neutrons have a neutron capture cross-section that is proportional to the inverse of their velocity ("1/v") [93] which implies that it is more likely that a neutron capture event will occur when the neutron is at slower speeds. An example of this is shown in Figure 6.2, which shows the neutron capture cross-section as a function of neutron energy. The "1/v" region, or the thermal neutron regime, clearly shows the decreasing cross-section as a function of increasing energy.

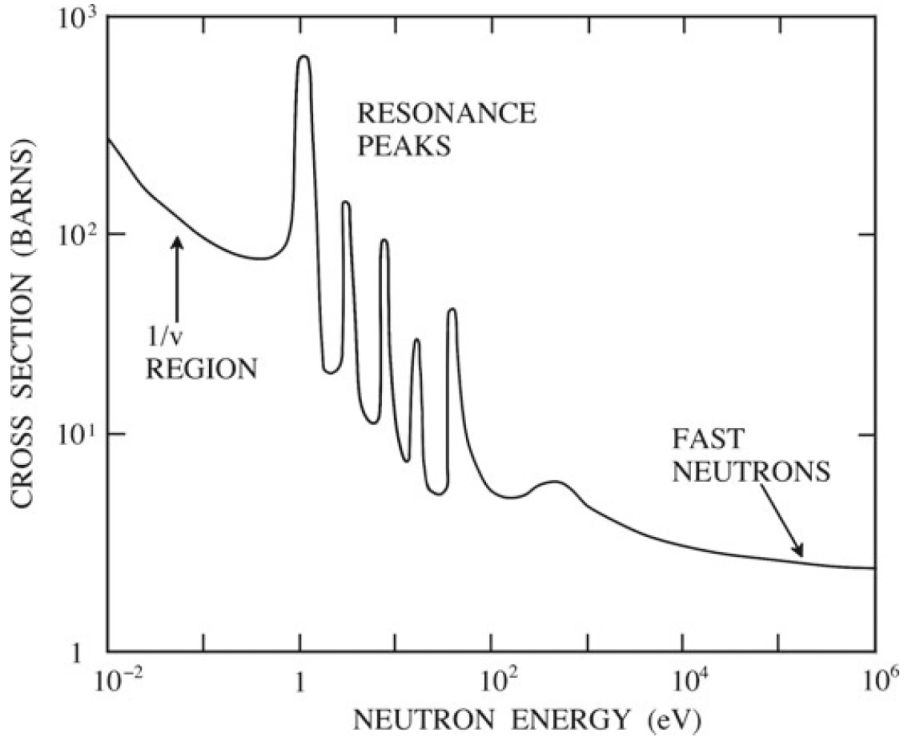

Figure 6.2: A plot of the radiative capture cross-section with respect to incident neutron energy. Highlighted on the plot is the "1/v" thermal neutron region. Plot sourced from [93].

6.2.2 Radioisotope Production Due to Radiative Capture

As previously mentioned, isotopes can be produced if a source of target atoms is exposed in a high neutron environment and neutron capture occurs. The rate at which these isotopes are produced is known as the production rate, P:

$$P = \Phi\sigma(E_{neutron})N_T \tag{6.19}$$

where Φ is the neutron flux (measured in neutrons·cm^{-2}· s^{-1}), σ is the neutron capture cross-section of the target atom (measured in barns, 1 barn = 10^{-24} cm^2), and N_T is the number of atoms in the target at time t [94]. However, this only accounts for the production of the isotope. If we want to calculate the total number of activated atoms (N') at time t, we need to account for the rate of production as well as the decay of the N' atoms. To

do this, we can add Equation 6.19 to Equation 6.5 to find the total net number of activated atoms [95]:

$$\begin{aligned} \frac{dN'}{dt} &= P - \lambda N'(t) \\ &= \Phi\sigma N_T - \lambda N'(t), \end{aligned} \tag{6.20}$$

where λ is the decay constant of the activated atoms.

To solve this ODE, we can choose a general solution of the form

$$N'(t) = a + be^{-\lambda t} \tag{6.21}$$

and apply it to Equation 6.20:

$$-\lambda be^{-\lambda t} = \Phi\sigma N_T - \lambda(a + be^{-\lambda t}), \tag{6.22}$$

which results in

$$a = \frac{\Phi\sigma N_T}{\lambda}. \tag{6.23}$$

If there are no activated atoms at $t = 0$, we can take the initial conditions to be $N'(t = 0) = 0$, and find that

$$a = -b = \frac{\Phi\sigma N_T}{\lambda},$$

which allows us to express the net number of activated atoms as a function of time as:

$$N'(t) = \frac{\Phi\sigma N_T}{\lambda}(1 - e^{-\lambda t}). \tag{6.24}$$

Lastly, we can write this in terms of the activity of the activated isotope:

$$\begin{aligned} A'(t) &= \lambda N'(t) \\ &= \Phi\sigma N_T(1 - e^{-\lambda t}). \end{aligned} \tag{6.25}$$

With this knowledge of producing radioisotopes from radiative capture, we can now apply this to the production of a ^{127}Xe calibration source.

Chapter 7

Production of a ^{127}Xe Calibration Source

In order to understand and characterize the SiPMs that are in LoLX, as well as those that will be used in nEXO, it is paramount to have a means to calibrate them. An ideal calibration source would be one that is long-lived enough in order to take data over a long period, have a Q-value lower than the $Q_{\beta\beta}$ value, and allow for *in situ* calibration and performance characterization of the SiPMs.

As previously discussed, one promising candidate is the radioisotope ^{127}Xe. ^{127}Xe is an attractive option as it is a relatively long-lived radioisotope, which means that it can continue to act as an *in situ* calibration source for longer than other radioisotopes, and it also has a small Q-value in comparison to that of $0\nu\beta\beta$ decay, indicating that it will not interfere or mask the $0\nu\beta\beta$ decay signal.

As ^{127}Xe is not a naturally occurring isotope, it must be produced by way of exposing the isotope ^{126}Xe to a source of thermal neutrons, i.e., radiative capture. However, there are challenges with this method, the primary ones being that pure ^{126}Xe can be hard to procure as well as costly. One way to circumvent this problem is to use natural Xe (^{nat}Xe) gas instead. The reasons for this is that the gas is cheaper to purchase than ^{126}Xe, and as shown in Figure 7.3 and in Table 7.1, ^{126}Xe is one of the isotopes that constitute ^{nat}Xe gas.

However, in order to create ^{127}Xe from the radiative capture on ^{126}Xe, we require a source of thermal neutrons. Fortunately, we have been in correspondence with the nuclear reactor director at the Royal Military College of Canada.

7.1 Royal Military College Nuclear Reactor

The Safe LOW Power c(K)ritical Experiment-2 (SLOWPOKE-2) is a 20 kW_{th} ^{235}U-fueled pool-type nuclear reactor [96]. Located at the Royal Military College of Canada (RMC) in Kingston, Ontario, the reactor, which became critical in 1985, serves both academic and educational purposes. The facilities are used in the instruction of RMC students, providing opportunities for scientific research, as well as training of the Canadian Armed Forces. Some of the work that is done at RMC includes neutron activation analysis, neutron radiography, as well as the production of some radioisotopes [97]. The reactor offers two different locations for samples to be irradiated. As seen in Figure 7.1 (B), there are inner sites within the beryllium annulus as well as outer sites beyond the annulus [98]. However, the use of these locations depends on the type of material to be irradiated as well as the dimension of the sample. In addition to these sites, larger objects can be lowered into the reactor pool with use of an elevator arm in order to be irradiated. While the neutron flux is lower in the reactor pool than in the inner/outer sites, it is still 1.9×10^{10} neutrons/cm^2/s, which is sufficient for the irradiation of the ^{nat}Xe gas.

Currently, the LoLX group at McGill has been in conversation with the SLOWPOKE-2 facility director regarding the use of their facilities to create a ^{127}Xe calibration source.

7.2 Canister Design

In order to irradiate a source at RMC a few requirements must be met: the canister the source is contained in must not be a pressure vessel, the canister must fit close to the reactor centerline, the canister must be able to withstand an aquatic environment $\sim$5.5

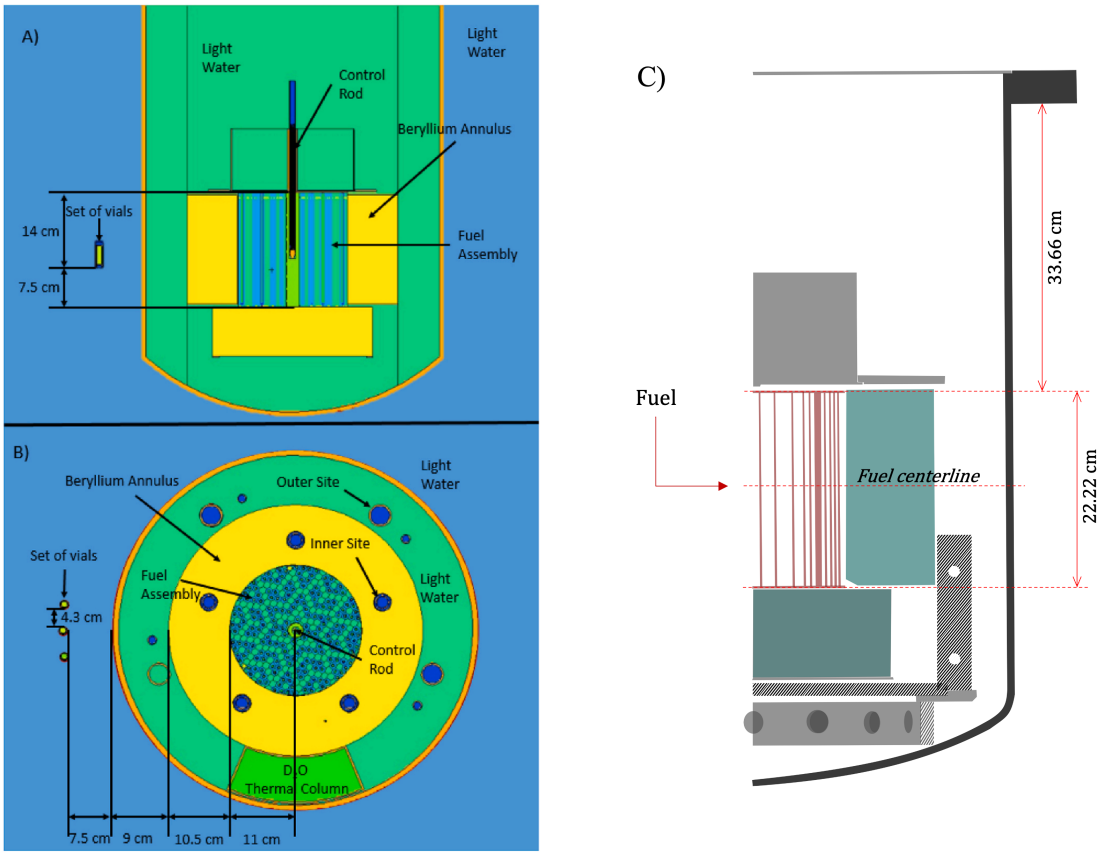

Figure 7.1: Schematic of the RMC reactor. (A) the side and (B) top view of the RMC reactor which highlight the location of the fuel rods, the beryllium annulus, as well as the inner and outer sites for sample irradiation. (A) and (B) sourced from [98]. (C) A cross section of the RMC reactor which shows some of the dimensions. The black, protruding edge of the reactor is under 5 m of water. (C) was graciously provided by RMC.

m below the waterline, and the material the source is contained within must not become highly radioactive when subjected to a neutron flux.

Due to the proposed size of our canister design, which will be elaborated upon later in this section, our canister must be irradiated in the reactor pool, and will therefore be placed under roughly ∼5.5 m of water. However, in order to place the canister close to the centerline of the reactor, the canister must be able to maneuver around a lip on the reactor, which can be seen in Figure 7.1 (C). A method for doing so is attaching a curved neck to the canister body that would allow for us to attach the neck to the elevator beam and still be able to get the canister close to the centerline.

The greatest of these concerns is fabricating a canister that will not become highly radioactive when exposed to the neutron flux. Previous work, as mentioned in Section 5.2, has been done on the creation of radioactive calibration sources with the use of nuclear reactors. However, in their work a stainless steel (SS) canister was used to contain the source, which is not ideal as SS can become highly radioactive (see Section 7.4.2 for more details). As such, it was suggested that the canister should primarily consist of aluminum as it is not as likely to become as radioactive as SS. However, conversations with RMC did indicate that SS would be permissible so long as few SS components were used and they were located roughly one meter away from the fuel centerline.

Extensive online research showed that it would not be possible to purchase a pre-fabricated canister that met the necessary design requirements. As such, it was decided that we should design the canister ourselves and then have the parts machined and assembled.

Based upon size limitations due to the reactor geometry, it was decided that the body of the canister would be a cylinder and consist of the aluminum alloy Al 6061 with an inner diameter of 4.5″, an outer diameter of 5″, and a height of 8″. Two Al 6061 disks of outer diameter 5″ and thickness 0.5″ will function as the bottom and top of the canister, with the top disk featuring a hole of radius 0.44″ at the centre where a 6061 aluminum pipe of 1/2 pipe size will be welded. A series of subsequent Al 6061 pipes will then lead away from the canister and transition to 1/2″ stainless steel tubing via an aluminum pipe to stainless steel tubing coupler from High Energy Metals, Inc. and then end with a VCR connection and valve (please see Appendix A for more details on the canister components as well as the proposed assembly instructions). Figure 7.2 shows a breakdown of this design and its dimensions will result in an internal canister body volume of 127.23 inch^3, or 2.09x10^{-3} m^3, and a weight of just over 2 kg.

Due to the requirements that the canister must not be a pressure vessel ($P > 2$atm), we plan to operate at a pressure of 1.5 atm. Using this, the canister volume, and assuming a temperature of 300 K we can use the Ideal Gas law ($PV = NkT$) to calculate the number

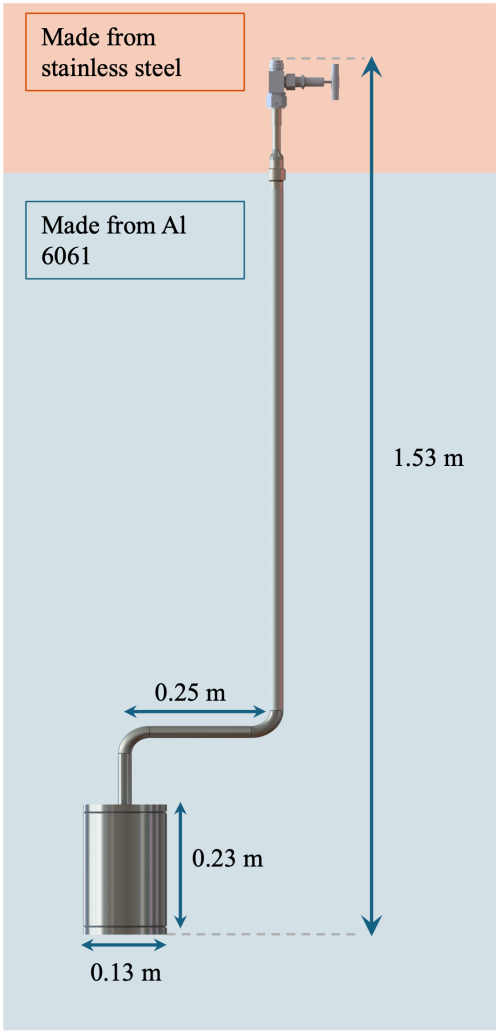

Figure 7.2: The proposed design for the canister which will be filled with ^{nat}Xe gas and then subjected to a high neutron flux at the RMC reactor.

of ^{nat}Xe atoms within the canister. Lastly, we can use the atomic mass of ^{nat}Xe [99] to calculate that there should be ~16.5 g of ^{nat}Xe in the canister.

7.3 Natural Xenon

Natural Xe comprises of nine different isotopes, with seven being stable and three having incredibly long half-lives: ^{124}Xe, ^{134}Xe, and ^{136}Xe. Figure 7.3 shows the isotopic abundance of ^{nat}Xe. The natural abundance for the nine isotopes of ^{nat}Xe, as well as their

Table 7.1: Properties of isotopes present within ^{nat}Xe. Thermal neutron capture cross-sections were sourced from the TENDL [102] and ENDF [101] online libraries and the natural abundance was sourced from the Nubase [100] online library.

	^{124}Xe	^{126}Xe	^{128}Xe	^{129}Xe	^{130}Xe	^{131}Xe	^{132}Xe	^{134}Xe	^{136}Xe
Natural abundance (%)	0.095	0.089	1.91	26.4	4.1	21.2	26.9	10.4	8.6
Thermal neutron capture cross-section (barns)	148.6	3.49	5.20	21.0	4.78	90.1	0.40	0.27	0.26

thermal neutron capture cross sections, which were obtained from the online libraries Nubase [100] and ENDF [101]. As shown in Table 7.1, the thermal neutron capture cross sections is expressed in the unit "barns", where 1 barn is equivalent to 10^{-24} cm^2.

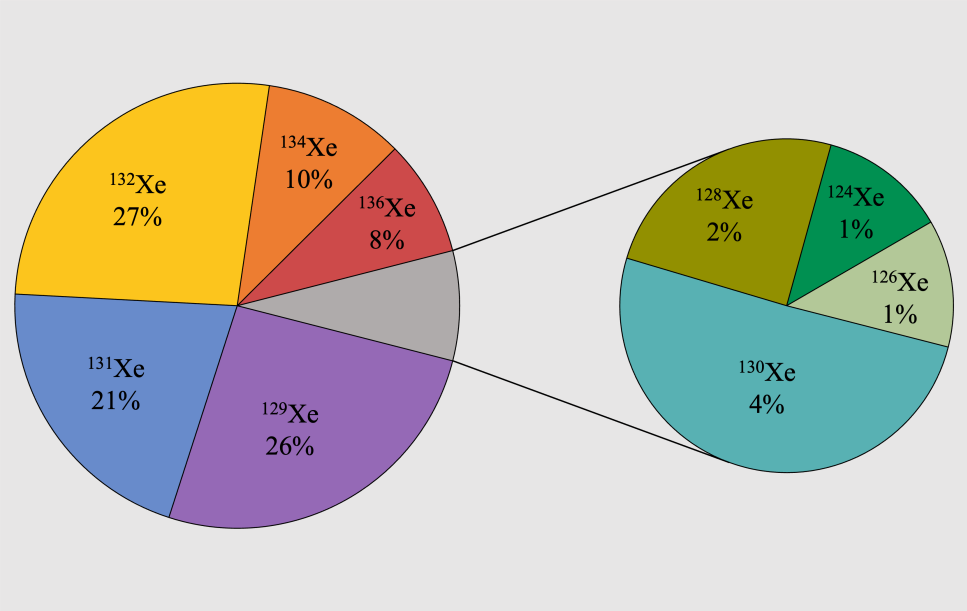

Figure 7.3: The elemental composition of ^{nat}Xe. Values were sourced from the Nubase [100] online library.

Subjecting the ^{nat}Xe to a thermal neutron flux would result in the neutron activation of ^{126}Xe and therefore the production of ^{127}Xe. However, that is not the only expected

radioisotope to result from the irradiation. Table 7.2 shows the predicted radioisotopes as well as their respective decay chains that we expect from irradiating ^{nat}Xe gas with thermal neutrons.

Due to the presence of these radioisotopes it was decided that it would be advantageous to let the Xe canister sit and rest at RMC after the irradiation period, for upwards of 100 days, before being moved to McGill. This would allow for most of the other radioisotopes to decay away, which is possible due in part to the relatively long half-life of ^{127}Xe.

Table 7.2: Radioisotope properties resulting from ^{nat}Xe exposure to thermal neutrons. Listed are the most-likely produced radioisotopes, their half-lives, their production mode, as well as their respective decay chains. Data was sourced from the ENSDF [16] online library. EC and IT refer to electron capture and internal transition, respectively.

Radioisotope	**Half-life**	**Production mode**	**Decay chain**
^{125}Xe	16.9 hrs.	^{124}Xe(n, γ)^{125}Xe	^{125}Xe $\xrightarrow[\beta^+(16.9\text{ h})]{}$ ^{125}I $\xrightarrow[\text{EC}(55\text{ d})]{}$ ^{125}Te (Stable)
^{127}Xe	36.3 days	^{126}Xe(n, γ)^{127}Xe	^{127}Xe $\xrightarrow[\text{EC}(36.3\text{ d})]{}$ ^{127}I (Stable)
^{129m}Xe	8.9 days	^{128}Xe(n, γ)^{129m}Xe	^{129m}Xe $\xrightarrow[\text{IT}(8.9\text{ d})]{}$ ^{129}Xe (Stable)
^{131m}Xe	11.9 days	^{130}Xe(n, γ)^{131m}Xe	^{131m}Xe $\xrightarrow[\text{IT}(11.9\text{ d})]{}$ ^{131}Xe (Stable)
^{133}Xe	5.2 days	^{132}Xe(n, γ)^{133}Xe	^{133}Xe $\xrightarrow[\beta^-(5.2\text{ d})]{}$ ^{133}Cs (Stable)
^{135}Xe	9.1 hrs.	^{134}Xe(n, γ)^{135}Xe	^{135}Xe $\xrightarrow[\beta^-(9.1\text{ h})]{}$ ^{135}Cs $\xrightarrow[\beta^-(2.3\times10^6\text{ y})]{}$ ^{135}Ba (Stable)
^{137}Xe	3.8 mins.	^{136}Xe(n, γ)^{137}Xe	^{137}Xe $\xrightarrow[\beta^-(3.8\text{ m})]{}$ ^{137}Cs $\xrightarrow[\beta^-(30.1\text{ y})]{}$ ^{137}Ba (Stable)

It was decided that a final ^{127}Xe activity, after a 100 day rest period, of 1.5 kBq would be sufficient as a calibration source for use in LoLX. As such, we needed to find out what initial activity (after ending irradiation) is required to achieve this.

Using Equation 6.18, along with the half-life of ^{127}Xe (shown in Table 7.2), it was determined that the desired activity immediately after ending irradiation was 10 kBq. Knowing this, we had to find out how long we had to irradiate our canister in order to achieve this desired activity.

As before, we can use the Ideal Gas Law to calculate the expected number of ^{nat}Xe atoms inside the canister. Then, using the natural abundance of ^{nat}Xe isotopes, we can calculate the initial number of ^{126}Xe atoms. Using that, along with the thermal neutron cross section, the half-life (shown in Table 7.2), the RMC neutron flux (1.9x10^{10} neutrons/cm^{2}s), and Equation 6.25, we can solve for the amount of time it would take for the ^{127}Xe to achieve an activity of 10 kBq. This results in $\sim$ 170 minutes, or $\sim$ 2.8 hours.

7.3.1 Activity of ^{nat}Xe Gas

As previously mentioned, ^{126}Xe is not the only isotope we need to consider while irradiating ^{nat}Xe gas. Therefore, it is important to calculate the expected activities for each of the radioisotopes.

All source code for this thesis can be found on the Brunner Neutrino Lab GitHub [1]; however, an example of the code, presented as Python pseudocode, is shown in Figure 7.4 where Equation 6.20 is used to calculate the number of daughter atoms that are created per time increment dt that the parent isotope is irradiated for. The number of newly-created daughter atoms is taken into account, and subsequently the number of parent atoms is adjusted. Then, the decay of the daughter isotope is taken into consideration, and finally the number of atoms is converted into activity. Figure 7.5 shows the expected activities of the radioisotopes during irradiation.

[1] Brunner Neutrino Lab GitHub: `https://github.com/Brunner-neutrino-lab/Xe-127-Calibration-Source/tree/main`

```
def neutron_induced_activity(flux, time, XS, decay_const, parent, daughter, Activity, NXe):
    '''
    Calculates the activity of a daughter isotope for a given parent, neutron flux, and irradiation time.

    Parameters:
    flux : Neutron flux. Units in neutrons/cm^2/s.
    time : Time that the isotopes are irradiated for. Units in s.
    XS: Dictionary of the parent isotopes with their cross sections for thermal neutron capture. Units in cm^2.
    decay_const : Dictionary of the decay constants for the daughter isotopes. Units in s^-1.
    parent : String. The name of the parent isotope.
    daughter : String. The name of the daughter isotope.
    Activity : Dictionary that contains the activities for all of the isotopes. Units in kBq.
    NXe : Dictionary that contains the number of atoms for all of the isotopes.

    Returns:
    Activity : Dictionary that contains the activities for all of the isotopes, newly filled for the daughter isotope
    NXe : Dictionary that contains the number of atoms for all of the isotopes, newly filled for the daughter isotope

    '''

    lamb = decay_const[daughter] # Decay constant of the daughter

    dt = time[1] - time[0] # Calculates the time increment we will be working with

    xs = XS[parent] # Cross section of the parent for thermal neutron capture

    for i in range(1, len(time)):

        num_created_atoms= xs * flux * NXe[parent][i-1] * dt # Num. of daughter atoms produced via neutron activation

        total_new_atoms= (xs * flux * NXe[parent][i-1] - lamb * NXe[daughter][i-1]) * dt

        NXe[parent][i] = NXe[parent][i-1] - num_created_atoms # Recalculates the new num. of parent atoms remaining

        NXe[daughter][i] = NXe[daughter][i-1] + total_new_atoms # Recalculates the new num. of daughter atoms

    Activity[daughter] = NXe[daughter] * lamb/1000 # Calculates the activity of the daughter in kBq

    return Activity, NXe
```

Figure 7.4: Depiction of the Python pseudocode function that was used to calculate the activity of the radioisotope. The function not only calculates the number of activated daughter atoms, but calculates the number of parent atoms after neutron activation for each time step.

Importantly, as can be seen from Figure 7.5, all of the radioisotopes present have activities larger than the desired ^{127}Xe. This is why, as was previously mentioned, we plan to leverage the somewhat long half-life of ^{127}Xe and let the canister rest for upwards of 100 days. By taking this measure, it should allow for most of the radioisotopes to either decay away or at least decrease in activity.

To confirm this, the expected activities of the radioisotopes were calculated for a time span of 100 days. For the majority of the radioisotopes, Equation 6.18 was implemented

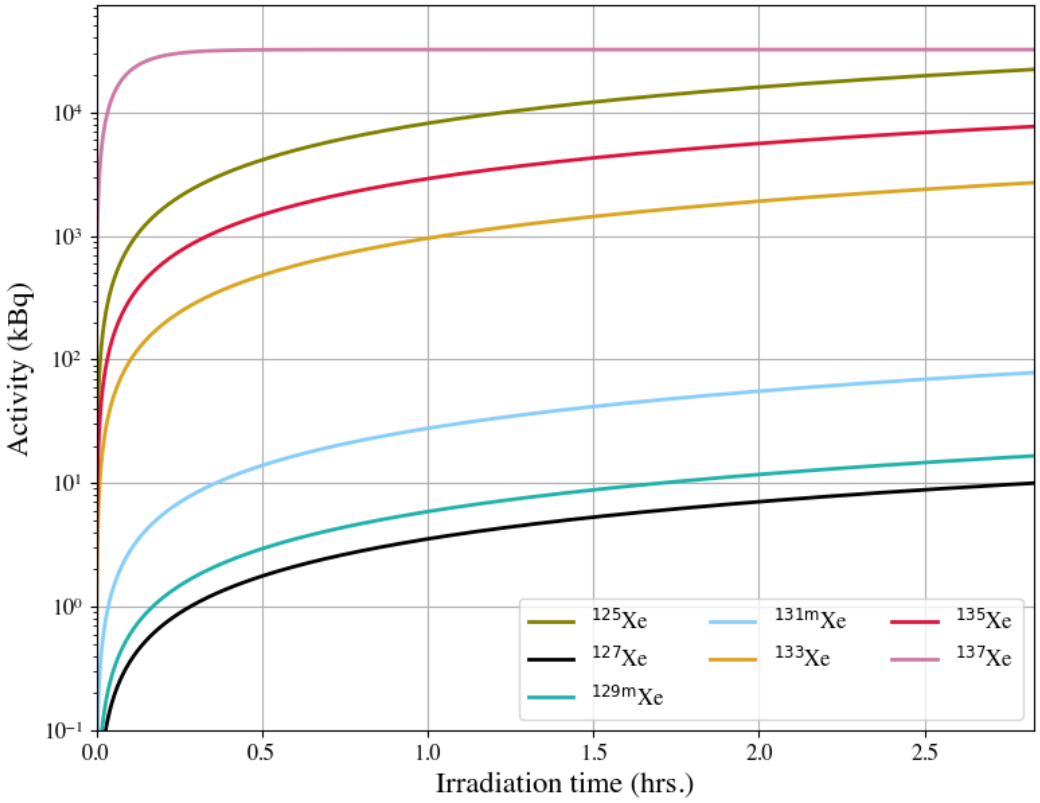

Figure 7.5: Expected activities for radioisotopes resulting from irradiating ^{nat}Xe gas over a period of 2.8 hours.

in Python to calculate the decaying activities. However, for the cases of ^{125}Xe, ^{135}Xe, and ^{137}Xe (which decay to ^{125}I, ^{135}Cs, and ^{137}Cs respectively), Equation 6.11 (the Bateman equation for the case where n=2) was used. Figure 7.6 depicts the Python pseudocode that was implemented in order to calculate the activities in these decay chains.

Figure 7.7 shows the activities for each of the radioisotopes over a 100 day period. The production and subsequent decay of ^{125}I to ^{125}Te is visible on the plot. However, due to the long half-life of ^{135}Cs, the greatest activity it reaches is $\sim$ 3.5x10^{-3} Bq and is therefore not shown as it is essentially negligible. Likewise, neither the decay of ^{137}Xe and ^{137}Cs are shown for similar reasons. The decay of ^{137}Xe occurs so quickly that there are only traces

```
def calc_decay_chain_for_NB(time, daughter_A, daughter_B,  decay_const, DecayingActivity, N):
        '''
        Calculates the decaying activity of N_B in the decay chain:
                        N_A → N_B → N_C
        where N_C is stable.

        Parameters:
        time : Time that the radioisotopes are left to decay for. Units in s.
        daughter_A: String. The name of the daughter radioisotope that was produced via thermal neutron capture. N_A in the decay
        chain.
        daughter_B: String. The name of the new daughter radioisotope that is produced from the decay of the previous daughter.   N_B in
        the decay chain.
        decay_const : Dictionary of the decay constants for the  radioisotopes. Units in s-1.
        DecayingActivity : Dictionary that contains the decaying activities for all of the isotopes. Units in kBq.
        N : Dictionary that contains the number of atoms for all of the isotopes during the irradiation period.

        Returns:
        DecayingActivity : Dictionary. Contains the decaying activities for all of the isotopes, newly filled for the daughter_B
        isotope. Units in kBq.

        '''
        DecayingActivity[daughter_B] = [] #Creates an empty array in the DecayingActivity dictionary for daughter_B
        lam_A = decay_const[daughter_A] # Decay constant of  daughter_A
        lam_B = decay_const[daughter_B] # Decay constant of daughter_B
        for i in range(len(time)):
                a = lam_B* N[daughter_A][-1] * (np.e**(-lam_A * time[i]) - np.e**(-lam_B * time[i])) * lam_A / (lam_B - lam_A)
                # Calculates the activity of daughter_B
                DecayingActivity[daughter_B].append(a/1000) # Converts the activity to kBq and adds it to the dictionary array


        return DecayingActivity
```

Figure 7.6: Python pseudocode to calculate the activity of the isotope N_B for the decay chain $N_A \xrightarrow{\lambda_A} N_B \xrightarrow{\lambda_B} N_C$ where N_C is stable. The activity was calculated by multiplying the Bateman equation for the case where n=2 (Equation 6.11) by λ_B.

left after irradiation has finished, and similarly the production of ^{137}Cs only achieves a largest activity of 7.8 Bq before it begins to decay away.

The expected activities for each of the radioisotopes immediately after ending irradiation and for 10, 50, and 100 days afterwards is shown in Table 7.3. Only activities that are greater than 10^{-6} kBq are shown in Table 7.3, and anything less than that is denoted by the "$\sim$" symbol. The "—-" horizontal line for ^{125}I, ^{135}Cs, and ^{137}Cs indicates that those radioisotopes are only present during the decay of their parent radionuclides, and therefore very little is present at the moment that irradiation ceases.

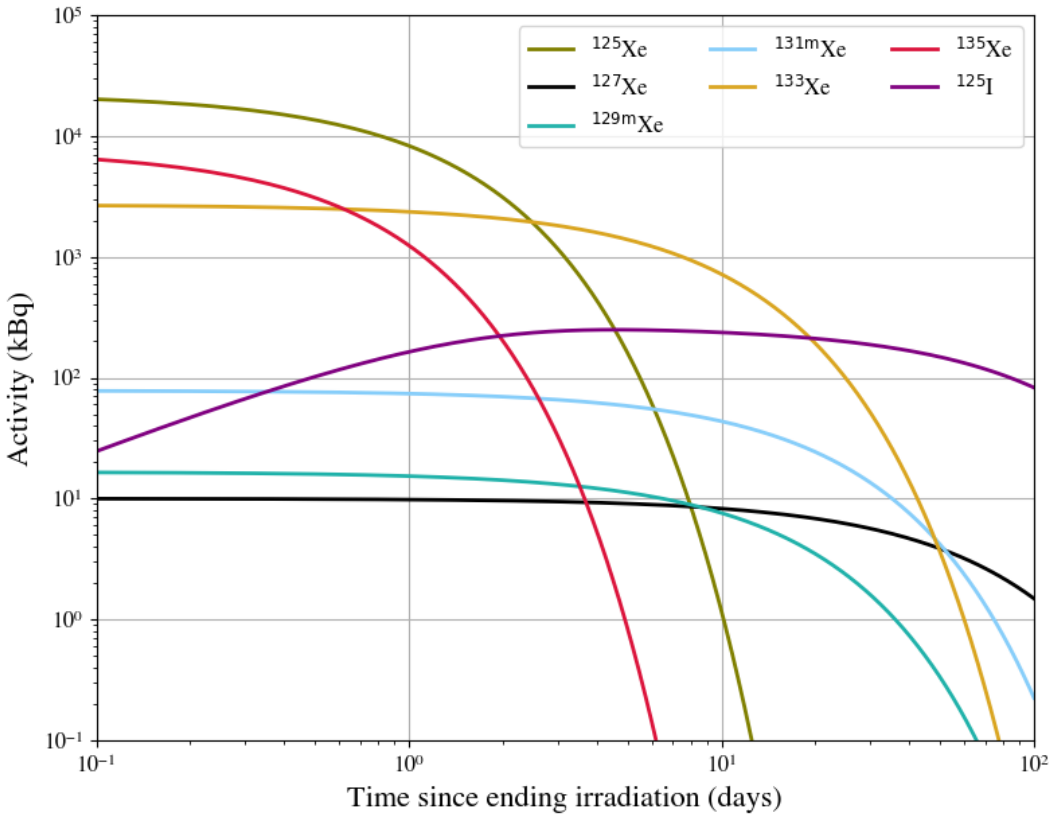

Figure 7.7: The expected activities of the radioisotopes from irradiated ^{nat}Xe over a period of 100 days after ending irradiation. It should be noted that ^{135}Cs, ^{137}Cs (resulting from the decays of ^{135}Xe and ^{137}Xe respectively), and ^{137}Xe are not shown in the plot as they decay too quickly to trace amounts. However, the production of ^{125}I from the decay of ^{125}Xe is shown.

Table 7.3: Xe radioisotope activities immediately after ending irradiation and then for 10/50/100 days after ending irradiation. Activities less than 10^{-6} kBq are denoted as $\sim$. Radioisotopes that are only present once their parent begins to decay are symbolized by —-.

	Activity after ending irradiation (kBq)	**Activity after ending irradiation for:** 10 days (kBq)	50 days (kBq)	100 days (kBq)
^{125}Xe	2.22x10^{4}	1.18	$\sim$	$\sim$
^{127}Xe	10.00	8.27	3.86	1.49
^{129m}Xe	16.60	7.60	0.33	6.76x10^{-3}
^{131m}Xe	78.32	43.61	4.19	0.22
^{133}Xe	2.69x10^{3}	7.18x10^{2}	3.64	4.94x10^{-3}
^{135}Xe	7.67x10^{3}	9.52x10^{-5}	$\sim$	$\sim$
^{137}Xe	3.21x10^{4}	$\sim$	$\sim$	$\sim$
^{125}I	———	2.37x10^{2}	1.48x10^{2}	82.87
^{135}Cs	———	3.49x10^{-6}	3.49x10^{-6}	3.49x10^{-6}
^{137}Cs	———	7.75x10^{-3}	7.73x10^{-3}	7.70x10^{-3}

It can be seen that at the end of the 100 days that ^{129m}Xe, ^{133}Xe, and ^{137}Cs have an activity of $\mathcal{O}(1\,\text{Bq})$ while ^{136}Cs has an activity of $\mathcal{O}(1\,\text{mBq})$. The other remaining radioisotopes are: 0.22 kBq of ^{131m}Xe, 82.87 kBq of ^{125}I, and 1.49 kBq of ^{127}Xe. Such small amounts of ^{131m}Xe should be permissible, but filtering the irradiated $^{\text{nat}}$Xe gas will be done prior to deployment in LoLX in the hopes to remove the ^{125}I and ^{131m}Xe.

7.4 Canister Activity

As was mentioned earlier in Section 7.2, it was decided that using an aluminum canister to contain the $^{\text{nat}}$Xe gas would be preferable as it would become less activated than stainless steel. However, it would be remiss to make the assumption that the canister would be completely non-radioactive after irradiation. The study of activation of the canister is presented in this section.

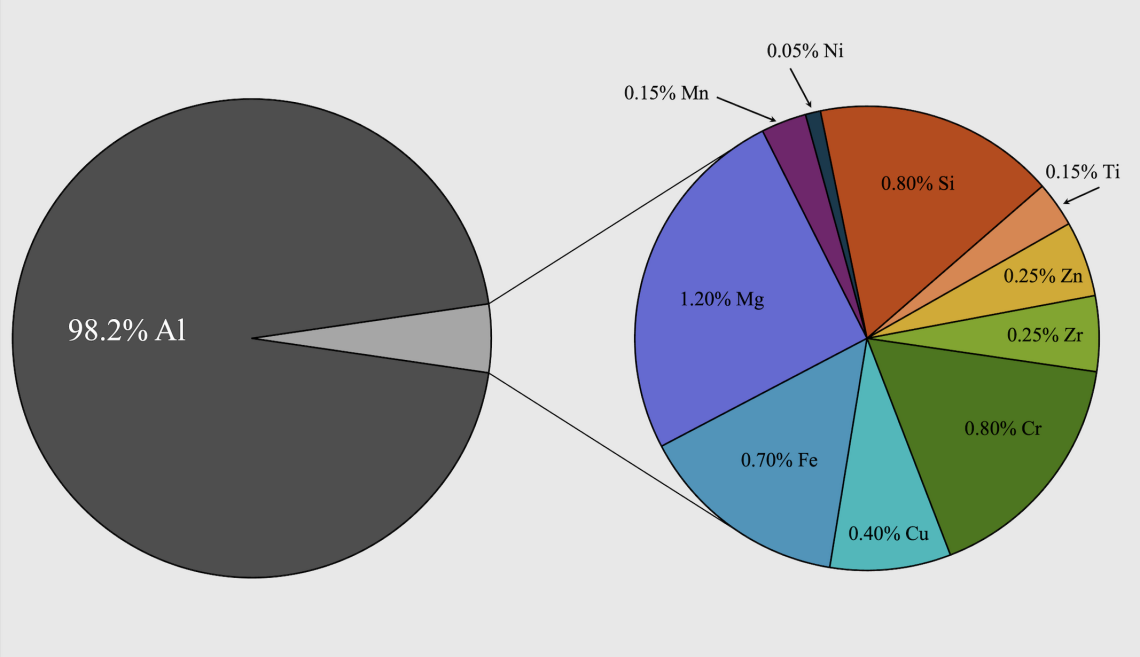

Figure 7.8: The elemental composition of Al 6061 as specified according to the supplier [103]. The maximum elemental percentages were used to account for deviations in the Al 6061 composition.

7.4.1 Activity of Al 6061

The material that will be used to contain the ^{nat}Xe gas is Al 6061, and as an aluminum alloy, it comprises of more elements than just aluminum. The composition of Al 6061 can vary with suppliers, which is why the breakdown of the elemental composition as shown in Figure 7.8 features the percentages claimed by a supplier [103].

Due to the large number of isotopes within Al 6061, it is important to note which ones may become radioactive once subjected to a neutron flux. Table 7.4 lists which isotopes will undergo neutron capture to produce a radioisotope, the elemental fraction of Al 6061, the isotope fraction, as well as the thermal neutron capture cross-section (for neutrons at an energy of 0.025 eV). All of the information in this table was sourced from the ENDF and Nubase online libraries.

Table 7.5 shows the radioisotopes that are produced from neutron capture on the Al 6061 isotopes, their half-lives, as well as their respective decay chains.

Table 7.4: Properties of isotopes present within Al 6061 that produce radioisotopes when subjected to a thermal neutron flux. Isotope fractions and cross-sections sourced from the ENDF [101] and Nubase [100] online libraries. Al 6061 composition sourced from supplier [103].

	Elemental fraction of Al 6061 (by weight)	**Isotope fraction**	**Thermal neutron capture cross-section (barns)**
^{27}Al	0.982	1	0.233
^{26}Mg	0.012	0.11	0.038
^{30}Si	0.008	0.031	0.108
^{54}Fe	0.007	0.0585	2.267
^{58}Fe	0.007	0.0028	1.315
^{63}Cu	0.004	0.692	4.500
^{65}Cu	0.004	0.309	2.162
^{50}Cr	0.008	0.0434	15.501
^{54}Cr	0.008	0.0237	0.414
^{64}Zn	0.0025	0.492	0.792
^{68}Zn	0.0025	0.185	1.072
^{70}Zn	0.0025	0.006	0.092
^{50}Ti	0.0015	0.0518	0.181
^{55}Mn	0.0015	1	13.361
^{92}Zr	0.0025	0.171	0.226
^{94}Zr	0.0025	0.174	0.050
^{96}Zr	0.0025	0.028	0.020

Table 7.5: Radioisotopes produced in thermal neutron capture on isotopes within Al 6061. Half-lives and decay chains were sourced from the ENSDF [16] online database. EC and IT refer to electron capture and internal transition, respectively. It should be noted that both ^{64}Cu and ^{93}Zr have two possible decay modes and the likelihoods for each decay are displayed next to them.

Radioisotope	Half-life	Decay chain
^{28}Al	2.2 mins.	$^{28}\mathrm{Al} \xrightarrow[\beta^-(2.2\,\mathrm{m})]{} {}^{28}\mathrm{Si}\ (\mathrm{Stable})$
^{27}Mg	9.4 mins.	$^{27}\mathrm{Mg} \xrightarrow[\beta^-(9.4\,\mathrm{m})]{} {}^{27}\mathrm{Al}\ (\mathrm{Stable})$
^{31}Si	2.6 hrs.	$^{31}\mathrm{Si} \xrightarrow[\beta^-(2.6\,\mathrm{h})]{} {}^{31}\mathrm{P}\ (\mathrm{Stable})$
^{55}Fe	2.7 yrs.	$^{55}\mathrm{Fe} \xrightarrow[\mathrm{EC}(2.7\,\mathrm{y})]{} {}^{55}\mathrm{Mn}\ (\mathrm{Stable})$
^{59}Fe	44.5 days	$^{59}\mathrm{Fe} \xrightarrow[\beta^-(44.5\,\mathrm{d})]{} {}^{59}\mathrm{Co}\ (\mathrm{Stable})$
^{64}Cu	12.7 hrs.	$(61.52\%)\ {}^{64}\mathrm{Cu} \xrightarrow[\beta^+(12.7\,\mathrm{h})]{} {}^{64}\mathrm{Ni}\ (\mathrm{Stable})$ $(38.48\%)\ {}^{64}\mathrm{Cu} \xrightarrow[\beta^-(12.7\,\mathrm{h})]{} {}^{64}\mathrm{Zn}\ (\mathrm{Stable})$
^{66}Cu	5.1 mins.	$^{66}\mathrm{Cu} \xrightarrow[\beta^-(5.1\,\mathrm{m})]{} {}^{66}\mathrm{Zn}\ (\mathrm{Stable})$
^{51}Cr	27.7 days	$^{51}\mathrm{Cr} \xrightarrow[\mathrm{EC}(27.7\,\mathrm{d})]{} {}^{51}\mathrm{V}\ (\mathrm{Stable})$
^{55}Cr	3.5 mins.	$^{55}\mathrm{Cr} \xrightarrow[\beta^-(3.5\,\mathrm{m})]{} {}^{55}\mathrm{Mn}\ (\mathrm{Stable})$
^{69}Zn	56.4 mins.	$^{69}\mathrm{Zn} \xrightarrow[\beta^-(56.4\,\mathrm{m})]{} {}^{69}\mathrm{Ga}\ (\mathrm{Stable})$
^{71}Zn	2.4 mins.	$^{71}\mathrm{Zn} \xrightarrow[\beta^-(2.4\,\mathrm{m})]{} {}^{71}\mathrm{Ga}\ (\mathrm{Stable})$
^{51}Ti	5.8 mins.	$^{51}\mathrm{Ti} \xrightarrow[\beta^-(5.8\,\mathrm{m})]{} {}^{51}\mathrm{V}\ (\mathrm{Stable})$
^{56}Mn	2.6 hrs.	$^{56}\mathrm{Mn} \xrightarrow[\beta^-(2.6\,\mathrm{h})]{} {}^{56}\mathrm{Fe}\ (\mathrm{Stable})$
^{93}Zr	1.5x10^6 yrs.	$(73\%)\ {}^{93}\mathrm{Zr} \xrightarrow[\beta^-(1.5\times10^6\,\mathrm{y})]{} {}^{93m}\mathrm{Nb} \xrightarrow[\mathrm{IT}(16.1\,\mathrm{y})]{} {}^{93}\mathrm{Nb}\ (\mathrm{Stable})$ $(27\%)\ {}^{93}\mathrm{Zr} \xrightarrow[\beta^-(1.5\times10^6\,\mathrm{y})]{} {}^{93}\mathrm{Nb}\ (\mathrm{Stable})$
^{95}Zr	64.0 days	$^{95}\mathrm{Zr} \xrightarrow[\beta^-(64\,\mathrm{d})]{} {}^{95}\mathrm{Nb} \xrightarrow[\beta^-(35\,\mathrm{d})]{} {}^{95}\mathrm{Mo}\ (\mathrm{Stable})$
^{97}Zr	16.7 hrs.	$^{97}\mathrm{Zr} \xrightarrow[\beta^-(16.7\,\mathrm{h})]{} {}^{97m}\mathrm{Nb} \xrightarrow[\mathrm{IT}(52.7\,\mathrm{s})]{} {}^{97}\mathrm{Nb} \xrightarrow[\beta^-(72.1\,\mathrm{m})]{} {}^{97}\mathrm{Mo}\ (\mathrm{Stable})$

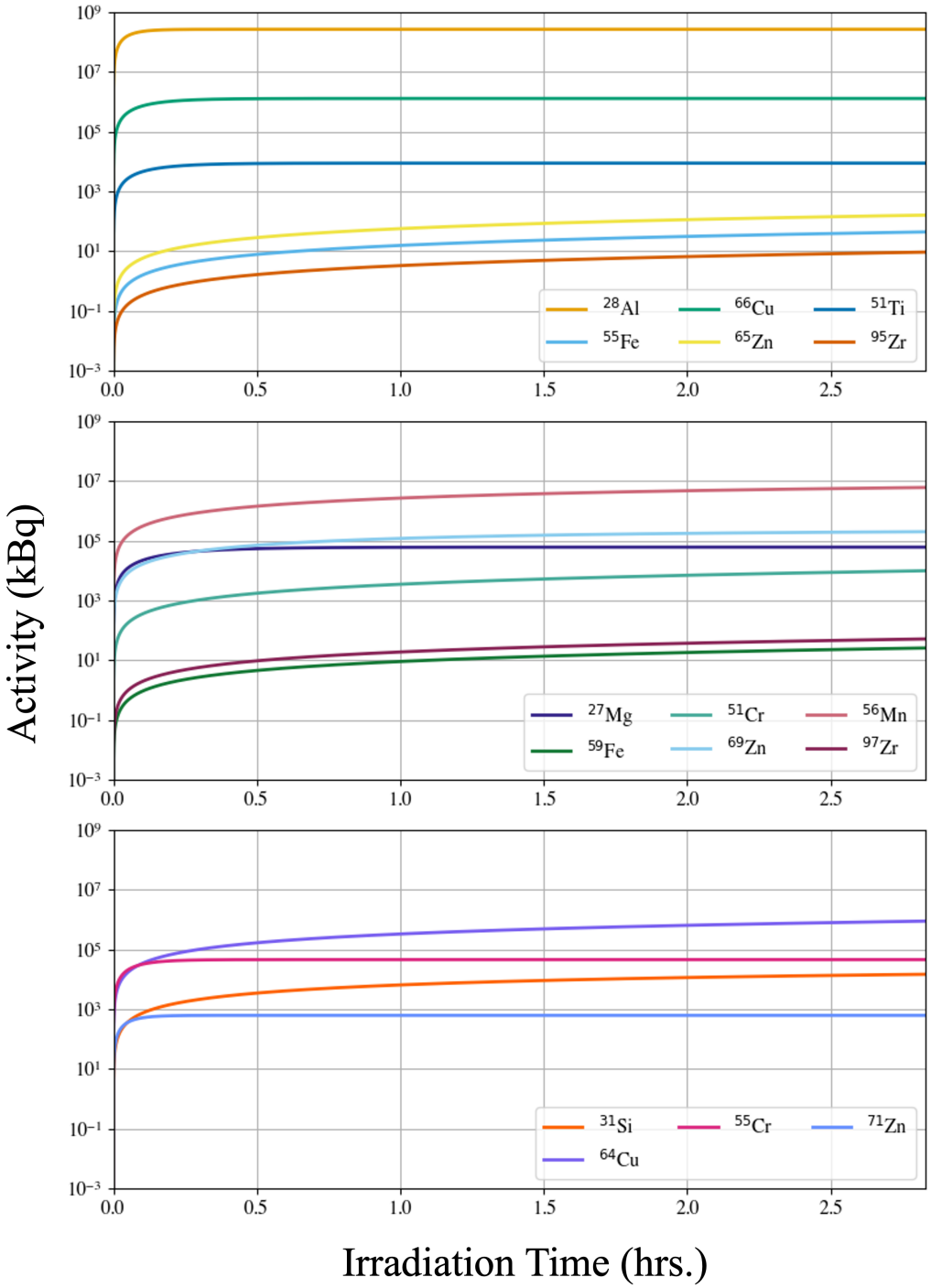

Figure 7.9: The expected activity of the radioisotopes from Al 6061 as a function of irradiation time.

In order to estimate the activity of Al 6061, the Al volumes of each of the canister components were calculated. Then, knowing the density of Al 6061, the mass of the canister

was determined. Using that, as well as the isotopic and elemental fractions of Al 6061 in Table 7.4, the amounts of each of the isotopes could be calculated along with the expected number of atoms for each isotope. By using Equation 6.24 as well as the aforementioned reactor pool thermal neutron flux and thermal neutron cross sections, we calculated the expected activities for each of the radioisotopes. Figure 7.9 shows the expected activity for the radioisotopes as a function of irradiation time, and Figure 7.10 shows the expected activity of the radioisotopes over a period of 100 days after ending irradiation. Calculating the decaying activities for the Al canister followed the same methods outlined in Section 7.3; however, a different method had to be used to calculate the activity of ^{97}Nb.

Figure 7.11 shows the Python pseudocode that was used to calculate the decaying activity of ^{97}Nb in the decay chain ^{97}Zr $\rightarrow$ ^{97m}Nb $\rightarrow$ ^{97}Nb $\rightarrow$ ^{97}Mo using the Bateman equation for the case where n = 3 (Equation 6.16). It is important to note that during the decays of ^{95}Zr and ^{97}Zr, both ^{95}Nb and ^{97}Nb are produced and subsequently decay as well, as shown in Table 7.5. ^{93}Zr also undergoes subsequent decays; however, due to its long half-life ($T_{1/2}$=1.5x10^6 years [16]), the resulting activity of ^{93m}Nb is $\mathcal{O}(10\,\mu\text{Bq})$. This is why, in Figure 7.10, its activity could not be plotted alongside the rest of the radioisotope activities.

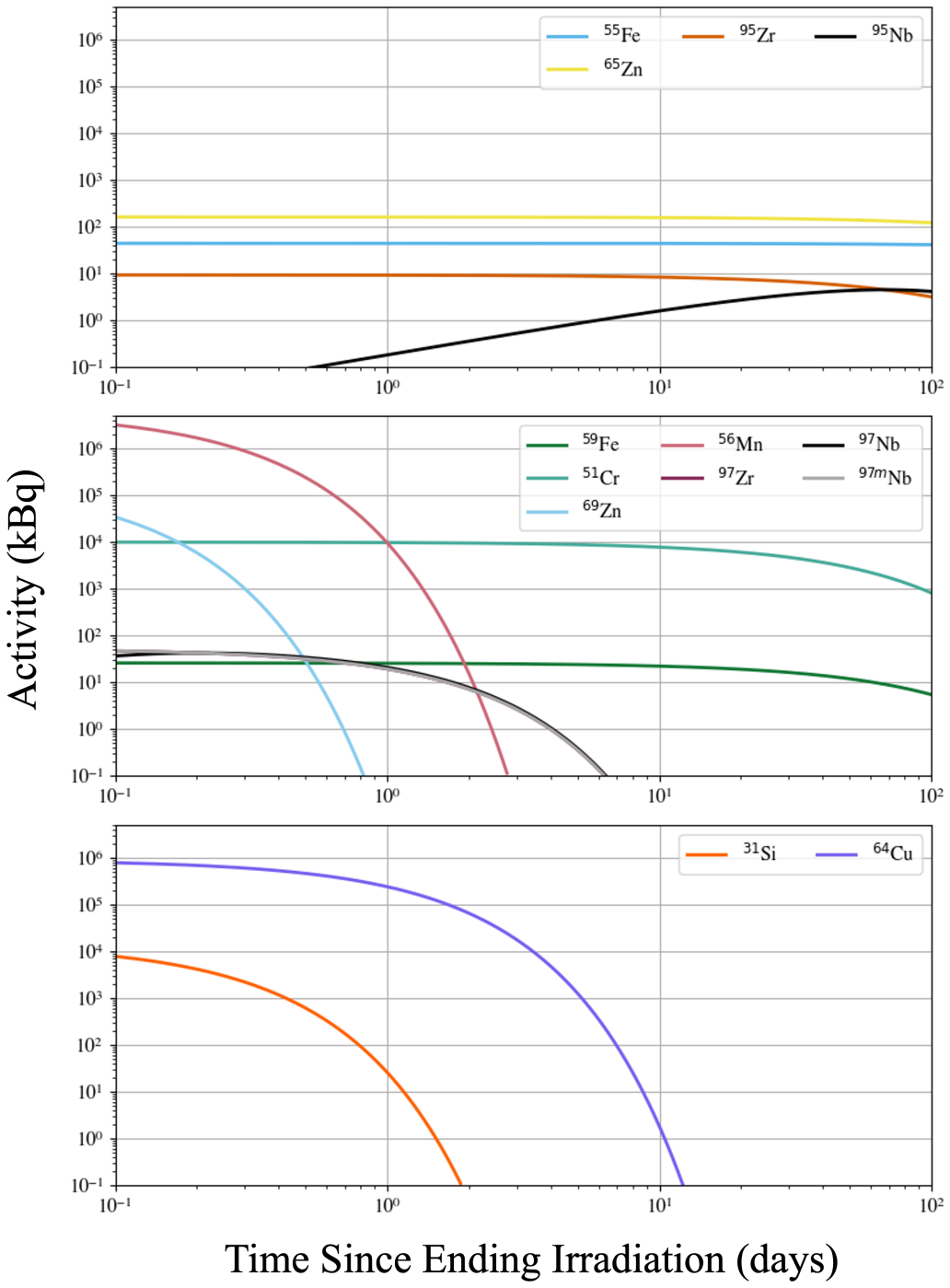

Figure 7.10: The expected activities of the radioisotopes from Al 6061 over a period of 100 days after ending irradiation. In the first plot the production and decay of ^{95}Nb is due to the decay of ^{95}Zr, and in the second plot one can see the production of ^{97m}Nb and then subsequent decay into ^{97}Nb.

```
def calc_decay_chain_for_NC(time, daughter_A, daughter_B, daughter_C,  decay_const, DecayingActivity, N):
    '''
    Calculates the decaying activity of N_C in the decay chain:
                        N_A → N_B → N_C → N_D
    where N_D is stable.

    Parameters:
    time : Time that the radioisotopes are left to decay for. Units in s.
    daughter_A: String. The name of the daughter radioisotope that was produced via thermal neutron capture. N_A in the decay
    chain.
    daughter_B: String. The name of the daughter radioisotope that is produced from the decay of daughter_A. N_B in the decay
    chain.
    daughter_C: String. The name of the daughter radioisotope that is produced from the decay of daughter_B. N_C in the decay chain.
    decay_const : Dictionary of the decay constants for the  radioisotopes. Units in s-1.
    DecayingActivity : Dictionary that contains the decaying activities for all of the isotopes. Units in kBq.
    N : Dictionary that contains the number of atoms for all of the isotopes during the irradiation period.

    Returns:
    DecayingActivity : Dictionary. Contains the decaying activities for all of the isotopes, newly filled for the daughter_C
    isotope. Units in kBq.

    '''
    DecayingActivity[daughter_C] = [] #Creates an empty array in the DecayingActivity dictionary for daughter_C
    lam_A = decay_const[daughter_A] # Decay constant of daughter_A
    lam_B = decay_const[daughter_B] # Decay constant of daughter_B
    lam_C = decay_const[daughter_C] # Decay constant of daughter_C

    c_1 = lam_A*lam_B*N[daughter_A][-1]/((lam_B – lam_A)*(lam_C – lam_A)) # Coefficient 1 for the Bateman equation where n=3
    c_2 = lam_A*lam_B*N[daughter_A][-1]/((lam_A - lam_B)*(lam_C - lam_B)) # Coefficient 2 for the Bateman equation where n=3
    for i in range(len(time)):
        a = (c_1*np.e**(-lam_A*time[i]) + c_2*np.e**(-lam_B*time[i]) - ((c_1 + c_2)*np.e**(-lam_C*time[i])))* lam_C
        # Calculates the activity of  daughter_C using the Bateman equation for n=3
        DecayingActivity[daughter_C].append(a/1000) # Converts the activity to kBq and adds it to the dictionary array


    return DecayingActivity
```

Figure 7.11: Python pseudocode to calculate the activity of the isotope N_C for the decay chain $N_A \xrightarrow{\lambda_A} N_B \xrightarrow{\lambda_B} N_C \xrightarrow{\lambda_C} N_D$ where N_D is stable. The activity was calculated by multiplying the Bateman equation for the case where n=3 (Equation 6.16) by λ_C.

Table 7.6: Al 6061 radioisotope activities immediately after ending irradiation and for 10/50/100 days after ending irradiation. Activities less than 10^{-6} kBq are denoted as $\sim$. Radioisotopes that are only present once their parent radioisotope begins to decay are symbolized by —-.

	Activity after ending irradiation (kBq)	**Activity after ending irradiation for:** 10 days (kBq)	50 days (kBq)	100 days (kBq)
^{28}Al	2.68x10^{8}	$\sim$	$\sim$	$\sim$
^{27}Mg	6.13x10^{4}	$\sim$	$\sim$	$\sim$
^{31}Si	1.48x10^{4}	$\sim$	$\sim$	$\sim$
^{55}Fe	44.06	43.76	42.56	41.11
^{59}Fe	25.70	21.99	11.79	5.41
^{64}Cu	8.91x10^{5}	1.82	$\sim$	$\sim$
^{66}Cu	1.30x10^{6}	$\sim$	$\sim$	$\sim$
^{51}Cr	9.90x10^{3}	7.71x10^{3}	2.83x10^{3}	8.11x10^{2}
^{55}Cr	4.58x10^{4}	$\sim$	$\sim$	$\sim$
^{65}Zn	1.61x10^{2}	1.56x10^{2}	1.39x10^{2}	1.21x10^{2}
^{69}Zn	2.01x10^{5}	$\sim$	$\sim$	$\sim$
^{71}Zn	6.23x10^{2}	$\sim$	$\sim$	$\sim$
^{51}Ti	8.85x10^{3}	$\sim$	$\sim$	$\sim$
^{56}Mn	6.08x10^{6}	$\sim$	$\sim$	$\sim$
^{93}Zr	4.85x10^{-6}	4.85x10^{-6}	4.85x10^{-6}	4.85x10^{-6}
^{95}Zr	9.29	8.34	5.41	3.15
^{97}Zr	51.61	2.49x10^{-3}	$\sim$	$\sim$
^{93m}Nb	_____	$\sim$	$\sim$	$\sim$
^{95}Nb	_____	1.58	4.32	4.11
^{97}Nb	_____	2.69x10^{-3}	$\sim$	$\sim$
^{97m}Nb	_____	2.50x10^{-3}	$\sim$	$\sim$

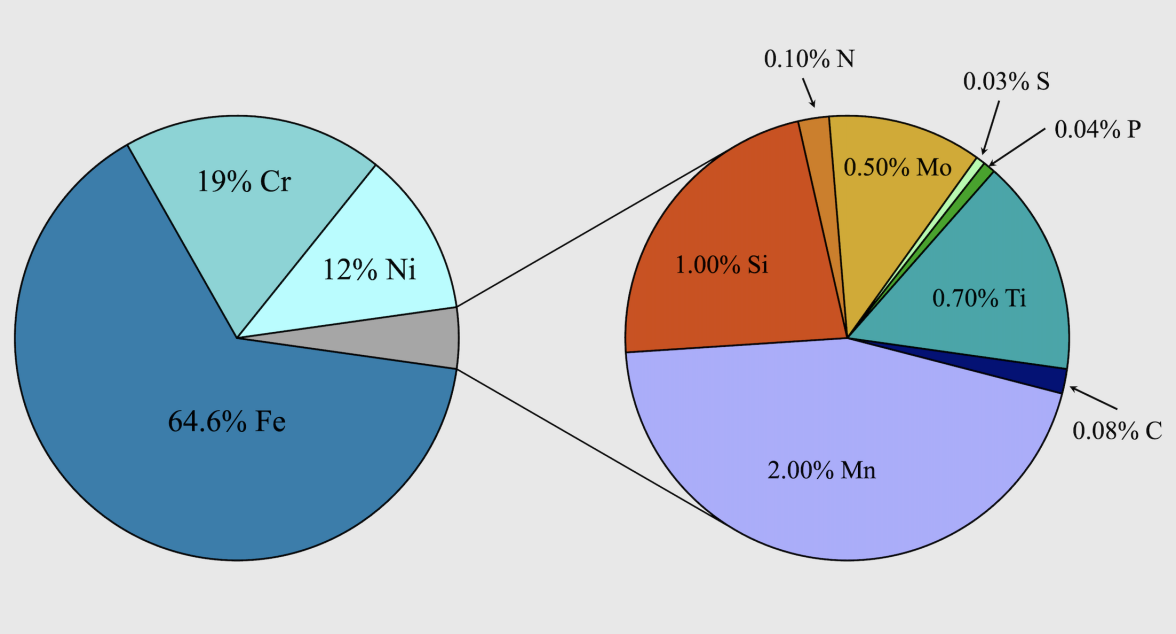

Figure 7.12: The elemental composition of stainless steel (SS) 321. The maximum elemental percentages were used to account for deviations in the SS 321 composition. Elemental percentages sourced from [104].

Table 7.6 shows the activities for the radioisotopes present immediately after ceasing irradiation and for 10, 50, and 100 days afterwards. Like Table 7.3, activities less than 10^{-6} kBq are denoted as "$\sim$" while radioisotopes that are only present once their parent radioisotope begins to decay are symbolized by "—-".

As can be seen in these Figures and the Table, seven of these radioisotopes still have an activity greater than 10^{-6} kBq after 100 days, with two of them, ^{51}Cr and ^{65}Zn, having activities of 0.8 MBq and 0.1 MBq, respectively. However, this is still less than what would be expected if the canister was made of stainless steel which has a higher content of Cr.

7.4.2 Activity of Stainless Steel 321

If the canister was made of stainless steel (SS) 321, we would expect the resulting canister to be more radioactive than the Al 6061 after irradiation. Shown in Figure 7.12, SS 321 contains more Fe than that of Al 6061 as well as more Cr, both of which become activated in a neutron flux.

Table 7.7: Properties of isotopes present within Stainless Steel (SS) 321 that produce radioisotopes when subject to a thermal neutron flux. Isotope fractions and cross-sections sourced from the ENDF [101] and Nubase [100] online libraries. Elemental fractions sourced from [104].

	Elemental fraction of SS 321 (by weight)	**Isotope fraction**	**Thermal neutron capture cross-section (barns)**
^{54}Fe	0.6455	0.0585	2.253
^{58}Fe	0.6455	0.0028	1.315
^{15}N	0.001	0.004	15.000
^{62}Ni	0.12	0.03635	14.999
^{64}Ni	0.12	0.00926	1.490
^{92}Mo	0.005	0.1465	0.0799
^{98}Mo	0.005	0.2429	0.130
^{100}Mo	0.005	0.0974	0.200
^{50}Cr	0.19	0.0434	15.362
^{54}Cr	0.19	0.0237	0.414
^{34}S	0.0003	0.0425	0.224
^{36}S	0.0003	0.0001	0.151
^{30}Si	0.008	0.031	0.108
^{31}P	0.0004	1	0.170
^{55}Mn	0.02	1	13.276
^{50}Ti	0.007	0.0518	0.181
^{13}C	0.0008	0.011	0.002

Similarly for Al 6061, Tables 7.7 and 7.8 show the different properties for the isotopes that produce radioactive isotopes as well as the properties for the produced radioisotopes and their decay chains.

Table 7.8: Radioisotopes produced from the thermal neutron capture of isotopes within SS 321. Half-lives and decay chains were sourced from the ENSDF [16] online database. EC and IT refer to electron capture and internal transition, respectively.

Radioisotope	Half-life	Decay chain
^{55}Fe	2.7 yrs.	$^{55}\underset{\text{EC(2.7 y)}}{\text{Fe}} \longrightarrow {}^{55}\underset{\text{(Stable)}}{\text{Mn}}$
^{59}Fe	44.5 days	$^{59}\underset{\beta^-\text{(44.5 d)}}{\text{Fe}} \longrightarrow {}^{59}\underset{\text{(Stable)}}{\text{Co}}$
^{16}N	7.1 s	$^{16}\underset{\beta^-\text{(7.1 s)}}{\text{N}} \longrightarrow {}^{16}\underset{\text{(Stable)}}{\text{O}}$
^{63}Ni	100.1 yrs.	$^{63}\underset{\beta^-\text{(100 y)}}{\text{Ni}} \longrightarrow {}^{63}\underset{\text{(Stable)}}{\text{Cu}}$
^{65}Ni	2.5 hrs.	$^{65}\underset{\beta^-\text{(2.5 h)}}{\text{Ni}} \longrightarrow {}^{65}\underset{\text{(Stable)}}{\text{Cu}}$
^{93}Mo	4.8x10^3 yrs.	$^{93}\underset{\text{EC}(4.8\times10^3\text{ y})}{\text{Mo}} \longrightarrow {}^{93}\underset{\text{(Stable)}}{\text{Nb}}$
^{99}Mo	2.7 days	$^{99}\underset{\beta^-\text{(2.7 d)}}{\text{Mo}} \longrightarrow {}^{99m}\underset{\text{IT(6 h)}}{\text{Tc}} \longrightarrow {}^{99}\underset{\beta^-(2x10^5y)}{\text{Tc}} \longrightarrow {}^{99}\underset{\text{(Stable)}}{\text{Ru}}$
^{101}Mo	14.6 mins.	$^{101}\underset{\beta^-\text{(14.6 m)}}{\text{Mo}} \longrightarrow {}^{101}\underset{\beta^-\text{(14 m)}}{\text{Tc}} \longrightarrow {}^{101}\underset{\text{(Stable)}}{\text{Ru}}$
^{51}Cr	27.7 days	$^{51}\underset{\text{EC(27.7 d)}}{\text{Cr}} \longrightarrow {}^{51}\underset{\text{(Stable)}}{\text{V}}$
^{55}Cr	3.5 mins.	$^{55}\underset{\beta^-\text{(3.5 m)}}{\text{Cr}} \longrightarrow {}^{55}\underset{\text{(Stable)}}{\text{Mn}}$
^{35}S	87.4 days	$^{35}\underset{\beta^-\text{(87.4 d)}}{\text{S}} \longrightarrow {}^{35}\underset{\text{(Stable)}}{\text{Cl}}$
^{37}S	5.1 mins.	$^{37}\underset{\beta^-\text{(5.1 m)}}{\text{S}} \longrightarrow {}^{37}\underset{\text{(Stable)}}{\text{Cl}}$
^{32}P	14.3 days	$^{32}\underset{\beta^-\text{(14.3 d)}}{\text{P}} \longrightarrow {}^{32}\underset{\text{(Stable)}}{\text{P}}$
^{31}Si	2.6 hrs.	$^{31}\underset{\beta^-\text{(2.6 h)}}{\text{Si}} \longrightarrow {}^{31}\underset{\text{(Stable)}}{\text{P}}$
^{56}Mn	2.6 hrs.	$^{56}\underset{\beta^-\text{(2.6 h)}}{\text{Mn}} \longrightarrow {}^{56}\underset{\text{(Stable)}}{\text{Fe}}$
^{14}C	5.7x10^3 yrs.	$^{14}\underset{\beta^-(5.7\times10^3\text{ y})}{\text{C}} \longrightarrow {}^{14}\underset{\text{(Stable)}}{\text{N}}$
^{51}Ti	5.8 mins.	$^{51}\underset{\beta^-\text{(5.8 m)}}{\text{Ti}} \longrightarrow {}^{51}\underset{\text{(Stable)}}{\text{V}}$

In a method similar to that for calculating the activity of the Al 6061 canister, we repeated the same calculations for a canister made of SS 321. Doing so resulted in Figures 7.13 and 7.14, which show the expected radioisotope activity as a function of irradiation time as well as the activities of the radioisotopes 100 days after ending irradiation.

Similar to before, the decays of both ^{99}Mo and ^{101}Mo decay further to ^{99m}Tc and ^{101}Tc, respectively. It should be noted that while ^{99m}Tc does decay to ^{99}Tc, due to the large half-life of ^{99}Tc the resulting activity after 100 days is $\mathcal{O}(10\,\mathrm{mBq})$, which compared to the other activities, meant that it could not be plotted alongside them.

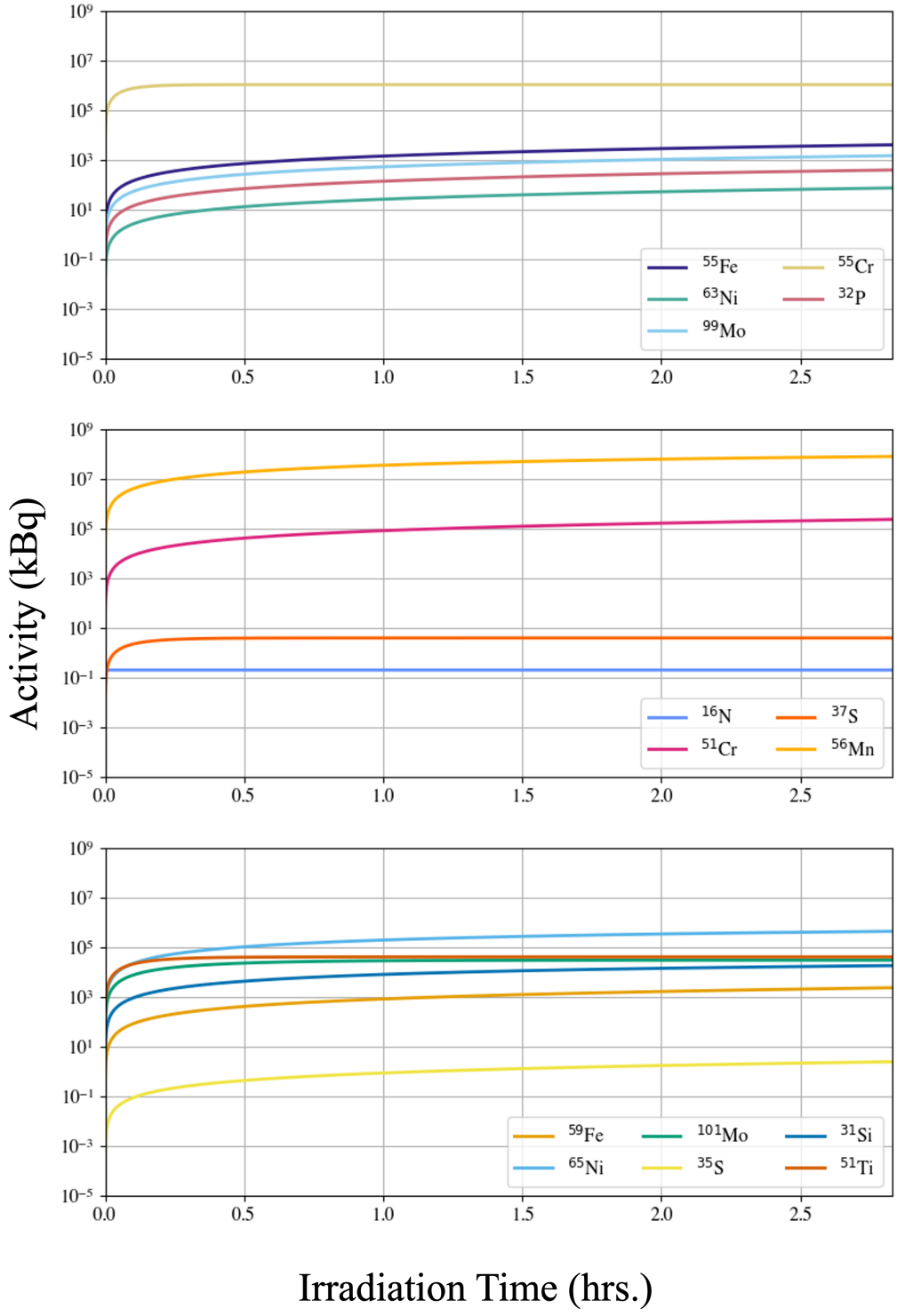

Figure 7.13: The expected activities of the radioisotopes from SS 321 as a function of irradiation time.

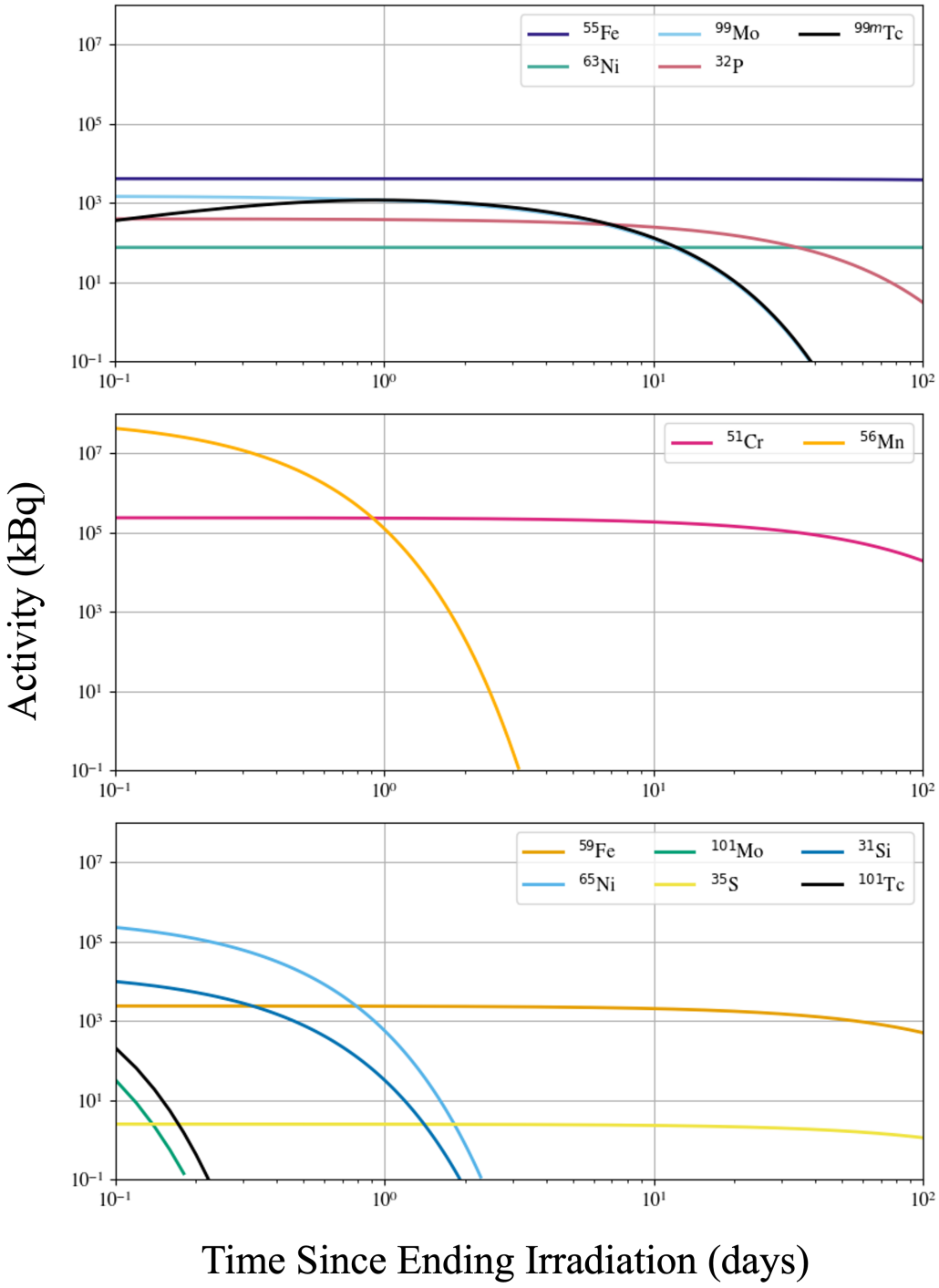

Figure 7.14: The expected activities of the radioisotopes from SS 321 over a period of 100 days after ending irradiation. One can see the production and subsequent decays of ^{99m}Tc as well as ^{101}Tc; however, the activity of ^{99}Tc could not be plotted as it was so small due to its large half-life.

Table 7.9: SS 321 radioisotope activities immediately following irradiation exposure and for 10/50/100 days after exposure had ended. Activities less than 10^{-6} kBq are denoted as $\sim$. Radioisotopes that are only present once their parent begins to decay are symbolized by —-.

	Activity after ending irradiation (kBq)	**Activity after ending irradiation for:** 10 days (kBq)	50 days (kBq)	100 days (kBq)
^{55}Fe	4.07x10^{3}	4.05x10^{3}	3.93x10^{3}	3.80x10^{3}
^{59}Fe	2.36x10^{3}	2.02x10^{3}	1.09x10^{3}	4.99x10^{2}
^{16}N	0.20	$\sim$	$\sim$	$\sim$
^{63}Ni	74.48	74.46	74.41	74.34
^{65}Ni	4.43x10^{5}	$\sim$	$\sim$	$\sim$
^{93}Mo	1.55x10^{-3}	1.55x10^{-3}	1.55x10^{-3}	1.55x10^{-3}
^{99}Mo	1.49x10^{3}	1.19x10^{2}	4.94x10^{-3}	$\sim$
^{101}Mo	3.07x10^{4}	$\sim$	$\sim$	$\sim$
^{51}Cr	2.35x10^{5}	1.83x10^{5}	6.74x10^{4}	1.93x10^{4}
^{55}Cr	1.09x10^{6}	$\sim$	$\sim$	$\sim$
^{35}S	2.47	2.28	1.66	1.12
^{37}S	3.97	$\sim$	$\sim$	$\sim$
^{32}P	3.95x10^{2}	2.43x10^{2}	34.90	3.08
^{31}Si	1.84x10^{4}	$\sim$	$\sim$	$\sim$
^{56}Mn	8.10x10^{7}	$\sim$	$\sim$	$\sim$
^{51}Ti	4.13x10^{4}	$\sim$	$\sim$	$\sim$
^{14}C	1.25x10^{-6}	1.25x10^{-6}	1.25x10^{-6}	1.25x10^{-6}
^{99}Tc	———	4.84x10^{-5}	5.31x10^{-5}	5.31x10^{-5}
^{99m}Tc	———	1.31x10^{2}	5.43x10^{-3}	$\sim$
^{101}Tc	———	$\sim$	$\sim$	$\sim$

Looking at Table 7.9, nine of the radioisotopes are still radioactive after the 100 day rest period. ^{93}Mo, ^{14}C, and ^{99}Tc have rather low activities of 1.6 Bq, 1.3 mBq, and 53.1 mBq, respectively. However, of the remaining radioisotopes ^{55}Fe, ^{59}Fe, ^{63}Ni, and ^{51}Cr have activities of 3.8 MBq, 0.5 MBq, 74.3 kBq, and 19.3 MBq, respectively.

Comparing the outcomes in Table 7.6 and Table 7.9, it is evident that Al 6061 will become less radioactive than SS 321 once irradiated with a thermal neutron source. However, care will need to be taken as even the Al 6061 canister will still be radioactive once removed from RMC's reactor pool.

7.5 Proposed Safety Measures and Calibration Source Deployment Method

Prior to the production of the ^{127}Xe calibration source, we plan to be in contact with the Environmental Health and Safety (EHS) unit at McGill as well as McGill's Radiation Safety Officer (RSO) in order to ensure that they are aware of and approve of us using such a radioactive source. As per McGill's Radiation Safety Manual [105], the lab space will have to be subject to safety inspections to ensure that it meets the requirements to house such a radioactive source, and that the LoLX gas handling system (described later in this Section) has been leak tested. In addition to this, all personnel who will be working on the experiment will need to have participated in and passed McGill's Radiation Safety Training.

Presently, all exhaust lines from vacuum pumps in the lab space are connected to the fume hood exhaust. Therefore, if a leak were to occur, any gas leaking through these paths would be evacuated from the lab through the fume hood exhaust. However, in order to ensure the safety of those working in the lab, as outlined in [105], all persons in the lab would have to be evacuated, the doors firmly shut with signs indicating that they should not be opened, and the RSO as well as the McGill Security Services should be contacted immediately.

In addition to this, we plan to take further precautions by ensuring that neither the source nor the canister are dangerous to humans by measuring the resulting radioactivities of the xenon gas and canister.

To do this, we plan to order a second copy of the aluminum canister. This canister can then be used, along with a low-background HPGe detector, to establish a background rate. Once the 100 days after irradiation has passed, we can transfer the irradiated xenon gas from the first canister to the second. We can then use a HPGe detector, along with our knowledge of the canister's background rate, to establish which radionuclides are present and how radioactive they are.

Furthermore, equipment at RMC can be used to ensure that neither the source nor the canister pose any danger to humans.

Once the source is brought to McGill, we plan to inject the calibration source through the LoLX gas handling system in order to filter out any impurities. As shown in Figure 7.15, the LoLX gas handling system features a PS3-MT3-R-1 MonoTorr heated purifier that is specified for the purification of He, Ar, and Xe gases. In prior work by Lenardo et al. [64], they found that by transferring the gas from the canister that it was irradiated in into a new canister the number of Cs atoms had decreased. Their hypothesis was that the Cs atoms had adhered to the sides of the canister walls. As well, they found that after purifying the xenon gas they did not find any other unexpected isotopes present in the gas [64].

The current proposed method for deploying the calibration source in LoLX is to first route the gas through the MonoTorr purifier, and then to inject the entirety of the gas into LoLX. Prior work by Lenardo et al. incrementally injected small amounts of the calibration gas into their experimental setup in order to maintain a steady level of calibration activity. However, if the initial activity of the calibration source is known prior to deployment, it is simple enough to calculate the activity over time and adjust one's calibration accordingly. This will allow for the calibration source to be used for multiple data-taking runs as even after three months the source will only decay to an activity of ~ 220 Bq.

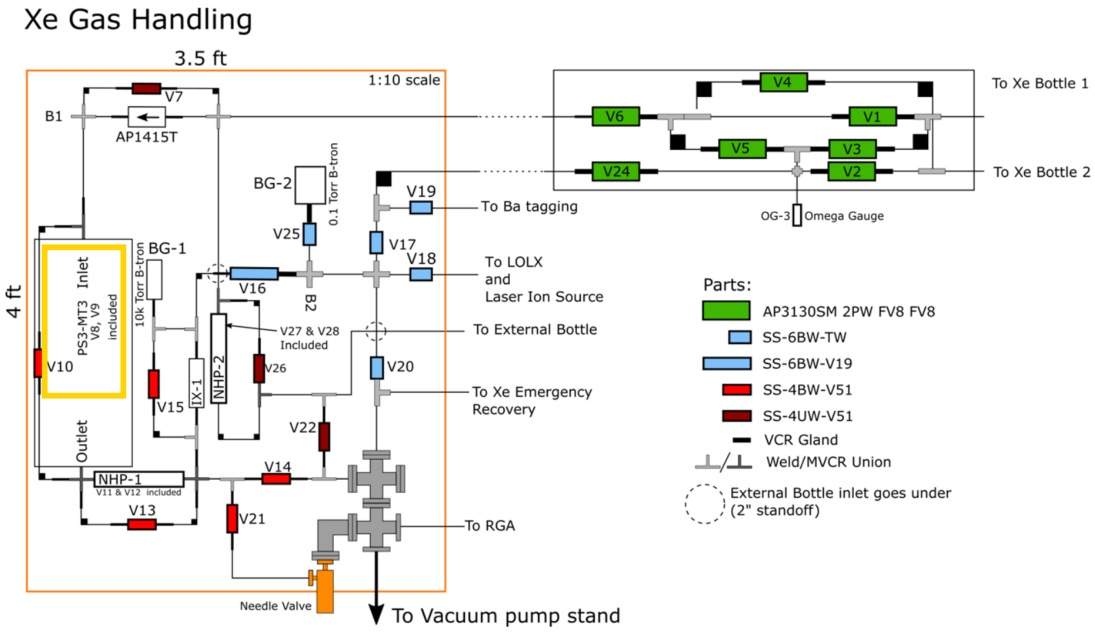

Figure 7.15: The Layout of the Xe gas handling system. The location of the PS3-MT3-R-1 MonoTorr heated purifier, which is designed for the purification of He, Ar, and Xe gases, is highlighted by the yellow rectangle. Original image created by Xiao Shang.

Chapter 8

Conclusion

The LoLX detector is currently being used to monitor and characterize the long-term behaviour of Hamamatsu VUV4 and FBK VUV-HD3 SiPMs for the nEXO experiment. In order to study them, we intend to use radioactive ^{127}Xe to act as an *in situ* calibration source for the detector.

This thesis covered the theoretical underpinnings for such a source, extending from the theory of radioisotope production due to neutron activation, the source canister design, proposed implementation of the calibration source into the detector, as well as the expected radioisotopes and their activities. This work showed that in order to achieve an ^{127}Xe activity of 1.5 kBq at the time of deployment, one must irradiate 16.5 g of ^{nat}Xe for 2.8 hours and then let the canister rest for upwards of 100 days. This work further showed that while Al 6061 is a better material to use than SS 321, it should still be handled with care as it too will be radioactive following irradiation.

Appendix A

A.1 Canister Components

The CAD drawings for the canister components that show the bill of materials (BOM), the part numbers, the part dimensions, and weld/surface finish instructions for the machine shop. All of the measurements are shown in inches.

ITEM NO.	PART NUMBER	DESCRIPTION	QTY.
1	9056K55	Multipurpose 6061 Aluminum Round Tube	1

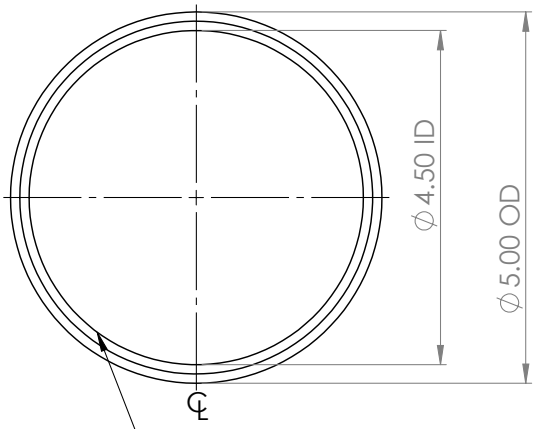

Machine inner surface for smooth surface

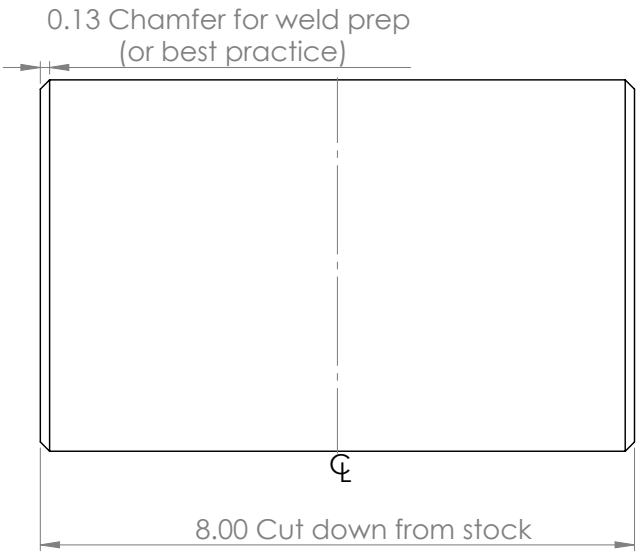

McMaster Carr part SKU #9056K55

		UNLESS OTHERWISE SPECIFIED:		NAME	DATE
		DIMENSIONS ARE IN INCHES TOLERANCES: FRACTIONAL ± ANGULAR: MACH ± BEND ± TWO PLACE DECIMAL ± THREE PLACE DECIMAL ±	DRAWN		
			CHECKED		
			ENG APPR.		
			MFG APPR.		
		INTERPRET GEOMETRIC TOLERANCING PER:	Q.A.		
		MATERIAL 6061 Aluminum	COMMENTS:		
NEXT ASSY	USED ON	FINISH			
APPLICATION		DO NOT SCALE DRAWING			

TITLE:
XAC001_CanisterBody_MC_9056K55

SIZE	DWG. NO.	REV
A	XAC001	

SCALE: 1:2	WEIGHT:	SHEET 1 OF 11

ITEM NO.	PART NUMBER	DESCRIPTION	QTY.
1	1610T143	Multipurpose 6061 Aluminum	1

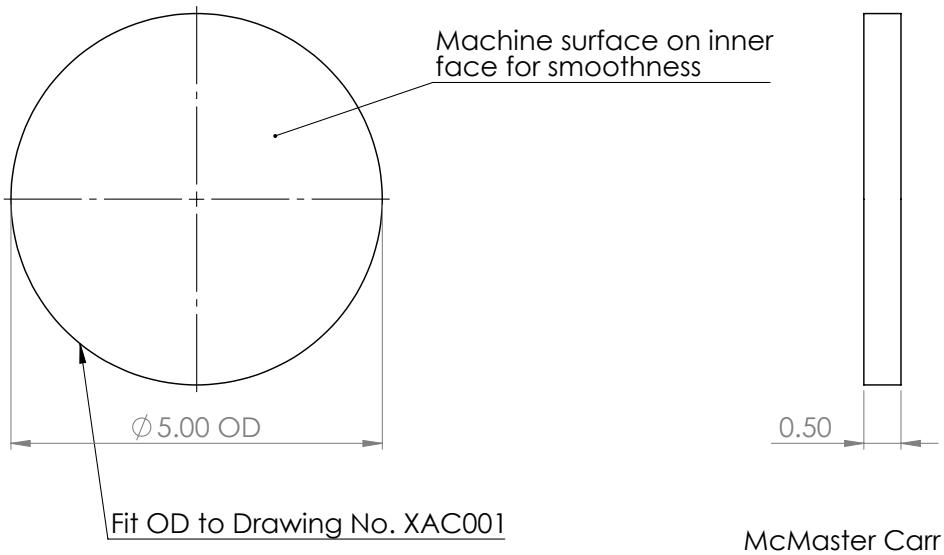

McMaster Carr part SKU #1610T48-1610T143

NEXT ASSY	USED ON	
APPLICATION		

UNLESS OTHERWISE SPECIFIED:

DIMENSIONS ARE IN INCHES
TOLERANCES:
FRACTIONAL ±
ANGULAR: MACH ± BEND ±
TWO PLACE DECIMAL ±
THREE PLACE DECIMAL ±

INTERPRET GEOMETRIC TOLERANCING PER:

MATERIAL
6061 Aluminum

FINISH

DO NOT SCALE DRAWING

	NAME	DATE
DRAWN		
CHECKED		
ENG APPR.		
MFG APPR.		
Q.A.		

COMMENTS:

TITLE:
XAC002_CanisterBottom_MC_1610T48

SIZE	DWG. NO.	REV
A	XAC002	

SCALE: 1:2	WEIGHT:	SHEET 2 OF 11

ITEM NO.	PART NUMBER	DESCRIPTION	QTY.
1	1610T143	Multipurpose 6061 Aluminum	1

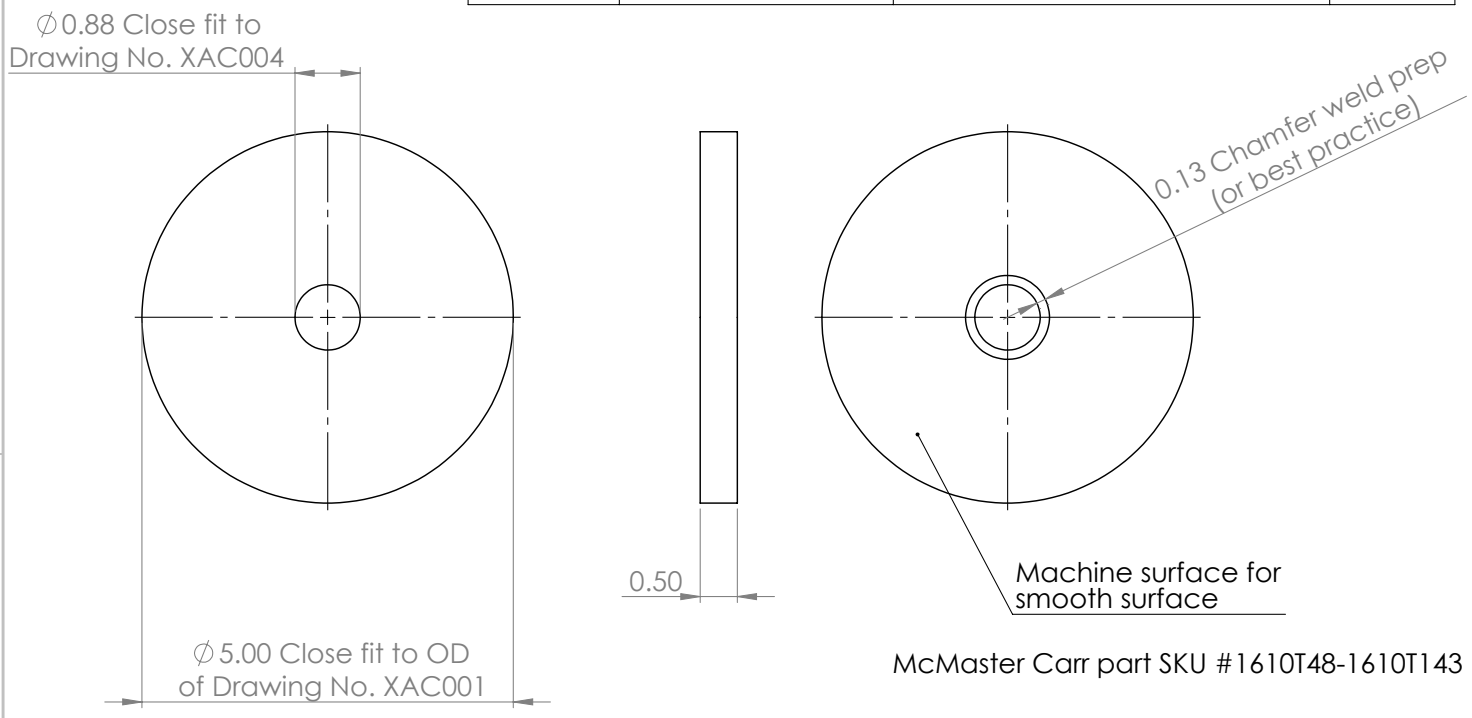

McMaster Carr part SKU #1610T48-1610T143

		UNLESS OTHERWISE SPECIFIED:		NAME	DATE
		DIMENSIONS ARE IN INCHES TOLERANCES: FRACTIONAL ± ANGULAR: MACH ± BEND ± TWO PLACE DECIMAL ± 0.010 THREE PLACE DECIMAL ± 0.005	DRAWN		
			CHECKED		
			ENG APPR.		
			MFG APPR.		
		INTERPRET GEOMETRIC TOLERANCING PER:	Q.A.		
		MATERIAL 6061 Aluminum	COMMENTS:		
NEXT ASSY	USED ON	FINISH			
APPLICATION		DO NOT SCALE DRAWING			

TITLE:
XAC003_CanisterTop_MC_1610T48

SIZE	DWG. NO.	REV
A	XAC003	

SCALE: 1:2	WEIGHT:	SHEET 3 OF 11

ITEM NO.	PART NUMBER	DESCRIPTION	QTY.
1	5038K544	Standard-Wall Aluminum Pipe	1

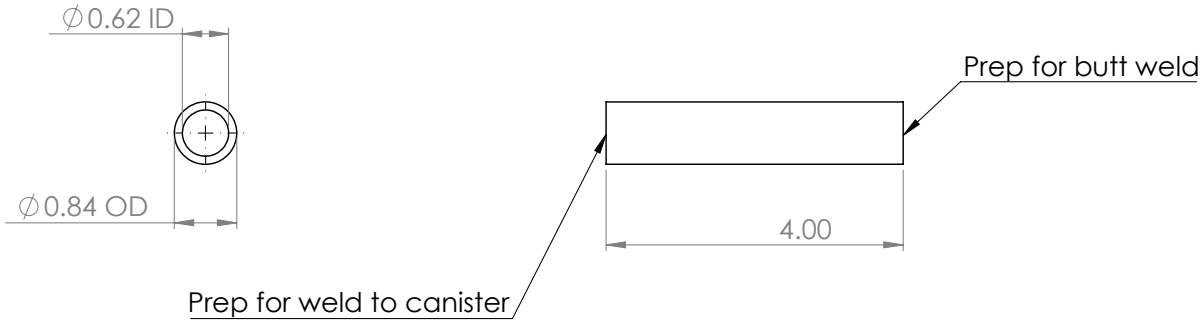

McMaster Carr part SKU #5038K544

		UNLESS OTHERWISE SPECIFIED:		NAME	DATE
		DIMENSIONS ARE IN INCHES TOLERANCES: FRACTIONAL ± ANGULAR: MACH ± BEND ± TWO PLACE DECIMAL ± THREE PLACE DECIMAL ±	DRAWN		
			CHECKED		
			ENG APPR.		
			MFG APPR.		
		INTERPRET GEOMETRIC TOLERANCING PER:	Q.A.		
		MATERIAL 6061 Aluminum	COMMENTS:		
NEXT ASSY	USED ON	FINISH			
APPLICATION		DO NOT SCALE DRAWING			

TITLE: XAC004_Pipe_MC_5038K544

SIZE	DWG. NO.	REV
A	XAC004	

SCALE: 1:2	WEIGHT:	SHEET 4 OF 11

ITEM NO.	PART NUMBER	DESCRIPTION	QTY.
1	43485K119	Standard-Wall Butt-Weld Aluminum Unthreaded Pipe Fitting	2

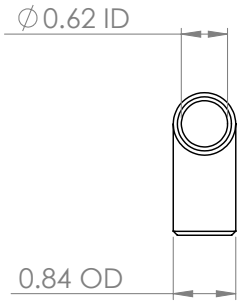

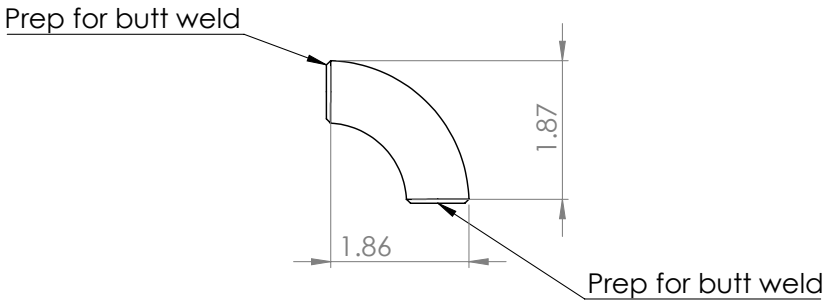

McMaster Carr part SKU #43485K119

NEXT ASSY	USED ON	
APPLICATION		

UNLESS OTHERWISE SPECIFIED:

DIMENSIONS ARE IN INCHES
TOLERANCES:
FRACTIONAL ±
ANGULAR: MACH ± BEND ±
TWO PLACE DECIMAL ±
THREE PLACE DECIMAL ±

INTERPRET GEOMETRIC TOLERANCING PER:

MATERIAL
6061 Aluminum

FINISH

DO NOT SCALE DRAWING

	NAME	DATE
DRAWN		
CHECKED		
ENG APPR.		
MFG APPR.		
Q.A.		

COMMENTS:

TITLE:
XAC005_Elbow_MC_43485K119

SIZE	DWG. NO.	REV
A	XAC005	

SCALE: 1:2 | WEIGHT: | SHEET 5 OF 11

ITEM NO.	PART NUMBER	DESCRIPTION	QTY.
1	5038K546	Standard-Wall Aluminum Pipe	1

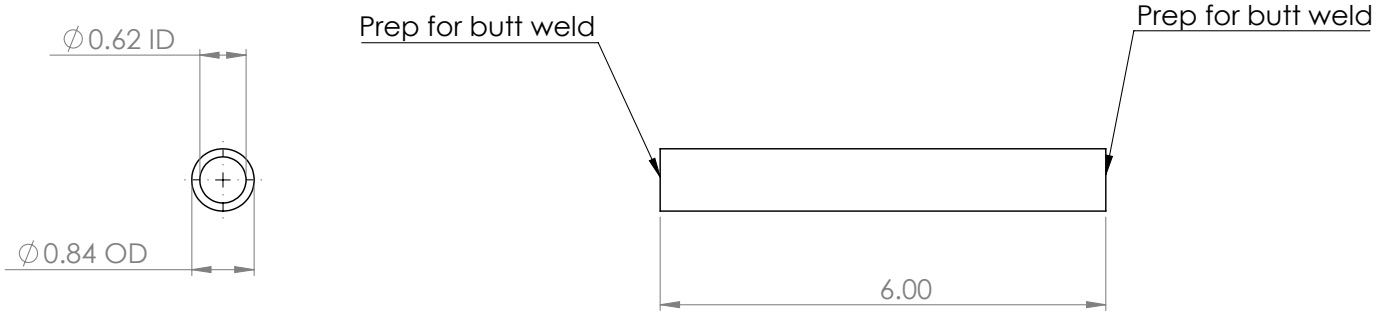

McMaster Carr part SKU #5038K546

		UNLESS OTHERWISE SPECIFIED:		NAME	DATE
		DIMENSIONS ARE IN INCHES TOLERANCES: FRACTIONAL ± ANGULAR: MACH ± BEND ± TWO PLACE DECIMAL ± THREE PLACE DECIMAL ±	DRAWN		
			CHECKED		
			ENG APPR.		
			MFG APPR.		
		INTERPRET GEOMETRIC TOLERANCING PER:	Q.A.		
		MATERIAL 6061 Aluminum	COMMENTS:		
NEXT ASSY	USED ON	FINISH			
APPLICATION		DO NOT SCALE DRAWING			

TITLE: XAC006_Pipe_MC_5038K546

SIZE	DWG. NO.	REV
A	XAC006	

SCALE: 1:2	WEIGHT:	SHEET 6 OF 11

ITEM NO.	PART NUMBER	DESCRIPTION	QTY.
1	5038K54	Standard-Wall Aluminum Pipe	1

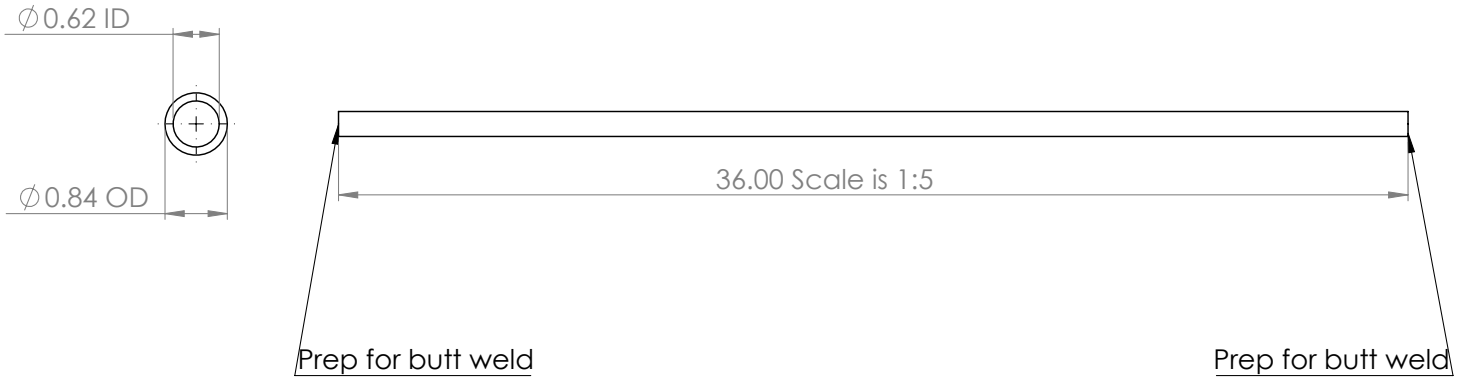

McMaster Carr part SKU #5038K54

		UNLESS OTHERWISE SPECIFIED:		NAME	DATE
		DIMENSIONS ARE IN INCHES TOLERANCES: FRACTIONAL ± ANGULAR: MACH ± BEND ± TWO PLACE DECIMAL ± THREE PLACE DECIMAL ±	DRAWN		
			CHECKED		
			ENG APPR.		
			MFG APPR.		
		INTERPRET GEOMETRIC TOLERANCING PER:	Q.A.		
		MATERIAL 6061 Aluminum	COMMENTS:		
NEXT ASSY	USED ON	FINISH			
APPLICATION		DO NOT SCALE DRAWING			

TITLE: XAC007_Pipe_MC_5038K54

SIZE	DWG. NO.	REV
A	XAC007	

SCALE: 1:2	WEIGHT:	SHEET 7 OF 11

ITEM NO.	PART NUMBER	DESCRIPTION	QTY.
1	NA	Swagelok Stainless Steel Tubing	1

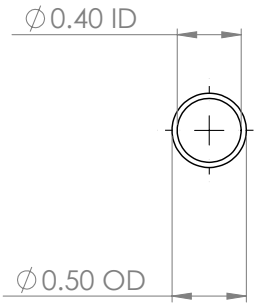

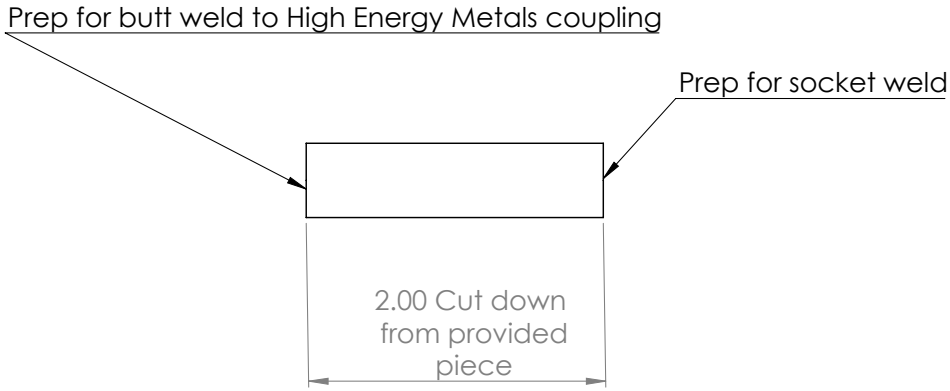

Piece will be provided

		UNLESS OTHERWISE SPECIFIED:		NAME	DATE	
		DIMENSIONS ARE IN INCHES TOLERANCES: FRACTIONAL ± ANGULAR: MACH ± BEND ± TWO PLACE DECIMAL ± THREE PLACE DECIMAL ±	DRAWN			
			CHECKED			TITLE: XAC008_Swagelok_SSTube
			ENG APPR.			
			MFG APPR.			
		INTERPRET GEOMETRIC TOLERANCING PER:	Q.A.			
		MATERIAL 316 Stainless Steel	COMMENTS:			SIZE A / DWG. NO. XAC008 / REV
NEXT ASSY	USED ON	FINISH				
APPLICATION		DO NOT SCALE DRAWING				SCALE: 1:1 / WEIGHT: / SHEET 8 OF 11

ITEM NO.	PART NUMBER	DESCRIPTION	QTY.
1	NA	Explosion bonded coupler	1

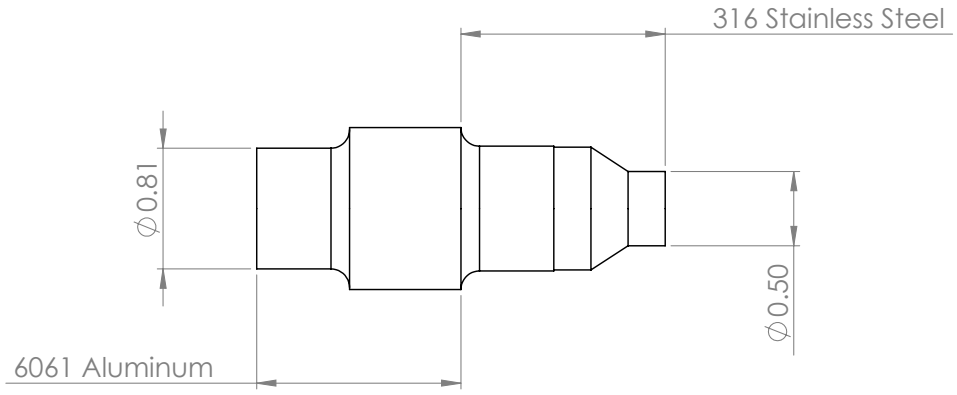

Stand-in for High Energy Metals coupler - actual part will be provided and may vary

		UNLESS OTHERWISE SPECIFIED:		NAME	DATE
		DIMENSIONS ARE IN INCHES TOLERANCES: FRACTIONAL ± ANGULAR: MACH ± BEND ± TWO PLACE DECIMAL ± THREE PLACE DECIMAL ±	DRAWN		
			CHECKED		
			ENG APPR.		
			MFG APPR.		
		INTERPRET GEOMETRIC TOLERANCING PER:	Q.A.		
		MATERIAL 316 Stainless Steel 6061 Aluminum	COMMENTS:		
NEXT ASSY	USED ON	FINISH			
APPLICATION		DO NOT SCALE DRAWING			

TITLE: XAC009_ExplosionBondedCoupler

SIZE	DWG. NO.	REV
A	XAC009	

SCALE: 1:1 | WEIGHT: | SHEET 9 OF 11

ITEM NO.	PART NUMBER	DESCRIPTION	QTY.
1	SS-8-VCR-3-8MTW	Swagelok Gland	1

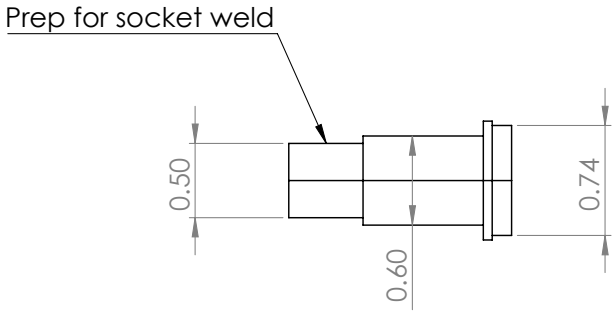

For reference only - actual part will be provided

Swagelok part #SS-8-VCR-3-8MTW

NEXT ASSY	USED ON	
APPLICATION		

UNLESS OTHERWISE SPECIFIED:

DIMENSIONS ARE IN INCHES
TOLERANCES:
FRACTIONAL ±
ANGULAR: MACH ± BEND ±
TWO PLACE DECIMAL ±
THREE PLACE DECIMAL ±

INTERPRET GEOMETRIC TOLERANCING PER:

MATERIAL
316 Stainless Steel

FINISH

DO NOT SCALE DRAWING

	NAME	DATE
DRAWN		
CHECKED		
ENG APPR.		
MFG APPR.		
Q.A.		

COMMENTS:

TITLE:
XAC010_Gland_S_SS8VCR38MTW

SIZE	DWG. NO.	REV
A	XAC010	

SCALE: 1:1 | WEIGHT: | SHEET 10 OF 1

ITEM NO.	PART NUMBER	DESCRIPTION	QTY.
1	SS-8-VCR-4	Swagelok Male Nut	1

Swagelok part #SS-8-VCR-4

		UNLESS OTHERWISE SPECIFIED:		NAME	DATE
		DIMENSIONS ARE IN INCHES TOLERANCES: FRACTIONAL ± ANGULAR: MACH ± BEND ± TWO PLACE DECIMAL ± THREE PLACE DECIMAL ±	DRAWN		
			CHECKED		
			ENG APPR.		
			MFG APPR.		
		INTERPRET GEOMETRIC TOLERANCING PER:	Q.A.		
		MATERIAL 316 Stainless Steel	COMMENTS:		
NEXT ASSY	USED ON	FINISH			
APPLICATION		DO NOT SCALE DRAWING			

TITLE: XAC011_NUT_S_SS8VCR4

SIZE	DWG. NO.	REV
A	XAC011	

SCALE: 1:1 | WEIGHT: | SHEET 11 OF 1

A.2 Canister Assembly Instructions

The CAD drawings for the canister assembly instructions that show the BOM, which references the parts in A, as well as the weld/surface finish instructions for the machine shop.

ITEM NO.	Drawing No.	PART NUMBER	DESCRIPTION	QTY.
1	XAC002	1610T143	Multipurpose 6061 Aluminum	1
2	XAC001	9056K55	Multipurpose 6061 Aluminum Round Tube	1
3	XAC003	1610T143	Multipurpose 6061 Aluminum	1
4	XAC004	5038K544	Standard-Wall 6061 Aluminum Pipe	1

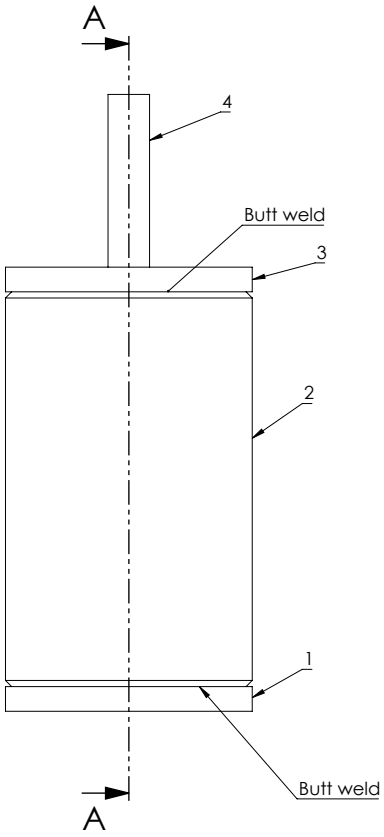

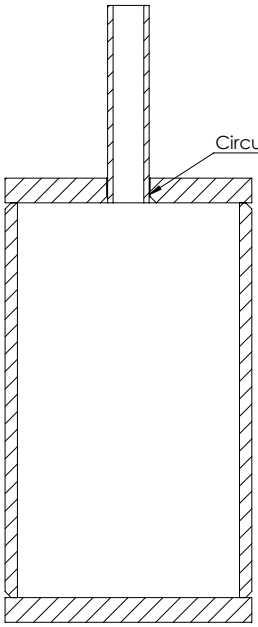

SECTION A-A
SCALE 1 : 2

Clean parts to vacuum standards prior to welding
Welds should be leak-tight for ultra-high vacuum application

UNLESS OTHERWISE SPECIFIED: DIMENSIONS ARE IN MILLIMETERS SURFACE FINISH: TOLERANCES: LINEAR: ANGULAR:	FINISH:		DEBURR AND BREAK SHARP EDGES	DO NOT SCALE DRAWING	REVISION
	NAME	SIGNATURE	DATE	TITLE: Step 1	
DRAWN					
CHK'D					
APPV'D					
MFG					
Q.A					
			MATERIAL:	DWG NO. XAC_Assembly_Step1	A3
			WEIGHT:	SCALE: 1:2	SHEET 1 OF 2

ITEM NO.	DRAWING NO.	PART NUMBER	DESCRIPTION	QTY.
1	XAC002	1610T143	Multipurpose 6061 Aluminum	1
2	XAC001	9056K55	Multipurpose 6061 Aluminum Round Tube	1
3	XAC003	1610T143	Multipurpose 6061 Aluminum	1
4	XAC004	5038K544	Standard-Wall Aluminum Pipe	1
5	XAC006	5038K546	Standard-Wall Aluminum Pipe	1
6	XAC005	43485K119	Standard-Wall Butt-Weld Aluminum Unthreaded Pipe Fitting	2
7	XAC007	5038K54	Standard-Wall Aluminum Pipe	1
9	XAC009	NA	Explosion Bonded Coupler	1
10	XAC008	NA	Swagelok Stainless Steel Tubing	1
11	XAC010	SS-8-VCR-3-8MTW	Swagelok Gland	1
12	XAC011	SS-8-VCR-4	Swagelok Male Nut	1

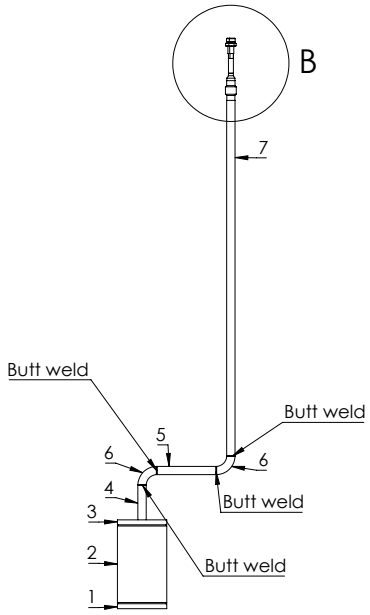

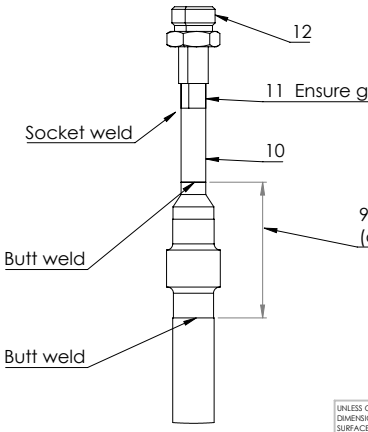

DETAIL B
SCALE 1 : 2

Clean parts to vacuum standards prior to welding
Welds should be leak-tight for ultra-high vacuum application

UNLESS OTHERWISE SPECIFIED: DIMENSIONS ARE IN MILLIMETERS SURFACE FINISH: TOLERANCES: LINEAR: ANGULAR:	FINISH:		DEBURR AND BREAK SHARP EDGES	DO NOT SCALE DRAWING	REVISION
	NAME	SIGNATURE	DATE	TITLE: Step 2	
DRAWN					
CHK'D					
APPV'D					
MFG					
Q.A					
				MATERIAL:	DWG NO. XAC_Assembly_Step2 A3
				WEIGHT:	SCALE: 1:10 SHEET 2 OF 2

A.3 Assembled Canister Design

A CAD drawing which shows the final canister assembly, the overall dimensions, and notes the materials that are used. In the drawing "Aluminum" refers to Aluminum 6061 and "Stainless steel" refers to Stainless Steel 321. All of the measurements are shown in inches.

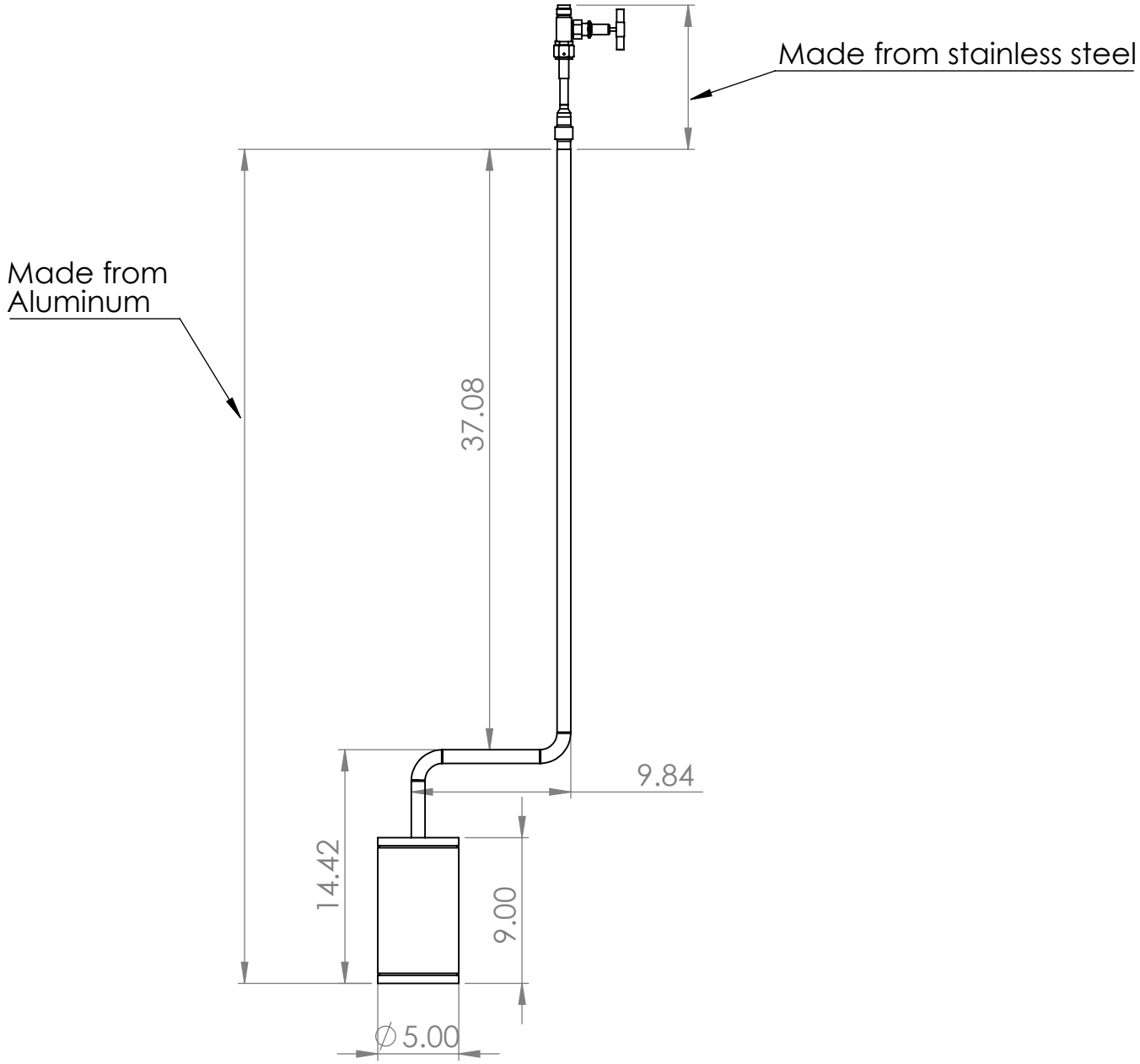

		DIMENSIONS ARE IN INCHES TOLERANCES: FRACTIONAL ± ANGULAR: MACH ± BEND ± TWO PLACE DECIMAL ± THREE PLACE DECIMAL ±		NAME	DATE
			DRAWN		
			CHECKED		
			ENG APPR.		
			MFG APPR.		
		MATERIAL	Q.A.		
			COMMENTS:		
NEXT ASSY	USED ON	FINISH			
APPLICATION		DO NOT SCALE DRAWING			

PROPRIETARY AND CONFIDENTIAL

Xenon Canister Assembly

SIZE	DWG. NO.	REV.
A		
SCALE:1:20	WEIGHT:	SHEET 1 OF 1

Bibliography

[1] Bruce T. Cleveland et al. Measurement of the Solar Electron Neutrino Flux with the Homestake Chlorine Detector. *The Astrophysical Journal*, 496(1), 1998. doi:10.1086/305343.

[2] Y. Fukuda et al. Evidence for Oscillation of Atmospheric Neutrinos. *Physical Review Letters*, 81:1562–1567, Aug 1998. doi:10.1103/PhysRevLett.81.1562.

[3] Q. R. Ahmad et al. Measurement of the Rate of $\nu_e + d \rightarrow p + p + e^-$ Interactions Produced by ^{8}B Solar Neutrinos at the Sudbury Neutrino Observatory. *Physical Review Letters*, 87:071301, Jul 2001. doi:10.1103/PhysRevLett.87.071301.

[4] Ettore Majorana and Luciano Maiani. A symmetric theory of electrons and positrons. In Giuseppe Franco Bassani, editor, *Ettore Majorana Scientific Papers: On occasion of the centenary of his birth*, pages 201–233. Springer Berlin Heidelberg, 2006. doi:10.1007/978-3-540-48095-2_10.

[5] Wolfgang Pauli. [259] Pauli an Meitner U.A. In K. Meyenn, editor, *Wissenschaftlicher Briefwechsel mit Bohr, Einstein, Heisenberg u.a. Band II: 1930–1939 (German) [Scientific Correspondence with Bohr, Einstein, Heisenberg a.o. Volume II: 1930–1939]*, volume 6, pages 39–40. Springer Berlin, Heidelberg, 1985. Original document in German. doi:10.1007/978-3-540-78801-0.

[6] C. D. Ellis and W. A. Wooster. The Average Energy of Disintegration of Radium E. *Proceedings of the Royal Society of London. Series A, Containing Papers of a Mathematical*

and Physical Character, 117(776):109–123, 1927. URL: http://www.jstor.org/stable/94774.

[7] C.S. Wu. History of Beta Decay. In O. R. Frisch, F. A. Paneth, F. Laves, and P. Rosbaud, editors, *Beiträge zur Physik und Chemie des 20. Jahrhunderts: Lise Meitner Otto Hahn Max von Laue zum 80. Geburtstag (German) [Contributions to Physics and Chemistry in the 20th Century: Lise Meitner, Otto Hahn, Max von Laue, on the occasion of the 80th birthday]*, pages 45–65. Vieweg+Teubner Verlag, Wiesbaden, 1959. doi:10.1007/978-3-663-20204-2_5.

[8] Carsten Jensen. *Controversy and Consensus: Nuclear Beta Decay 1911–1934*. Birkhäuser Basel, 2000. doi:10.1007/978-3-0348-8444-0.

[9] C L Cowan et al. Detection of the Free Neutrino: A Confirmation. *Science*, 124:103–104, 7 1956. doi:10.1126/science.124.3212.103.

[10] The Nobel Prize organisation. The Nobel Prize in Physics 1995, 1995. Accessed: 08-14-23. URL: https://www.nobelprize.org/prizes/physics/1995/summary/.

[11] Frederick Reines and Clyde L. Cowan. The Neutrino. *Nature*, 178(4531):446–449, 1956. doi:10.1038/178446a0.

[12] G. Danby, J-M. Gaillard, K. Goulianos, L. M. Lederman, N. Mistry, M. Schwartz, and J. Steinberger. Observation of High-Energy Neutrino Reactions and the Existence of Two Kinds of Neutrinos. *Physical Review Letters*, 9:36–44, 1962. doi:10.1103/PhysRevLett.9.36.

[13] K. Kodama et al. Observation of tau neutrino interactions. *Physics Letters B*, 504(3):218–224, 2001. doi:10.1016/S0370-2693(01)00307-0.

[14] The ALEPH Collaboration, The DELPHI Collaboration, The L3 Collaboration, The OPAL Collaboration, The SLD Collaboration, The LEP Electroweak Working

Group, and The SLD Electroweak and Heavy Flavour Groups. Precision electroweak measurements on the Z resonance. *Physics Reports*, 427(5):257–454, 2006. doi:10.1016/j.physrep.2005.12.006.

[15] Raymond Davis, Don S Harmer, and Kenneth C Hoffman. Search for Neutrinos from the Sun. *Physical Review Letters*, 20:1205–1209, 5 1968. doi:10.1103/PhysRevLett.20.1205.

[16] M. R. Bhat. Evaluated Nuclear Structure Data File (ENSDF). In Syed M. Qaim, editor, *Nuclear Data for Science and Technology*, pages 817–821. Springer Berlin Heidelberg, 1992. Data extracted using the NNDC On-Line Data Service from the ENSDF database, file revised as of 07-01-24. URL: https://www.nndc.bnl.gov/ensdf/.

[17] S.M. Bilenky. Bruno Pontecorvo and the neutrino. *Physics-Uspekhi*, 57(5), 2014. doi:10.3367/UFNe.0184.201405g.0531.

[18] V. Gribov and B. Pontecorvo. Neutrino astronomy and lepton charge. *Physics Letters B*, 28(7):493–496, 1969. doi:10.1016/0370-2693(69)90525-5.

[19] Ziro Maki, Masami Nakagawa, and Shoichi Sakata. Remarks on the Unified Model of Elementary Particles. *Progress of Theoretical Physics*, 28:870–880, 1962. doi:10.1143/PTP.28.870.

[20] Jose Bernabeu. On the history of the PMNS Matrix ...with today's perspective. *Il Nuovo Cimento C*, 37(3):145–154, Jul 2014. doi:10.1393/ncc/i2014-11774-6.

[21] Alessandro De Angelis. *Cosmic Rays: Multimessenger Astrophysics and Revolutionary Astronomy*. Springer Cham, 2023. doi:10.1007/978-3-031-38560-5.

[22] Takaaki Kajita. Atmospheric neutrinos and discovery of neutrino oscillations. *Proceedings of the Japan Academy, Series B Physical and Biological Sciences*, 86(4):303–321, 2010. doi:10.2183/pjab.86.303.

[23] R. L. Workman and Others. Review of Particle Physics. *PTEP*, 2022:083C01, 2022. doi:10.1093/ptep/ptac097.

[24] C. K. Jung, T. Kajita, T. Mann, and C. McGrew. Oscillations of Atmospheric Neutrinos. *Annual Review of Nuclear and Particle Science*, 51:451–488, 2001. doi:10.1146/annurev.nucl.51.101701.132421.

[25] K.S. Hirata et al. Experimental study of the atmospheric neutrino flux. *Physics Letters B*, 205(2):416–420, 1998. doi:10.1016/0370-2693(88)91690-5.

[26] The Nobel Prize organisation. The Nobel Prize in Physics 2015, 2015. Accessed: 08-14-23. URL: https://www.nobelprize.org/uploads/2018/06/press-30.pdf.

[27] X. Qian and P. Vogel. Neutrino mass hierarchy. *Progress in Particle and Nuclear Physics*, 83:1–30, 2015. doi:10.1016/j.ppnp.2015.05.002.

[28] D.V. Forero, M Tórtola, and J.W.F. Valle. Neutrino oscillations refitted. *Physical Review D*, 90:93006, 11 2014. doi:10.1103/PhysRevD.90.093006.

[29] Planck Collaboration et al. Planck 2018 results: VI. Cosmological parameters. *Astronomy & Astrophysics*, 641:A6, 2020. doi:10.1051/0004-6361/201833910.

[30] S Adrián-Martínez et al. Letter of intent for KM3NeT 2.0. *Journal of Physics G: Nuclear and Particle Physics*, 43:084001, 8 2016. doi:10.1088/0954-3899/43/8/084001.

[31] P. F. de Salas et al. 2020 global reassessment of the neutrino oscillation picture. *Journal of High Energy Physics*, 2021(2), 2021. doi:10.1007/jhep02(2021)071.

[32] S. Al Kharusi et al. nEXO Pre-Conceptual Design Report. *arXiv: Instrumentation and Detectors*, 2018. URL: https://arxiv.org/abs/1805.11142.

[33] M. Goeppert-Mayer. Double Beta-Disintegration. *Physical Review*, 48:512–516, Sep 1935. doi:10.1103/PhysRev.48.512.

[34] Petr Vogel. Nuclear structure and double beta decay. *Journal of Physics G: Nuclear and Particle Physics*, 39(12):124002, 2012. doi:10.1088/0954-3899/39/12/124002.

[35] Frank T Avignone, Steven R Elliott, and Jonathan Engel. Double beta decay, Majorana neutrinos, and neutrino mass. *Reviews of Modern Physics*, 80:481–516, 4 2008. doi:10.1103/RevModPhys.80.481.

[36] W. H. Furry. On Transition Probabilities in Double Beta-Disintegration. *Physical Review*, 56:1184–1193, Dec 1939. doi:10.1103/PhysRev.56.1184.

[37] Felix Boehm and Petr Vogel. Double Beta Decay. In *Physics of Massive Neutrinos*, page 159–216. Cambridge University Press, 1992. doi:10.1017/CBO9780511622571.

[38] S. Cebrián et al. Pattern recognition of ^{136}Xe double beta decay events and background discrimination in a high pressure Xenon TPC. *Journal of Physics G Nuclear and Particle Physics*, 40, 06 2013. doi:10.1088/0954-3899/40/12/125203.

[39] Stefano Dell'Oro, Simone Marcocci, Matteo Viel, and Francesco Vissani. Neutrinoless Double Beta Decay: 2015 Review. *Advances in High Energy Physics*, 2016, 2016. doi:10.1155/2016/2162659.

[40] Kai Zuber. *Neutrino Physics*. CRC Press, Florida, 3 edition, 2020. doi:10.1201/9781315195612.

[41] Matthew Redshaw, Elizabeth Wingfield, Joseph McDaniel, and Edmund G. Myers. Mass and Double-Beta-Decay Q Value of ^{136}Xe. *Physical Review Letters*, 98, 2007. doi:10.1103/PhysRevLett.98.053003.

[42] Ruben Saakyan. Two-Neutrino Double-Beta Decay. *Annual Review of Nuclear and Particle Science*, 63(1):503–529, 2013. doi:10.1146/annurev-nucl-102711-094904.

[43] Alexander Barabash. Precise Half-Life Values for Two-Neutrino Double-β Decay: 2020 Review. *Universe*, 6(10), 2020. doi:10.3390/universe6100159.

[44] J. B. Albert et al. Improved measurement of the $2\nu\beta\beta$ half-life of ^{136}Xe with the EXO-200 detector. *Physical Review C*, 89, 2014. doi:10.1103/PhysRevC.89.015502.

[45] R. Arnold et al. Measurement of the $2\nu\beta\beta$ decay half-life of ^{150}Nd and a search for $0\nu\beta\beta$ decay processes with the full exposure from the NEMO-3 detector. *Physical Review D*, 94:072003, Oct 2016. doi:10.1103/PhysRevD.94.072003.

[46] E. Conti et al. Correlated fluctuations between luminescence and ionization in liquid xenon. *Physical Review B*, 68, 2003. doi:10.1103/PhysRevB.68.054201.

[47] E. Aprile and T. Doke. Liquid xenon detectors for particle physics and astrophysics. *Reviews of Modern Physics*, 82:2053–2097, 2010. doi:10.1103/RevModPhys.82.2053.

[48] K. Asakura et al. Search for double-beta decay of ^{136}Xe to excited states of ^{136}Ba with the KamLAND-Zen experiment. *Nuclear Physics A*, 946:171–181, 2016. doi:10.1016/j.nuclphysa.2015.11.011.

[49] J. B. Albert et al. Search for Neutrinoless Double-Beta Decay with the Upgraded EXO-200 Detector. *Physical Review Letters*, 120, 2018. doi:10.1103/PhysRevLett.120.072701.

[50] N. Ackerman et al. Observation of Two-Neutrino Double-Beta Decay in ^{136}Xe with the EXO-200 Detector. *Physical Review Letters*, 107, 2011. doi:10.1103/PhysRevLett.107.212501.

[51] G. Anton et al. Search for Neutrinoless Double-β Decay with the Complete EXO-200 Dataset. *Physical Review Letters*, 123, 2019. doi:10.1103/PhysRevLett.123.161802.

[52] Vincenzo Flaminio, Oliviero Cremonesi, and Maura Pavan. Challenges in Double Beta Decay. *Advances in High Energy Physics*, 2014. doi:10.1155/2014/951432.

[53] Michelle J Dolinski, Alan W P Poon, and Werner Rodejohann. Neutrinoless Double-Beta Decay: Status and Prospects. *Annual Review of Nuclear and Particle Science*, 69:219–251, 2019. doi:10.1146/annurev-nucl-101918-023407.

[54] J.J. Gómez-Cadenas et al. Sense and sensitivity of double beta decay experiments. *Journal of Cosmology and Astroparticle Physics*, 2011(06), 2011. doi:10.1088/1475-7516/2011/06/007.

[55] David Nygren and Jay Marx. The Time Projection Chamber. *Physics Today*, 31(10), 1978. doi:10.1063/1.2994775.

[56] Thomas Lohse and Werner Witzeling. The Time Projection Chamber. In *Instrumentation in high energy physics*, volume 9 of *Advanced series on directions in high energy physics*, pages 81–155. World Scientific, Singapore, 1992. doi:10.1142/1356.

[57] C. Rubbia. The Liquid-Argon Time Projection Chamber: A New Concept for Neutrino Detectors, 1977. URL: https://cds.cern.ch/record/117852/files/CERN-EP-INT-77-8.pdf.

[58] Nicole A. Larsen. Two-Phase Xenon Time Projection Chambers for WIMP Searches and Other Applications. Master's thesis, Yale University Department of Physics, 2012. URL: https://poorvucenter.yale.edu/sites/default/files/files/NicoleLarsen_Prospectus_Physics.pdf.

[59] M. Jewell et al. Characterization of an Ionization Readout Tile for nEXO. *Journal of Instrumentation*, 13(01), 2018. doi:10.1088/1748-0221/13/01/P01006.

[60] G Adhikari et al. nEXO: neutrinoless double beta decay search beyond 10^{28} year half-life sensitivity. *Journal of Physics G: Nuclear and Particle Physics*, 49, 2022. doi:10.1088/1361-6471/ac3631.

[61] J. B. Albert et al. Sensitivity and discovery potential of the proposed nEXO experiment to neutrinoless double-β decay. *Physical Review C*, 97, 2018. doi:10.1103/PhysRevC.97.065503.

[62] Z. Li et al. Simulation of charge readout with segmented tiles in nEXO. *Journal of Instrumentation*, 14(9), 2019. doi:10.1088/1748-0221/14/09/P09020.

[63] E. Aprile et al. Observation of anticorrelation between scintillation and ionization for MeV gamma rays in liquid xenon. *Physical Review B*, 76:014115, Jul 2007. doi:10.1103/PhysRevB.76.014115.

[64] B.G. Lenardo et al. Development of a ^{127}Xe calibration source for nEXO. *Journal of Instrumentation*, 17:P07028, 7 2022. doi:10.1088/1748-0221/17/07/P07028.

[65] S. Bruenner et al. Radon daughter removal from PTFE surfaces and its application in liquid xenon detectors. *The European Physical Journal C*, 81, 2021. doi:10.1140/epjc/s10052-021-09047-2.

[66] E. Aprile et al. First Dark Matter Search Results from the XENON1T Experiment. *Physical Review Letters*, 119, 2017. doi:10.1103/PhysRevLett.119.181301.

[67] D.S. Akerib et al. Radiogenic and muon-induced backgrounds in the LUX dark matter detector. *Astroparticle Physics*, 62, 2015. doi:10.1016/j.astropartphys.2014.07.009.

[68] B. Lubsandorzhiev. "New" and "Old" ideas in photon detection. *Proceedings of Science*, 2016. doi:10.22323/1.252.0040.

[69] D. Renker. Geiger-mode avalanche photodiodes, history, properties and problems. *Nuclear Instruments and Methods in Physics Research Section A: Accelerators, Spectrom-*

eters, Detectors and Associated Equipment, 567(1):48–56, 2006. doi:10.1016/j.nima.2006.05.060.

[70] B.K. Lubsandorzhiev. On the history of photomultiplier tube invention. *Nuclear Instruments and Methods in Physics Research Section A: Accelerators, Spectrometers, Detectors and Associated Equipment*, 567(1):236–238, 2006. doi:10.1016/j.nima.2006.05.221.

[71] Matsusada Precision. Photomultiplier Tube (PMT). Accessed: 04-21-24. URL: https://www.matsusada.com/application/ps/photomultiplier_tubes/.

[72] George H. Rieke. Other Photodetectors. In *Detection of Light*, pages 174–214. Cambridge University Press, 3 edition, 2021. doi:10.1017/9781316407189.

[73] Samo Korpar and Peter Križan. Photon Detectors. In *Handbook of Particle Detection and Imaging*, pages 353–370. Springer Cham, 2 edition, 2021. doi:10.1007/978-3-319-93785-4.

[74] Frank Simon. Silicon photomultipliers in particle and nuclear physics. *Nuclear Instruments and Methods in Physics Research Section A: Accelerators, Spectrometers, Detectors and Associated Equipment*, 926:85–100, 2019. doi:10.1016/j.nima.2018.11.042.

[75] Stefan Gundacker and Arjan Heering. The silicon photomultiplier: fundamentals and applications of a modern solid-state photon detector. *Physics in Medicine & Biology*, 65(17), 2020. doi:10.1088/1361-6560/ab7b2d.

[76] George Rieke. Photodiodes and other junction-based detectors. In *Detection of Light: From the Ultraviolet to the Submillimeter*, pages 78–115. Cambridge University Press, 2002. doi:10.1017/CBO9780511606496.

[77] Douglas S. McGregor. Semiconductor Radiation Detectors. In *Handbook of Particle Detection and Imaging*, pages 451–494. Springer Cham, 2 edition, 2021. doi:10.1007/978-3-319-93785-4.

[78] Erika Garutti. Silicon Photomultipliers. In *Handbook of Particle Detection and Imaging*, pages 495–514. Springer Cham, 2 edition, 2021. doi:10.1007/978-3-319-93785-4.

[79] Federico Capasso. Chapter 1 Physics of Avalanche Photodiodes. In W.T. Tsang, editor, *Lightwave Communications Technology*, volume 22, pages 1–172. Elsevier, 1985. doi:10.1016/S0080-8784(08)62952-X.

[80] David Jenkins. Scintillator detectors for gamma-ray detection. In *Radiation Detection for Nuclear Physics*. IOP Publishing, 2020. doi:10.1088/978-0-7503-1428-2.

[81] Fabio Acerbi and Stefan Gundacker. Understanding and simulating SiPMs. *Nuclear Instruments and Methods in Physics Research Section A: Accelerators, Spectrometers, Detectors and Associated Equipment*, 926:16–35, 2019. doi:10.1016/j.nima.2018.11.118.

[82] Claudio Piemonte and Alberto Gola. Overview on the main parameters and technology of modern Silicon Photomultipliers. *Nuclear Instruments and Methods in Physics Research Section A: Accelerators, Spectrometers, Detectors and Associated Equipment*, 926, 2019. doi:10.1016/j.nima.2018.11.119.

[83] Patrick Eckert et al. Characterisation studies of silicon photomultipliers. *Nuclear Instruments and Methods in Physics Research Section A: Accelerators, Spectrometers, Detectors and Associated Equipment*, 620(2), 2010. doi:10.1016/j.nima.2010.03.169.

[84] G. Anton et al. Measurement of the scintillation and ionization response of liquid xenon at MeV energies in the EXO-200 experiment. *Physical Review C*, 101, 2020. doi:10.1103/PhysRevC.101.065501.

[85] Christopher Chambers. Light-only Liquid Xenon (LoLX) Detector for Cherenkov and Scintillation Light Investigation. 2022. URL: https://indico.triumf.ca/event/269/contributions/3424/.

[86] Larisa M. Ganea, Andrei I. Apostol, and Ana Pantelica. Non-destructive analysis of pure-beta emitters: applications in nuclear forensics. *Journal of Radioanalytical and Nuclear Chemistry*, 322(3), 2019. doi:10.1007/s10967-019-06814-0.

[87] Stephanie Bron. New photosensor assembly in the Light only Liquid Xenon (LoLX) experiment: design and measurement prospects. 2023. URL: https://indico.cern.ch/event/1191895/contributions/5333533/.

[88] Laraweb. Decay scheme made using the query Xe-127. URL: http://www.lnhb.fr/Laraweb/index.php.

[89] M.-M. Bé et al. *Table of Radionuclides*, volume 8 of *Monographie BIPM-5*. Bureau International des Poids et Mesures, Pavillon de Breteuil, F-92310 Sèvres, France, 2016. URL: http://www.bipm.org/utils/common/pdf/monographieRI/Monographie_BIPM-5_Tables_Vol8.pdf.

[90] Dobromir S. Pressyanov. Short solution of the radioactive decay chain equations. *American Journal of Physics*, 70, 2002. doi:10.1119/1.1427084.

[91] Harry Bateman. Solution of a system of differential equations, etc. In *Proceedings of the Cambridge Philosophical Society*, volume XV, pages 423–427. Cambridge University Press, 1908-1910. URL: https://www.biodiversitylibrary.org/item/97262#page/490/mode/1up.

[92] N. J. Carron. Selected Topics on Neutron Interactions. In *An Introduction to the Passage of Energetic Particles through Matter*, pages 305–345. Taylor and Francis, 2007. doi:10.1201/9781420012378.

[93] Alexandre Obertelli and Hiroyuki Sagawa. *Modern Nuclear Physics*. Springer Singapore, 2021. doi:10.1007/978-981-16-2289-2.

[94] Shunzhong Luo. *Nuclear Science and Technology: Isotopes and Radiation*. Springer Singapore, 2023. doi:10.1007/978-981-99-3087-6.

[95] *Manual for Reactor Produced Radioisotopes*. Number 1340 in TECDOC Series. International Atomic Energy Agency, Vienna, 2003. URL: https://www.iaea.org/publications/6407/manual-for-reactor-produced-radioisotopes.

[96] Greg Brian Lamarre. Experimental and Computational Determination of Radiation Dose Rates in the SLOWPOKE-2 Research Reactor at the Royal Military College of Canada/Collège Militaire Royal du Canada. Master's thesis, Royal Military College of Canada/Collège Militaire Royal du Canada, 1999. URL: https://www.collectionscanada.gc.ca/obj/s4/f2/dsk3/ftp04/Mq44912.pdf.

[97] Government of Canada: Royal Military College of Canada. SLOWPOKE-2 Facility. Accessed: 05-20-24. URL: https://www.rmc-cmr.ca/en/chemistry-and-chemical-engineering/slowpoke-2-facility.

[98] D.A. Huston, P. Samuleev, F. Kelly, and E.C. Corcoran. Characterization of flux distribution in the pool of the RMC SLOWPOKE-2. *Applied Radiation and Isotopes*, 27, 2024. doi:10.1016/j.apradiso.2024.111262.

[99] John R. de Laeter et al. Atomic weights of the elements. Review 2000 (IUPAC Technical Report). *Pure and Applied Chemistry*, 75(6):683–900, 2003. doi:10.1351/pac200375060683.

[100] F.G. Kondev et al. The NUBASE2020 evaluation of nuclear physics properties. *Chinese Physics C*, 45(3), 2021. URL: https://www-nds.iaea.org/relnsd/nubase/nubase_min.html.

[101] D.A.Brown et al. ENDF/B-VIII.0: The 8th major release of the nuclear reaction data library with CIELO-project cross sections, new standards and thermal scattering data. *Nuclear Data Sheets*, 148, 2018. URL: https://www-nds.iaea.org/exfor/endf.htm.

[102] A.J. Koning, D. Rochman, J.-Ch. Sublet, N. Dzysiuk, M. Fleming, and S. van der Marck. TENDL: Complete Nuclear Data Library for Innovative Nuclear Science and Technology. *Nuclear Data Sheets*, 155, 2019. URL: https://tendl.web.psi.ch/tendl_2023/tendl2023.html, doi:10.1016/j.nds.2019.01.002.

[103] Multipurpose 6061 Aluminum 5" diamter. URL: https://www.mcmaster.com/1610T48/.

[104] Alloy Wire International. Stainless Steel 321. URL: https://www.alloywire.com/wp-content/uploads/2021/06/AW_Datasheet_STAINLESS-STEEL-321_Rev-2.pdf.

[105] McGill Environmental Health & Safety. McGill Radiation Safety Manual Edition 7.0, 2016. URL: https://www.mcgill.ca/ehs/files/ehs/radiation_safety_manual-_ed_7.0.pdf.